

Characterisation of laminated construction materials based on ultrasonic reflection measurements

Proefschrift

ter verkrijging van de graad van doctor
aan de Technische Universiteit Delft,
op gezag van de Rector Magnificus prof. ir. K. F. Wakker,
in het openbaar te verdedigen ten overstaan van een commissie,
door het College voor Promoties aangewezen,
op dinsdag 28 maart 2000 te 16:00 uur

door

Johan VOS



burgerlijk mijnbouwkundig ingenieur
aan de Katholieke Universiteit Leuven, België
geboren te Mechelen, België

Dit proefschrift is goedgekeurd door de promotoren:

Prof. dr.ir. A.J. Berkhout

Prof. dr.ir. C.P.A. Wapenaar

Toegevoegd promotor:

Dr. ir. D.J. Verschuur

Samenstelling Promotiecommissie:

Rector Magnificus,	voorzitter
Prof. dr. ir. A. J. Berkhout,	Technische Universiteit Delft, promotor
Prof. dr. ir. C. P. A. Wapenaar,	Technische Universiteit Delft, promotor
Dr. ir. D.J. Verschuur,	Technische Universiteit Delft, toegevoegd promotor
Prof. ir. L.B. Vogelesang,	Technische Universiteit Delft
Prof. dr. ir. J.T. Fokkema,	Technische Universiteit Delft
Prof. dr. K.J. Langenberg,	Universität Kassel
Dr. ir. R.A.M. Coenen,	ING-Groep

ISBN 90-9013594-4

Copyright ©2000, by J. Vos, Delft University of Technology, Delft, The Netherlands.

All rights reserved. No part of this publication may be reproduced, stored in a retrieval system or transmitted in any form or by any means, electronic, mechanical, photocopying, recording or otherwise, without the prior written permission of the author J. Vos, Delft University of Technology, Faculty of Applied Sciences, P.O. Box 5046, 2600 GA Delft, The Netherlands.

SUPPORT

The research for this thesis was financially supported by the Dutch foundation for Technology (STW);(DLR.3433)

Typesetting system: L^AT_EX

Printed in The Netherlands by: DocVision BV. Technische Universiteit Delft.

*Nothing vanishes
without a trace.*



Contents

Notation and terminology	xi
1 Ultrasonic inspection of laminated materials	1
1.1 Advanced ultrasonic inspection	1
1.1.1 Importance of inspection	1
1.1.2 Non-destructive inspection	2
1.1.3 Ultrasonic inspection	3
1.1.4 Advanced processing	5
1.2 Outline of this thesis	6
2 The forward model	11
2.1 Acoustic wave theory	11
2.1.1 Continuum hypothesis	12
2.1.2 The equation of motion	17
2.1.3 The deformation equation	19
2.1.4 The constitutive coefficients in a time-invariant medium . . .	21
2.1.5 Low-velocity approximation	24
2.2 Instantaneously reacting medium	24
2.2.1 General wave equation	25
2.2.2 Plane wave theory	26
2.3 Medium with relaxation	28

2.3.1	General wave equation	29
2.3.2	Plane wave theory	32
2.4	Boundary conditions	35
2.5	Forward model in a layered configuration	36
2.5.1	Initiation step	39
2.5.2	Recursion steps	40
2.6	Simulations	44
2.6.1	Aluminium layer	45
2.6.2	Prepreg	46
2.6.3	Glare	52
3	Measurements	59
3.1	Conversion of the acoustic pressures	59
3.1.1	Conversion to acoustic energy	61
3.1.2	Conversion from acoustic energy	61
3.2	Transducers	61
3.2.1	Wavefield emitted by a flat cylindrical radiator	62
3.2.2	Wavefield emitted by a cylindrical focusing radiator	65
3.3	Preprocessing	68
3.4	Source signal	73
3.4.1	15 MHz, unfocused transducer	75
3.4.2	15 MHz, focussed transducer	77
3.4.3	20 MHz, focussed transducer	78
3.5	Reflection measurements	80
3.5.1	Aluminium disk	80
3.5.2	Prepreg	83
3.5.3	Glare	87
4	Recursive Direct Inversion	93
4.1	Inversion parameters and acoustic parameters	93
4.2	Inverse theory	94
4.3	Obtaining the wavefield parameters	96

4.3.1	Separated arrivals	97
4.3.2	Interfering arrivals	103
4.4	Inversion algorithm	108
4.5	Inversion on simulated data	109
4.5.1	Aluminium layer	111
4.5.2	Glare	113
4.6	Inversion on measured data	124
4.6.1	Aluminium layer	124
4.6.2	Glare 2/1	126
5	Iterative Parametric Optimisation	129
5.1	Theory of parametric optimisation	129
5.1.1	Description of the optimisation problem	130
5.1.2	Steepest descent method	132
5.1.3	Gauss-Newton Method	135
5.1.4	Stop criterion	137
5.1.5	The choice of parameters	137
5.2	Optimisation on simulated data	138
5.2.1	Aluminium layer	138
5.2.2	Glare	147
5.3	Optimisation on measured data	152
5.3.1	Aluminium layer	152
5.3.2	Glare 2/1	153
6	Conclusions and recommendations	159
6.1	Conclusions	159
6.2	Recommendations	161
6.2.1	Using the existing model	161
6.2.2	Enhanced model	162
A	Glare	165
A.1	Structure and naming	165
A.2	Properties	166

Bibliography	171
Summary	173
Samenvatting	175
Curriculum vitae	177
Dankwoord	179

Notation and terminology

Transformations

In this thesis, extensive use is made of the temporal Fourier Transform. The forward temporal Fourier Transform $F(\omega)$ of a function of time $f(t)$ is defined as

$$F(\omega) = \int_{-\infty}^{+\infty} f(t) \exp(-j\omega t) dt. \quad (1)$$

The inverse temporal Fourier Transform retrieves the time-function based on the frequency spectrum $F(\omega)$:

$$f(t) = \frac{1}{2\pi} \int_{-\infty}^{+\infty} F(\omega) \exp(j\omega t) d\omega. \quad (2)$$

If $f(t)$ is a real function, it holds that

$$f(t) = \frac{1}{\pi} \text{Re} \left[\int_0^{+\infty} F(\omega) \exp(j\omega t) d\omega \right]. \quad (3)$$

As a consequence, no negative values of ω have to be taken into account when the considered function is real valued in time.

Terminology

- A function f is called time-invariant if the evaluation of f does not depend on the time it is evaluated, i.e.

$$f(t_0) = f(t_1). \quad (4)$$

- Einstein summation convention: a repeated subscript in an expression implies summation:

$$\lambda_j \nu_j = \lambda_1 \nu_1 + \lambda_2 \nu_2 + \lambda_3 \nu_3. \quad (5)$$

- The partial derivate of a function with respect to time — ∂_t — is used when the considered function is also dependent on another parameter except the time.

The absolute time-derivative — d_t — is used when the function it is applied to only depends on the time.

- The delta-function $\delta(t)$ is defined as follows:

$$\delta(t) = 0 \text{ if } t \neq 0, \quad (6)$$

$$\int_{t=-\epsilon}^{\epsilon} \delta(t) dt = 1, \text{ for any } \epsilon > 0. \quad (7)$$

- According to Kreyszig (1972), "a function $f(t)$ is piecewise continuous on a finite interval $a \leq t \leq b$, if it is defined on that interval and is such that the interval can be subdivided into finitely many intervals, in each of which $f(t)$ is continuous and has finite limits as t approaches either end point of the interval of subdivision from the interior".
- A function $f(t)$ is a causal function when

$$f(t) = 0, \text{ for } t < 0. \quad (8)$$

- If a quantity is written as $A(\omega) \exp(j\beta(\omega))$ with $A(\omega)$ and $\beta(\omega)$ real valued, then $A(\omega)$ is called the amplitude and $\beta(\omega)$ is called the phase.
- The term *interface* is used for denoting the boundary separating two regions with different medium parameters.

Table of notation

t	=	time [s]
\mathbf{x}^α	=	position of particle α
\mathbf{w}^α	=	instantaneous velocity of particle α [m s ⁻¹]
m^α	=	mass of particle α [kg]
\mathcal{D}_ϵ	=	elementary time-invariant domain
\mathcal{N}_ϵ	=	number of particles in an elementary time-invariant domain
\mathcal{V}_ϵ	=	volume of an elementary time-invariant domain
n	=	number density [m ⁻³]
ρ	=	volume density of mass [kg m ⁻³]
\mathbf{v}	=	drift velocity [m s ⁻¹]
ϕ	=	mass flow density [kg m ⁻² s ⁻¹]
$\dot{\phi}$	=	mass flow density rate [kg m ⁻² s ⁻²]
\mathcal{D}	=	time-variant domain
\mathbf{f}^V	=	volume force density [N m ⁻³]
\mathbf{F}^V	=	volume force [N]
\mathbf{t}	=	traction [N m ⁻³]
\mathbf{F}^S	=	surface force [N]
\mathcal{M}	=	linear momentum [kg m s ⁻¹]
p	=	acoustic pressure [N m ⁻²] or [Pa]
ν	=	unit normal vector
f	=	frequency [s ⁻¹] or [Hz]
ω	=	angular frequency [rad s ⁻¹], $\omega = 2\pi f$
j	=	imaginary unit, $j = \sqrt{-1}$
q	=	volume source density of volume injection rate [s ⁻¹]
$\dot{\theta}$	=	induced part of the cubic dilatation rate [s ⁻¹]
κ	=	compressibility [Pa ⁻¹]
μ	=	inertia relaxation function [kg m ⁻³ s ⁻¹]
χ	=	compliance relaxation function [Pa ⁻¹ s ⁻¹]
c	=	acoustic velocity [m s ⁻¹]
Z	=	specific acoustic impedance [kg m ⁻² s ⁻¹]
K	=	coefficient of frictional force [kg m ⁻³ s ⁻¹]
Γ	=	coefficient of bulk inviscidness [Pa ⁻¹ s ⁻¹]
$\hat{\rho}$	=	generalised volume density of mass [kg m ⁻³]
$\hat{\kappa}$	=	generalised compressibility [Pa ⁻¹]
\hat{c}	=	generalised acoustic velocity [m s ⁻¹]

\dot{Q}^d	=	volume density of dissipated power [Pa s ⁻¹]
\dot{W}^{ext}	=	total acoustic power delivered by sources [N m s ⁻¹]
P^a	=	net acoustic power flow [N m s ⁻¹]
W^{kin}	=	kinetic energy of the acoustic wavefield [N m]
W^{def}	=	deformation energy of the acoustic wavefield [N m]
P^d	=	dissipated acoustic power [N m s ⁻¹]
γ_r	=	attenuation coefficient [m ⁻¹]
W	=	propagation factor
R_i	=	reflection coefficient at interface $i + 1$ between layers i and $i + 1$
T_i	=	transmission coefficient at interface $i + 1$ between layers i and $i + 1$
S	=	source spectrum
X_i	=	transfer function at depth z_i
X_i^0	=	interface-free transfer function at depth z_i

Chapter 1

Ultrasonic inspection of laminated materials

In this first chapter, the topic of this thesis is situated in a more general context. The benefits of the research project are briefly mentioned. Next, an outline of this thesis is given.

1.1 Advanced ultrasonic inspection

In this section, the importance of ultrasonic reflection measurements is discussed. This technique is placed in the field of inspection techniques, and it is explained when it is appropriate to use such an inspection technique. Further, the benefits of advanced signal processing are given.

Special attention is paid to the inspection of aircrafts, and more specific to the laminated materials these aircrafts can be composed of.

1.1.1 Importance of inspection

In many disciplines, the inspection of materials, accessories and final products is of great importance. Inspection techniques can provide information about the quality of products. Depending on the nature and the intended use of the product, the quality can influence the economical aspects of the material and it can have consequences for the functionality and safety of the product.

Although inspection techniques may be rather costly, their use can decrease the total costs of products. When a final product is composed of different components, it is advantageous that possible defects in the components are discovered as soon as possible.

The profit of a product partly depends on the quality of the constituting parts. An inspection of these accessories gives an indication about some of the properties.

Among others, these properties include

- mechanical properties: a material might be strong or weak, hard or soft etc;
- density: the density of a material is of particular interest in the aircraft industry, where heavier materials hinder the elevation;
- the behaviour of the material under extreme conditions: materials that are used in aircrafts may be exposed both to extremely high and extremely low temperatures;
- the cohesion between the different components which is of major importance in laminated materials, where for example unwanted void inclusions between two layers can affect the reliability of the material.

When a final product has to meet specific criteria — e.g. an aircraft has to be able to carry a certain load —, the constituting parts also have to meet specific requirements. If one of the materials used in an aircraft does not meet the necessary requirements, this can have serious consequences concerning the safety. Therefore, it is important that the properties of the crucial parts of the aircraft are monitored on a regular basis and that defects are detected as soon as possible.

1.1.2 Non-destructive inspection

Inspection techniques are generally classified into two groups. If the target material is affected by the test, the technique is called a destructive inspection technique. On the other hand, if after performing the test none of the properties are changed, use is made of a non-destructive technique.

In general, destructive inspection techniques are easier to perform and are often cheaper than non-destructive techniques. Destructive inspection is often used in combination with statistical methods. A test is performed on a subset of a number of target materials, and the results are extrapolated to the entire set. For an overview of destructive techniques, the reader is referred to De Meester (1988).

In many cases, however, it is important that the target material remains intact after testing, which requires the use of a non-destructive inspection technique. All critical parts in aircrafts, for example, have to be inspected and they have to be used after that inspection.

The goal of non-destructive inspection (NDI) techniques is to quantify a material parameter without affecting this parameter. In many NDI-techniques, use is made of indirect measurements. A physical relationship between the measured quantity and the desired parameter is then used for quantifying the desired parameter.

This thesis is focused on ultrasonic non-destructive inspection techniques.

1.1.3 Ultrasonic inspection

Due to the increasing interest in non-destructive inspection, the number of NDI-techniques also increases. An overview of these techniques and their application fields can be found in Bray and Stanley (1997). There is no ideal technique which covers all types of defects in all types of material. Which technique one has to use depends on a number of factors, including

- the parameters that have to be investigated;
- the accuracy with which the parameters have to be obtained;
- the available time and money;
- the size, nature and specific requirements of the target;
- the nature of possible flaws.

This thesis is concerned with a particular non-destructive ultrasonic inspection techniques, based on reflection measurements. In an ultrasonic inspection experiment, an ultrasonic wave is generated — e.g. by means of a piezo-electric transducer which converts an electrical pulse into an acoustic sound wave. The wave travels through a coupling medium, and interacts with the target material. Due to this interaction, a scattered ultrasonic wavefield arises. The characteristics of this resulting wavefield depend on the characteristics of the original wavefield and on the acoustic parameters of the target. Therefore, this method is suited for quantifying the acoustic parameters of the target material — and, indirectly, the parameters that can be related to the acoustic parameters.

Current C-Scan inspection

Laminated materials — as used in the aerospace industry — are often inspected with a C-scan system. Traditional C-scan measurements are studied by a.o. Coenen (1998). Typically, two transducers are used. The first transducer generates an ultrasonic wave, while the second transducer, placed at the other side of the target, records the transmitted wavefield. After the wavefield has been recorded, the transducers are moved to a next position. If the transducer pair is moved in two dimensions, the series of measurements on different positions is called a C-scan¹. A traditional C-scan setup is shown in Figure 1.1. For each measurement, the attenuation level is calculated. The attenuation level is defined as the logarithm of the ratio of the maximum absolute value of the input signal — generated by the first

¹The term A-scan is used for a single measurement, and a B-scan is obtained when the transducers are moved in one dimension.

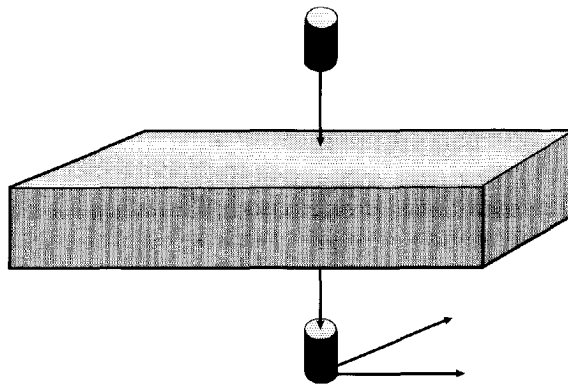


Fig. 1.1 Traditional C-scan setup. The transducers move simultaneously in two dimensions parallel to the target. For each position of the transducers, a measurement can be done.

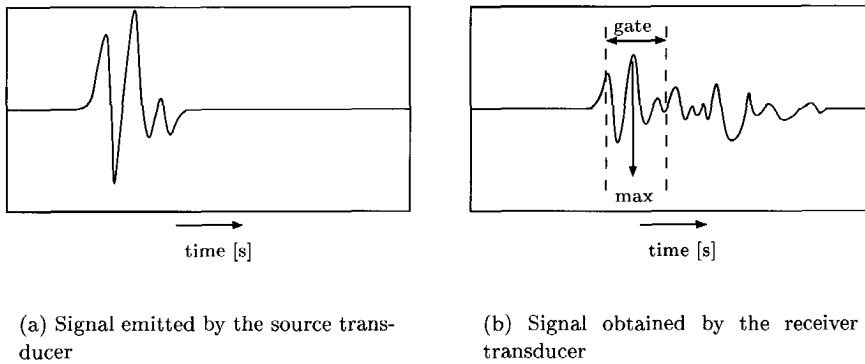


Fig. 1.2 Signal at source transducer and receiver transducer. A time-window — or gate — is placed at the receiver transducer, and the maximum absolute value of the signal in that time-window is preserved.

transducer — and the maximum absolute value of the signal received by the second transducer. Optionally, the second value is replaced by the maximum absolute value of the received signal over a fixed time-window. This principle is illustrated in Figure 1.2.

Generally, the obtained attenuation levels for the different positions at the target are rendered in a 2D-plot. A typical C-scan measurement then looks like Figure 1.3(a).

Dark regions indicate a high attenuation level, whereas light regions indicate less attenuation. A high attenuation may be due to a high porosity or a void-inclusion,

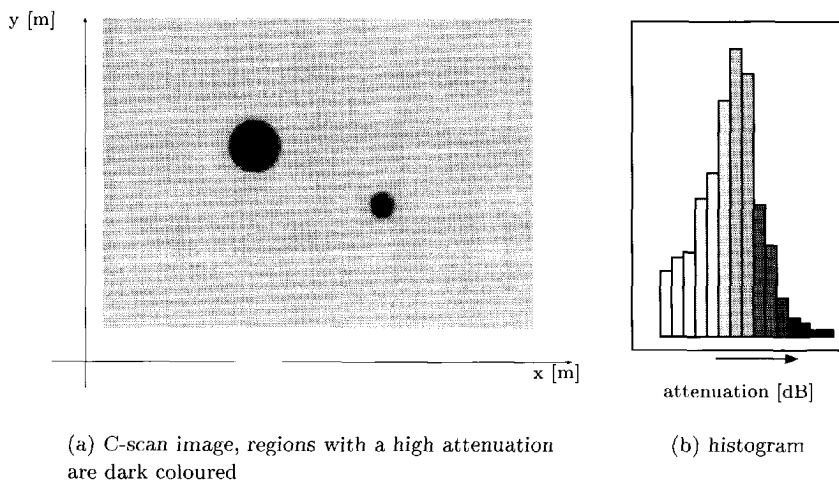


Fig. 1.3 Example of a C-scan image and histogram.

which are both undesired in construction materials. Therefore, regions with a high attenuation level are considered dangerous. When there are too many points with a high attenuation level the material is rejected.

Further analysis of the C-scan image can be done by means of the histogram — as shown in Figure 1.3(b). The attenuation range is subdivided into a finite number of intervals. The number of sample points that occur in each attenuation interval is calculated and the result is shown in the histogram.

1.1.4 Advanced processing

Although a complete time trace is obtained for each measurement position, in C-scans only one number is preserved for each measurement — the maximum absolute value that occurs in a pre-defined time-window. The other data are not processed, although they contain useful information. In this thesis, an advanced processing method is described. Applying this method on the complete time trace can reveal more detailed information about the region where the measurement was done. In the case of laminated materials, it is possible to indicate in which layer possible attenuation effects occur.

Current C-scan systems are based on transmission measurements. In a number of cases, however, it is not possible to access the target material from two opposite

sides. Ultrasonic inspection can still be performed, but the transducer that emits the source signal also has to record the scattered wavefield — or a second transducer has to be placed at the same side of the material. It is clear that the scattered wavefield at one side of the target will be different from the scattered wavefield at the other side of the target. Principles and techniques used to detect the attenuation in the material from transmission measurements no longer hold for reflection measurements. Therefore, the model described in this thesis will be based on reflection measurements — although the principles the method is based on can also be used in transmission measurements.

As a consequence, the new model both enhances the quality of ultrasonic measurements, and it solves a practical problem.

In order to obtain processing techniques that are based on wavefield propagation and reflection, it is necessary to understand these principles. A close examination of the interaction of an ultrasonic wave with a target material can provide information that then can be used for the development of processing techniques for inspecting target materials where only single-side access is possible, or where more information about the constituting layers is desired.

It will be shown in this thesis that the interaction of an ultrasonic wave with a target can rather easily be described when this target consists of a finite number of homogeneous, parallel layers — so-called laminated materials. Based on this description, the inverse problem can be solved: starting from the measured scattered wavefield, it is possible to obtain the material parameters of the target.

Although the algorithms developed in this thesis can be applied to laminated materials in general, they are illustrated on Glare configurations. Glare is a fibre metal laminate developed at the Faculty of Aerospace Engineering of the Delft University of Technology — see Appendix A.

1.2 Outline of this thesis

In this thesis, the phenomenon of wavefield propagation in layered media is examined. Knowledge of this phenomenon is required for the development of algorithms and software applications that provide useful information based on the result of an ultrasonic measurement.

The flow chart in Figure 1.4 clarifies the relationships between the different aspects of the research.

In Chapter 2, a forward model is discussed that describes the interactions that will take place when an acoustic wave is sent through a layered material. The model is based on some fundamental aspects of physics, and it holds for a variety of cases. This general model is too complex for performing numerical simulations. Therefore,

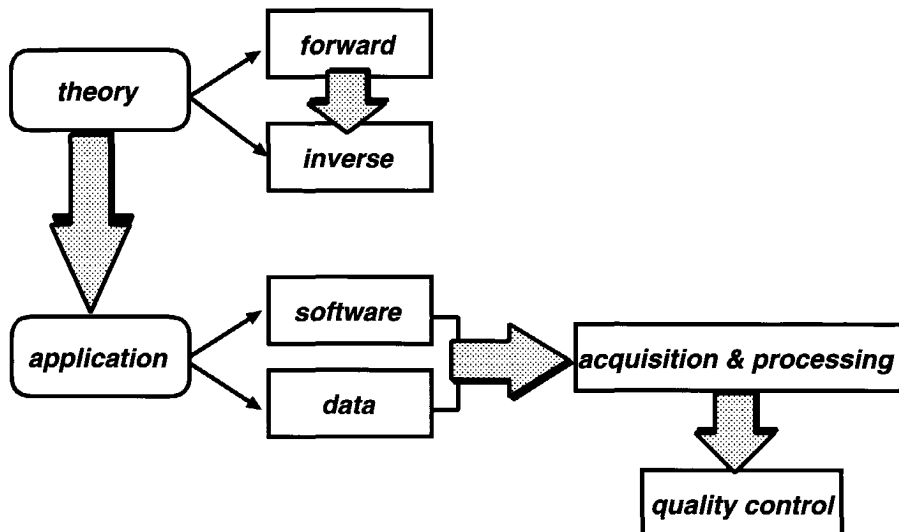
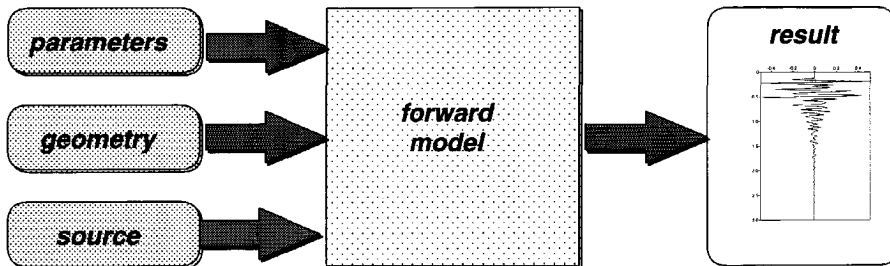


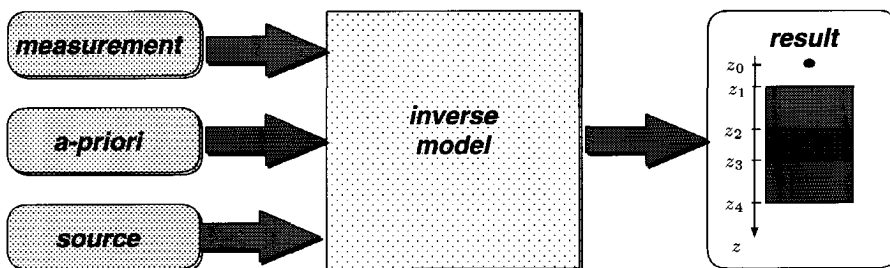
Fig. 1.4 Different aspects in the development of an application for the advanced processing of data obtained by ultrasonic reflection measurements. Both the quality of the algorithms and of the measured data contribute to the quality of the inspection results.

some assumptions are made step by step, in order to arrive at a model that is valid in layered media, where the constituting materials are considered to be homogeneous. Based on the developed model, some simulations are performed. These simulations are based on configurations that are often used in practice — the parameters for the constituting layers are chosen as realistic as possible. The principles of a simulation are given in Figure 1.5(a). Based on the acoustic parameters of the different layers, the geometrical configuration and the used source signal, the resulting scattered wavefield is predicted by the forward model.

In the third chapter, experimental measurements are discussed. The inversion algorithms that will be developed in the subsequent chapters will pose some requirements on the quality of the data. In this chapter, the quality of the data for different configurations is examined. First, the devices that convert the acoustic wavefield into



(a) The forward theory links the acoustic parameters with the resulting wavefield



(b) The inverse theory links the measured wavefield with the acoustic parameters of the material. A-priori information can enhance the quality of the result.

Fig. 1.5 Forward and inverse model.

a computer-friendly representation are discussed. The principles of transducers are explained. Different transducers are tested and compared against each other, and the pro's and con's are given.

Further, some tools are introduced for pre-processing the data. It is shown that the quality of the data can significantly be enhanced by combining different measurements. The pre-processed data will be used as the input for the inversion algorithms. Pre-processing is the first step in the chain, and a very important one. It will be shown that errors occurring in the beginning of the processing-chain will inflate and

disturb the final result.

The measurements are compared with the results of the simulations performed in the second chapter. Although the similarity between the predicted and the measured signal is not a proof that the used model is valid, it is a strong indication for the usefulness of the model for the considered configuration.

The next two chapters describe two algorithms that retrieve the acoustic parameters for each layer of the inspected material. For this purpose, the measured wavefield and the used source signal have to be known. The principle of inversion is shown in Figure 1.5(b).

The algorithm described in Chapter 4 is the Recursive Direct Inversion algorithm. It is based on a direct inversion of the formulas that form the basis for the forward algorithm, developed in Chapter 2. It is a recursive algorithm since each step of the algorithm only gives information about the current top-most layer. Information about the other layers is then obtained by performing the next recursion step on the result of an elimination-process, which eliminates the influence of the current top-most layer.

In order to deal with some practical problems, a number of mathematical and statistical tools are used — i.e. for enhanced peak detection.

The usefulness of the algorithm is first tested on simulated data, and later on measured data.

A second inversion approach is given in Chapter 5. In this chapter, a method is described for obtaining the acoustic parameters of each layer using an iterative procedure. Starting from an initial set of expected parameters, the iterative algorithm will give a new set of acoustic parameters. The new set will be "better" than the old set, and it is expected that the obtained series converge towards the real set of acoustic parameters.

In the last chapter it is concluded that the model described in this thesis agrees with experiments, and the developed inversion techniques can be used to obtain the material parameters of the different layers.

Finally, some directions are given for new research. The main principles of the model described in this thesis are also used in seismic exploration. The application of other techniques used in seismics — in particular multi-offset experiments — may lead to improvements in the field of ultrasonic inspection.

Chapter 2

The forward model

In this chapter the interactions between an acoustic wave and a laminated material are studied. First, relationships between microscopic phenomena and macroscopic, observable quantities are derived. The theory is then applied to the special case of acoustic wave propagation in laminated materials. Next, an algorithm is developed in order to predict the acoustic response of a laminated material on a known source. Finally, this algorithm is used to perform simulations on configurations that will be used in practice.

2.1 Acoustic wave theory

The result of a measurement is a series of numbers representing one or more macroscopic quantities — e.g. the drift velocity \mathbf{v} or the acoustic pressure p — that are measured as a function of a variable parameter — e.g. the time t , or the position \mathbf{x} . In the development of an algorithm for performing simulations, extensive use is made of these macroscopic quantities. It is therefore necessary that the macroscopic quantities are well-defined and have a physical meaning.

In this section, a model will be built that allows to predict the macroscopic acoustic quantities based on the acoustic source and the knowledge of the acoustic parameters of the material. It should be stressed here that the theory will be developed for an acoustic medium. An acoustic medium is capable of carrying compressional forces. The term *acoustic waves* is often used for denoting waves associated with compressional forces. An *ideal fluid* is a fluid that can only support compressional forces, and that will not react when a shear force is applied — as a consequence, it is an acoustic medium. Solid media can also support shearing forces. In the latter case, both compressional and shear waves may occur, and conversions between these two types may occur at interfaces. These media are called elastic media. A description

of the elastic wave equation can be found in Achenbach (1973), Aki and Richards (1980), Wapenaar and Berkhouw (1989) and applications for layered media are given by Brekhovskikh (1980) and Kennett (1983).

Although target materials like Glare are capable of carrying shear forces, an acoustic approach is still valid in the case the path followed by the incident wave is always perpendicular to the interfaces. In this case, no conversion from compressional forces into shear forces occurs. This condition is satisfied if

- the target material is embedded in an ideal fluid and the path followed by the incident wave through this fluid is perpendicular to the target boundary — as a consequence, no shear waves will enter the target,
- the layers are parallel to each other — as a consequence, incident compressional waves will not convert into shear waves.

2.1.1 Continuum hypothesis

In this subsection, the relationship between macroscopic and microscopic quantities is investigated. What is measured — a series of macroscopic quantities — is a consequence of the presence of microscopic structures and the interactions that exist between these structural elements.

The wave theory developed in this section makes abstraction of the microscopic layer, and tries to enclose all microscopic quantities in space- and time-dependent macroscopic parameters. It turns out that the *continuum hypothesis* is an essential condition that has to be satisfied in order to define macroscopic quantities.

microscopic quantities

An elementary time-invariant domain $\mathcal{D}_\epsilon(\mathbf{x}_c)$, located in the investigated medium and with geometrical centre in \mathbf{x}_c is considered — see Figure 2.1. In this domain, elementary particles are labelled with the superscript α . Quantities that are directly related to these particles are called microscopic quantities, while quantities that are defined as functions of the entire elementary domain are called macroscopic quantities. The latter are often written as functions of the *centre* \mathbf{x}_c of the elementary domain.

The position of these particles may change in time and is given by $\mathbf{x}^\alpha(t)$ — which is a microscopic quantity. This implies that the particles are chosen sufficiently small — their location is defined by one single point. Since even the smallest known particle occupies a volume, this mathematical requirement can never be met. Therefore, the microscopic quantity $\mathbf{x}^\alpha(t)$ has to be considered as the result of *an* averaging operation. It will be shown later in this section that also the macroscopic quantities

are the result of an averaging operator acting on the microscopic quantities.

Averaging operators are used since it is in general not possible to assign a physical measured quantity to a well-defined point in space-time. Since a device used for measurements has a non-vanishing behaviour in space and time, the measured quantity is an average of the physical function over the measuring domain. Schwartz (1957) introduced the concepts functional and test function. A measured quantity is the result of a functional f acting on a particular test function φ :

$$\langle f, \varphi \rangle = \int_{-\infty}^{+\infty} f(\mathbf{x}, t) \varphi(\mathbf{x}, t) d\mathbf{x} dt. \quad (2.1)$$

The concept of averaging operators is discussed by Schwartz (1957) and Zemanian (1965), and used in wavelet analysis by Herrmann (1997) and Dessim (1997).

If the functional f is chosen to be the position of the evaluated point, the particle position \mathbf{x}^α can be defined as

$$\mathbf{x}^\alpha = \int_{\mathbf{x} \in \mathbb{R}^3} \mathbf{x} \varphi^\alpha(\mathbf{x}) d\mathbf{x} \quad (2.2)$$

where the test function φ^α vanishes outside the particle α .

Each particle has an instantaneous velocity $\mathbf{w}^\alpha(t) [ms^{-1}]$ that is a three-component vector defined as

$$\mathbf{w}^\alpha(t) = d_t \mathbf{x}^\alpha. \quad (2.3)$$

In addition, it is possible to assign a time-independent property to each particle, indicating its mass $m^\alpha [kg]$.

The number of particles in the elementary domain $\mathcal{D}_\epsilon(\mathbf{x}_c)$ is, at a given time t , denoted by $\mathcal{N}_\epsilon(\mathbf{x}_c, t)$, and the volume of the domain is given by $\mathcal{V}_\epsilon(\mathbf{x}_c) [m^3]$ ¹. Note that the number of particles is a time-dependent property, since particles can enter or leave the time-invariant domain. The volume, however, only depends on the geometrical properties of the domain and is therefore time-invariant.

macroscopic quantities

As already been mentioned, macroscopic quantities can be seen as the result of an averaging operator acting on microscopic quantities, by means of

$$M(\mathbf{x}, t) = \langle m, \varphi \rangle \quad (2.4)$$

¹The notation \mathbf{x}_c is used to indicate that the quantity is assigned to the centre of an elementary domain \mathcal{D}_ϵ . It does not only depend on the position of the centre itself, however, but also on the other particles located in the elementary domain. For simplicity, the subscript c will be omitted from here onward.

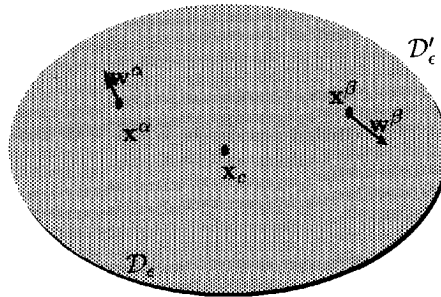


Fig. 2.1 Elementary time-invariant domain \mathcal{D}_ϵ with centre \mathbf{x}_c . \mathbf{x}^α and \mathbf{x}^β are particle positions, and \mathbf{w}^α and \mathbf{w}^β are the instantaneous velocity vectors of the considered particles. The region outside \mathcal{D}_ϵ is denoted by \mathcal{D}'_ϵ .

where M represents a macroscopic function and m represents a microscopic functional.

The test function φ is non-zero in a non-vanishing subdomain of $(\mathbf{x}, t) \in \mathbb{R}^4$. Using the above-mentioned theory, φ will vanish in \mathcal{D}'_ϵ — the region outside the elementary domain \mathcal{D}_ϵ . From Equation (2.4), it is clear that a macroscopic quantity is associated not only with a microscopic quantity, but also with a test-function — or with the size of the elementary domain it is defined over.

The first macroscopic quantity introduced here is the number density $n(\mathbf{x}, t)[\text{m}^{-3}]$, which is defined in a general form as

$$n(\mathbf{x}, t) = \int_{(\mathbf{x}', t') \in \mathbb{R}^4} \varphi(\mathbf{x}', t') \sum_{\alpha=1}^{\mathcal{N}_\epsilon} \delta(\mathbf{x}' - \mathbf{x}^\alpha) d\mathbf{x}' dt'. \quad (2.5)$$

A test function restricts the space-time area where the functional should be evaluated. By choosing the test function as

$$\varphi(\mathbf{x}', t') = \begin{cases} \frac{\delta(t - t')}{\mathcal{V}_\epsilon} & \text{if } \mathbf{x}' \in \mathcal{D}_\epsilon, \\ 0 & \text{if } \mathbf{x}' \in \mathcal{D}'_\epsilon \end{cases} \quad (2.6)$$

it follows from Equation (2.5) that

$$n(\mathbf{x}, t) = \frac{1}{\mathcal{V}_\epsilon} \sum_{\alpha=1}^{\mathcal{N}_\epsilon} \int_{\mathbf{x}' \in \mathcal{D}_\epsilon} \delta(\mathbf{x}' - \mathbf{x}^\alpha) d\mathbf{x}', \quad (2.7)$$

and a more simple definition is obtained:

$$n(\mathbf{x}, t) = \frac{\mathcal{N}_\epsilon(\mathbf{x}, t)}{\mathcal{V}_\epsilon(\mathbf{x})}. \quad (2.8)$$

The number density and the other macroscopic properties in a considered point \mathbf{x} do not only depend on the microscopic quantities in \mathbf{x} , but are the result of an averaging process in a *small* domain \mathcal{D}_ϵ around \mathbf{x} . Indeed, both the number of particles \mathcal{N}_ϵ and the volume \mathcal{V} are defined in and dependent on an elementary domain they are the centre of.

In what follows, it is important that the number density is a piecewise continuous function of the position \mathbf{x} . This is assumed in the continuum hypothesis.

Assumption 1: *Continuum hypothesis*

- The number density function $n(\mathbf{x}, t)$, as defined in Equation (2.8), and the other macroscopic quantities that will be introduced in this section are piecewise continuous functions of \mathbf{x} .

In order for this assumption to be valid, the elementary domain $\mathcal{D}_\epsilon(\mathbf{x})$ has to be chosen sufficiently large that discontinuous spatial variations in the microscopic quantities average over the total elementary domain. On the other hand, $\mathcal{D}_\epsilon(\mathbf{x})$ has to be sufficiently small in order to be able to study the variations of the macroscopic quantities over the domain of interest.

If the continuum hypothesis is satisfied, the total number of particles in a domain \mathcal{D} can be written as

$$\mathcal{N}(\mathcal{D}, t) = \int_{\mathbf{x} \in \mathcal{D}(t)} n(\mathbf{x}, t) d\mathcal{V}. \quad (2.9)$$

The continuum hypothesis is needed here since only piecewise continuous functions are integrable.

A second macroscopic quantity is the volume density of mass $\rho(\mathbf{x}, t)[\text{kgm}^{-3}]$, which is defined as

$$\rho(\mathbf{x}, t) = \frac{1}{\mathcal{V}_\epsilon(\mathbf{x})} \sum_{\alpha=1}^{\mathcal{N}_\epsilon(\mathbf{x}, t)} m^\alpha. \quad (2.10)$$

The drift velocity $\mathbf{v}(\mathbf{x}, t)[\text{ms}^{-1}]$ in the centre of an elementary domain is related to the instantaneous velocity of the particles in the elementary domain by

$$\mathbf{v}(\mathbf{x}, t) = \frac{1}{\mathcal{N}_\epsilon(\mathbf{x}, t)} \sum_{\alpha=1}^{\mathcal{N}_\epsilon(\mathbf{x}, t)} \mathbf{w}^\alpha(t). \quad (2.11)$$

The mass flow density $\phi(\mathbf{x}, t)$ [kg m⁻²s⁻¹] is given by

$$\phi(\mathbf{x}, t) = \frac{1}{\mathcal{V}_\epsilon(\mathbf{x})} \sum_{\alpha=1}^{\mathcal{N}_\epsilon(\mathbf{x}, t)} m^\alpha \mathbf{w}^\alpha(t). \quad (2.12)$$

From this, the mass flow density rate $\dot{\phi}(\mathbf{x}, t)$ [kgm⁻²s⁻²] is introduced via

$$d_t \int_{\mathbf{x} \in \mathcal{D}(t)} \phi(\mathbf{x}, t) dV = \int_{\mathbf{x} \in \mathcal{D}(t)} \dot{\phi}(\mathbf{x}, t) dV, \quad (2.13)$$

where $\mathcal{D}(t)$ is any domain of interest. Note that Equation (2.13) is only valid if $\phi(\mathbf{x}, t)$ is a piecewise continuous function of \mathbf{x} .

particle classification

Until now, all definitions hold for a medium containing elementary particles of any sort. The particles may or may not all have the same microscopic quantities.

In many cases, the particles can be classed in a few types, with each particle of type B having the same mass $m_B^\alpha = m_B$. The classification is evident in the case of a macroscopic homogeneous material that consists of two microscopic structures.

Even if all particles have a different mass, this classification can be done since the number of particles in an elementary domain has to be finite — since they all have a non-zero mass.

The number of particles of type B in the elementary domain $\mathcal{D}_\epsilon(\mathbf{x})$ is denoted by $\mathcal{N}_{\epsilon, B}(\mathbf{x}, t)$. Analogous to the definition in Equation (2.8), the number density of particles of type B is defined by

$$n_B(\mathbf{x}, t) = \frac{\mathcal{N}_{\epsilon, B}(\mathbf{x}, t)}{\mathcal{V}_\epsilon(\mathbf{x})}, \quad (2.14)$$

from which it also follows that the total number density is the sum of the number densities of the different particle types:

$$n(\mathbf{x}, t) = \sum_{B=1}^M n_B(\mathbf{x}, t), \quad (2.15)$$

with M the number of particle-types present in the elementary domain \mathcal{D}_ϵ around the considered point \mathbf{x} .

The volume density of mass for the particles of type B is defined as

$$\begin{aligned} \rho_B(\mathbf{x}, t) &= \frac{1}{\mathcal{V}_\epsilon(\mathbf{x})} \sum_{\alpha=1}^{\mathcal{N}_{\epsilon, B}(\mathbf{x}, t)} m_B \\ &= n_B(\mathbf{x}, t) m_B, \end{aligned} \quad (2.16)$$

where use is made of Equation (2.14).

The total volume density of mass can now be written as the sum of the volume densities of mass for the different particle types:

$$\begin{aligned}\rho(\mathbf{x}, t) &= \frac{1}{\mathcal{V}_\epsilon(\mathbf{x})} \sum_{B=1}^M m_B \mathcal{N}_{\epsilon, B}(\mathbf{x}, t) \\ &= \sum_{B=1}^M m_B n_B(\mathbf{x}, t) \\ &= \sum_{B=1}^M \rho_B(\mathbf{x}, t).\end{aligned}\quad (2.17)$$

According to the definition of particle-types, the particles of type B have the same mass, but their instantaneous velocity may still vary. The drift velocity for particles of type B is given by

$$\mathbf{v}_B(\mathbf{x}, t) = \frac{1}{\mathcal{N}_{\epsilon, B}(\mathbf{x}, t)} \sum_{\alpha=1}^{\mathcal{N}_{\epsilon, B}(\mathbf{x}, t)} \mathbf{w}_B^\alpha(t). \quad (2.18)$$

The mass flow density for the particles of type B is defined as

$$\phi_B(\mathbf{x}, t) = \frac{1}{\mathcal{V}_\epsilon(\mathbf{x})} \sum_{\alpha=1}^{\mathcal{N}_{\epsilon, B}(\mathbf{x}, t)} m_B \mathbf{w}_B^\alpha(t), \quad (2.19)$$

or, using Equations (2.16), (2.14) and (2.18),

$$\phi_B(\mathbf{x}, t) = \rho_B(\mathbf{x}, t) \mathbf{v}_B(\mathbf{x}, t). \quad (2.20)$$

Using Equations (2.12) and (2.19), the total mass flow density is now written as the sum of the mass flow densities of the different particle types:

$$\phi(\mathbf{x}, t) = \sum_{B=1}^M \phi_B(\mathbf{x}, t). \quad (2.21)$$

2.1.2 The equation of motion

In a fluid, volume forces act on each particle. A typical force is the gravitational force, acting on each particle, but also other types of forces may be present -- e.g. external sources. The volume density of volume force is given by $\mathbf{f}(\mathbf{x}, t)$ [Nm⁻³]. If this quantity is a piecewise continuous function of \mathbf{x} , the total volume force \mathbf{F}^V in a domain \mathcal{D} can be written as

$$\mathbf{F}^V(\mathcal{D}, t) = \int_{\mathbf{x} \in \mathcal{D}(t)} \mathbf{f}(\mathbf{x}, t) dV. \quad (2.22)$$

Surface forces acting on the boundary $\partial\mathcal{D}$ of a domain \mathcal{D} are caused by a traction vector $\mathbf{t}(\mathbf{x}, t)$. If this traction is a piecewise continuous function over the boundary $\partial\mathcal{D}$, the surface force \mathbf{F}^S can be written as

$$\mathbf{F}^S(\mathcal{D}, t) = \int_{\mathbf{x} \in \partial\mathcal{D}(t)} \mathbf{t}(\mathbf{x}, t) dA. \quad (2.23)$$

According to Newton, the net result of surface and volume forces causes a change in the linear momentum of a fluid:

$$\mathbf{F}^V + \mathbf{F}^S = d_t \mathcal{M} \quad (2.24)$$

The linear momentum of a particle is defined as the product of its mass and its velocity.

Another assumption will be made now:

Assumption 2: superposition of the linear momentum of particles

- The linear momentum of a fluid in a domain \mathcal{D} is the superposition of the linear momentum of the particles in the considered domain.

The domain \mathcal{D} is subdivided into a number $N(t)$ elementary subdomains \mathcal{D}_ϵ , each consisting of N_ϵ particles. In this case, the total linear momentum of the fluid in domain \mathcal{D} at that moment is written as

$$\mathcal{M}(\mathcal{D}, t) = \sum_{\epsilon=1}^{N(t)} \left(\sum_{\alpha=1}^{N_\epsilon} m^\alpha \mathbf{w}_\epsilon^\alpha \right) \quad (2.25)$$

Using the particle-type classification, this can be written as

$$\begin{aligned} \mathcal{M}(\mathcal{D}, t) &= \sum_{\epsilon=1}^{N(t)} \left(\sum_{B=1}^M \left(m_B \sum_{\alpha=1}^{N_{\epsilon,B}} \mathbf{w}_{\epsilon,B}^\alpha \right) \right) \\ &= \sum_{\epsilon=1}^{N(t)} \left(\sum_{B=1}^M m_B n_{\epsilon,B}(t) \mathbf{v}_{\epsilon,B}(t) \right) \mathcal{V}_\epsilon \end{aligned} \quad (2.26)$$

where use is made of Equations (2.18) and (2.14). Substituting Equations (2.16), (2.20) and (2.21) in Equation (2.26) gives

$$\mathcal{M}(\mathcal{D}, t) = \sum_{\epsilon=1}^{N(t)} \phi_\epsilon(t) \mathcal{V}_\epsilon. \quad (2.27)$$

Since summation has to be done over elementary small domains, it can be replaced by integration:

$$\mathcal{M}(\mathcal{D}, t) = \int_{\mathbf{x} \in \mathcal{D}(t)} \phi(\mathbf{x}, t) dV. \quad (2.28)$$

Newton's law — Equation (2.24) — can now be written as

$$\int_{\mathbf{x} \in \mathcal{D}(t)} \mathbf{f}(\mathbf{x}, t) dV + \int_{\mathbf{x} \in \partial \mathcal{D}(t)} \mathbf{t}(\mathbf{x}, t) dA = d_t \int_{\mathbf{x} \in \mathcal{D}(t)} \phi(\mathbf{x}, t) dV. \quad (2.29)$$

Using Equation (2.13), this can be written as

$$\int_{\mathbf{x} \in \mathcal{D}(t)} \mathbf{f}(\mathbf{x}, t) dV + \int_{\mathbf{x} \in \partial \mathcal{D}(t)} \mathbf{t}(\mathbf{x}, t) dA = \int_{\mathbf{x} \in \mathcal{D}(t)} \dot{\phi}(\mathbf{x}, t) dV. \quad (2.30)$$

In non-viscous fluids, the traction has only a component perpendicular to the surface the force acts on. In this case, the traction is given by

$$\mathbf{t}(\mathbf{x}, t) = -p(\mathbf{x}, t) \boldsymbol{\nu}(\mathbf{x}, t), \quad (2.31)$$

where p is the acoustic pressure in the point \mathbf{x} at time t and $\boldsymbol{\nu}$ is the unit vector perpendicular to the boundary element dA .

Assuming that $p(\mathbf{x}, t)$ is defined everywhere in the domain \mathcal{D} , and that $p(\mathbf{x}, t)$ is a continuous differentiable function of \mathbf{x} , Gauss' integral theorem can be applied to convert the boundary integral in the left-hand-side of Equation (2.30) into a volume integral. Equation (2.30) then becomes

$$\int_{\mathbf{x} \in \mathcal{D}(t)} \left(\nabla p(\mathbf{x}, t) + \dot{\phi}(\mathbf{x}, t) \right) dV = \int_{\mathbf{x} \in \mathcal{D}(t)} \mathbf{f}(\mathbf{x}, t) dV. \quad (2.32)$$

Since Equation (2.32) holds for any domain $\mathcal{D}(t)$, it follows that

$$\partial_k p(\mathbf{x}, t) + \dot{\phi}_k(\mathbf{x}, t) = f_k(\mathbf{x}, t). \quad (2.33)$$

which is the local form of the equation of motion. After a temporal Fourier transform, this equation can be written in the frequency domain as

$$\partial_k P(\mathbf{x}, \omega) + \dot{\Phi}_k(\mathbf{x}, \omega) = F_k(\mathbf{x}, \omega). \quad (2.34)$$

Equations (2.33) and (2.34) mean that a spatial variation of the acoustic pressure is related to a temporal variation of the linear momentum and a volume force acting on the medium.

2.1.3 The deformation equation

The change in volume of a time-variant domain $\mathcal{D}(t)$ is related to the drift velocity at the boundary of the specified volume through

$$d_t \mathcal{V}(t) = \int_{\mathbf{x} \in \partial \mathcal{D}(t)} v_k(\mathbf{x}, t) \nu_k(\mathbf{x}, t) dA, \quad (2.35)$$

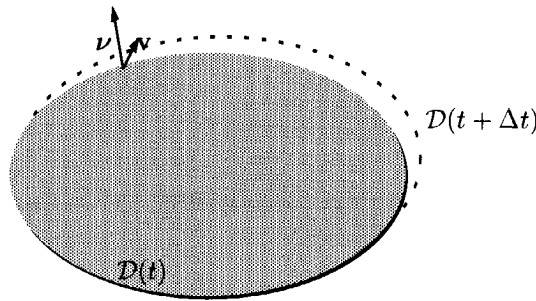


Fig. 2.2 Volume change in an elementary domain.

where ν is the unit normal vector perpendicular on the boundary $\partial\mathcal{D}$. This process is illustrated in Figure 2.2. Equation (2.35) only makes sense when the drift velocity $\mathbf{v}(\mathbf{x}, t)$ is defined in each point at the boundary $\partial\mathcal{D}$ and $\mathbf{v}(\mathbf{x}, t)$ is a piecewise continuous function of \mathbf{x} . Furthermore, if $\mathbf{v}(\mathbf{x}, t)$ is continuously differentiable throughout \mathcal{D} , the volume change can be written as

$$d_t \mathcal{V}(t) = \int_{\mathbf{x} \in \mathcal{D}(t)} \partial_k v_k(\mathbf{x}, t) dV \quad (2.36)$$

where Gauss' integral theorem has been used to convert the boundary integral in Equation (2.35) into a volume integral.

The presence of a source — i.e. an acoustic transducer — can cause the volume of a domain to change. The volume source density of volume injection rate $q(\mathbf{x}, t)[\text{s}^{-1}]$ is a quantity describing the rate the considered domain is changing due to the presence of a source. The cubic dilatation rate is not only influenced by a source, but has also an induced part, due to the state quantities of the acoustic wave motion. This induced part of the cubic dilatation rate is denoted by $\dot{\theta}(\mathbf{x}, t)[\text{s}^{-1}]$. The total cubic dilatation rate is now written as:

$$d_t \mathcal{V}(t) = \int_{\mathbf{x} \in \mathcal{D}(t)} \dot{\theta}(\mathbf{x}, t) dV + \int_{\mathbf{x} \in \mathcal{D}(t)} q(\mathbf{x}, t) dV. \quad (2.37)$$

By combining Equations (2.36) and (2.37), the deformation equation can be written as

$$\int_{\mathbf{x} \in \mathcal{D}(t)} [\partial_k v_k(\mathbf{x}, t) - \dot{\theta}(\mathbf{x}, t)] dV = \int_{\mathbf{x} \in \mathcal{D}(t)} q(\mathbf{x}, t) dV. \quad (2.38)$$

Since Equation (2.38) holds for any domain \mathcal{D} , it follows that

$$\partial_k v_k(\mathbf{x}, t) - \dot{\theta}(\mathbf{x}, t) = q(\mathbf{x}, t), \quad (2.39)$$

which is the local form of the deformation equation.

In the frequency domain, this becomes

$$\partial_k V_k(\mathbf{x}, \omega) - \dot{\Theta}(\mathbf{x}, \omega) = Q(\mathbf{x}, \omega). \quad (2.40)$$

Equations (2.39) and (2.40) mean that the presence of an injection source is compensated for by a spatial variation of the drift velocity and a variation of the induced part of the cubic dilation.

2.1.4 The constitutive coefficients in a time-invariant medium

Equations (2.33) and (2.39) — or their frequency domain counterparts (2.34) and (2.40) — give an expression for the wavefield parameters p and \mathbf{v} as a function of source distributions \mathbf{f} and q . However, the microscopic material properties are implicitly still present in this equation, due to the expression for the mass flow density rate $\dot{\phi}_k$ — definition (2.12) and Equation (2.13) — and the cubic dilation rate $\dot{\theta}$. In this subsection, these wavefield quantities are related to the wavefield parameters \mathbf{v} and p , by means of the constitutive equations.

From the analysis in subsection 2.1.2 it follows that the change in linear momentum of a fluid in a domain \mathcal{D} can be written as

$$\begin{aligned} d_t \mathcal{M}(\mathcal{D}, t) &= d_t \int_{\mathbf{x} \in \mathcal{D}(t)} \sum_{B=1}^M m_B n_B(\mathbf{x}, t) \mathbf{v}_B(\mathbf{x}, t) \\ &= d_t \int_{\mathbf{x} \in \mathcal{D}(t)} \sum_{B=1}^M \rho_B(\mathbf{x}, t) \mathbf{v}_B(\mathbf{x}, t). \end{aligned} \quad (2.41)$$

A new assumption is made now:

Assumption 3: conservation of number of particles

- Particles are neither created nor annihilated. Particles from one type can not transform into particles from another type.

This assumption puts new restrictions on the definition of "particles". The validity of this assumption depends on the definition of particles and on the nature of the considered processes. If one chooses a molecule to be the definition of the particle, it is clear that Assumption 3 will not be satisfied when the process under consideration consists of molecular transformations.

If Assumption 3 is valid, it holds that² for a quantity $\psi_B(\mathbf{x}, t)$

$$d_t \int_{\mathbf{x} \in \mathcal{D}(t)} n_B(\mathbf{x}, t) \psi_B(\mathbf{x}, t) d\mathcal{V} = \int_{\mathbf{x} \in \mathcal{D}(t)} n_B(\mathbf{x}, t) D_t \psi_B(\mathbf{x}, t) d\mathcal{V}, \quad (2.42)$$

where the co-moving time derivative D_t is defined as

$$D_t = \partial_t + v_k \partial_k. \quad (2.43)$$

As a consequence, it follows from Equation (2.41) that

$$\begin{aligned} d_t \mathcal{M}(\mathcal{D}, t) &= \sum_{B=1}^M \int_{\mathbf{x} \in \mathcal{D}(t)} n_B(\mathbf{x}, t) D_t m_B \mathbf{v}_B(\mathbf{x}, t) d\mathcal{V} \\ &= \sum_{B=1}^M \int_{\mathbf{x} \in \mathcal{D}(t)} \rho_B(\mathbf{x}, t) D_t \mathbf{v}_B(\mathbf{x}, t) d\mathcal{V}. \end{aligned} \quad (2.44)$$

Also, combining Equations (2.13), (2.20), (2.21) and (2.41) gives

$$d_t \mathcal{M}(\mathcal{D}, t) = \int_{\mathbf{x} \in \mathcal{D}(t)} \dot{\phi}(\mathbf{x}, t) d\mathcal{V}. \quad (2.45)$$

Since Equations (2.44) and (2.45) hold for any domain \mathcal{D} , it follows that an explicit expression for the mass flow density rate can now be given by

$$\dot{\phi}(\mathbf{x}, t) = \sum_{B=1}^M \rho_B(\mathbf{x}, t) D_t \mathbf{v}_B(\mathbf{x}, t). \quad (2.46)$$

This expression is still difficult to treat, due to the particle type dependent drift velocity $\mathbf{v}_B(\mathbf{x}, t)$. In many practical cases, though, the next assumption is very reasonable:

Assumption 4: common collective motion

■ The particles of different types all have the same drift velocity: $\mathbf{v}_B = \mathbf{v}$

This assumption can be satisfied by mechanical interactions between the different substances, preventing them from separating from each other.

Using this assumption, Equation (2.46) can be written as

$$\dot{\phi}(\mathbf{x}, t) = \rho(\mathbf{x}, t) D_t \mathbf{v}(\mathbf{x}, t), \quad (2.47)$$

where use is made of Equation (2.17).

²A proof of this can be found in De Hoop (1995).

According to Equation (2.47), the mass flow density rate depends only on the drift velocity \mathbf{v} , and not on the pressure p . Similarly, it is often assumed that the induced part of the cubic dilation rate only depends on the pressure p and not on the drift velocity \mathbf{v} , and has the form

$$\dot{\theta}(\mathbf{x}, t) = -\kappa(\mathbf{x}, t)D_t p(\mathbf{x}, t), \quad (2.48)$$

where $\kappa(\mathbf{x}, t)[\text{Pa}^{-1}]$ is the compressibility of the fluid for a given time and position.

In a time invariant medium, the constitutive parameters are time independent. As a consequence, Equations (2.47) and (2.48) are written as

$$\dot{\phi}(\mathbf{x}, t) = \rho(\mathbf{x})D_t \mathbf{v}(\mathbf{x}, t). \quad (2.49)$$

and

$$\dot{\theta}(\mathbf{x}, t) = -\kappa(\mathbf{x})D_t p(\mathbf{x}, t). \quad (2.50)$$

In some media, the different particle types do not have the same drift velocity \mathbf{v} . Depending on their material state, the particles of one constituent may undergo a large displacement with respect to the motion of the particles of another constituent. This is the case, for example, when a medium consists of a two fluids with a different acoustic velocity. Assumption (4) is not satisfied then, and Equations (2.47) and (2.48) no longer hold.

Equations (2.49) and (2.50) assume that the constitutive parameters at time t depend only on the wavefield parameters at the same time.

A more general form of the constitutive equations is given by

$$\dot{\phi}(\mathbf{x}, t) = \int_{t' \in \mathcal{R}} \mu(\mathbf{x}, t')D_t \mathbf{v}(\mathbf{x}, t - t')dt' \quad (2.51)$$

and

$$\dot{\theta}(\mathbf{x}, t) = - \int_{t' \in \mathcal{R}} \chi(\mathbf{x}, t')D_t p(\mathbf{x}, t - t')dt'. \quad (2.52)$$

Note the introduction of the inertia relaxation function $\mu(\mathbf{x}, t)[\text{kgm}^{-3}\text{s}^{-1}]$ and the compliance relaxation function $\chi(\mathbf{x}, t)[\text{Pa}^{-1}\text{s}^{-1}]$.

Since these relaxation functions in the right-hand side of Equations (2.51) and (2.52) only depend on relative times — the time difference between *cause* at $t - t'$ and *observation* at t , the medium is assumed to be time-invariant.

Causality implies that the values of $\{\dot{\phi}, \dot{\theta}\}$ at a given time t can not be influenced by the values of the wavefield at a time later than t . Hence, the equations (2.51)

and (2.52) become

$$\dot{\phi}(\mathbf{x}, t) = \int_{t'=0}^{\infty} \mu(\mathbf{x}, t') D_t \mathbf{v}(\mathbf{x}, t - t') dt' \quad (2.53)$$

and

$$\dot{\theta}(\mathbf{x}, t) = - \int_{t'=0}^{\infty} \chi(\mathbf{x}, t') D_t p(\mathbf{x}, t - t') dt'. \quad (2.54)$$

When the medium is instantaneously reacting, it holds that

$$\mu(\mathbf{x}, t) = \rho(\mathbf{x}) \delta(t) \quad (2.55)$$

and

$$\chi(\mathbf{x}, t) = \kappa(\mathbf{x}) \delta(t), \quad (2.56)$$

so that Equations (2.53) and (2.54) reduce to Equations (2.49) and (2.50).

2.1.5 Low-velocity approximation

The expressions for the mass flow density rate — Equations (2.49) and (2.53) — and the induced part of the cubic dilation rate — Equations (2.50) and (2.54) — are rather difficult to handle due to the presence of the co-moving time derivative D_t . In many applications, though, this co-moving time derivative is simplified.

Intuitively, it can be seen that in the expression

$$D_t p(\mathbf{x}, t) = \partial_t p(\mathbf{x}, t) + v_k \partial_k p(\mathbf{x}, t) \quad (2.57)$$

the second term will be much smaller than the first term when the static equilibrium is disturbed by a relatively fast fluctuation with a relatively small amplitude. In most ultrasonic and seismic situations, this condition is satisfied. In this case, it is reasonable to replace equation (2.43) by the approximation

$$D_t = \partial_t. \quad (2.58)$$

A further analysis of this low-velocity linearisation is given by De Hoop (1995).

2.2 Instantaneously reacting medium

For an instantaneously reacting medium, the expressions for the mass flow density rate $\dot{\phi}_k$ — Equation (2.49) — and the cubic dilation rate $\dot{\theta}$ — Equation (2.50) — are rather simple expressions, especially when using the low-velocity linearisation (2.58).

Although the basic equations are very general, they will be solved here for the case of a one-dimensional plane wave. In this section, an expression will be derived for calculating the plane wavefield at a point in a homogeneous medium, based on the plane wavefield in another point in the same medium.

2.2.1 General wave equation

Using the low-velocity approximation as expressed in equation (2.58), the constitutive relations for an instantaneously reacting medium — equations (2.49) and (2.50) — are simplified to

$$\dot{\phi}_k(\mathbf{x}, t) = \rho(\mathbf{x}) \partial_t v_k(\mathbf{x}, t) \quad (2.59)$$

and

$$\dot{\theta}(\mathbf{x}, t) = -\kappa(\mathbf{x}) \partial_t p(\mathbf{x}, t). \quad (2.60)$$

Using these relations in the equation of motion (2.33) and the deformation equation (2.39), the basic equations become

$$\partial_k p(\mathbf{x}, t) + \rho(\mathbf{x}) \partial_t v_k(\mathbf{x}, t) = f_k(\mathbf{x}, t) \quad (2.61)$$

and

$$\partial_k v_k(\mathbf{x}, t) + \kappa(\mathbf{x}) \partial_t p(\mathbf{x}, t) = q(\mathbf{x}, t). \quad (2.62)$$

Applying a Fourier-transformation to equations (2.61) and (2.62) leads to

$$\partial_k P(\mathbf{x}, \omega) + j\omega \rho(\mathbf{x}) V_k(\mathbf{x}, \omega) = F_k(\mathbf{x}, \omega) \quad (2.63)$$

and

$$\partial_k V_k(\mathbf{x}, \omega) + j\omega \kappa(\mathbf{x}) P(\mathbf{x}, \omega) = Q(\mathbf{x}, \omega). \quad (2.64)$$

When no sources are present, Equations (2.63) and (2.64) become

$$\partial_k P(\mathbf{x}, \omega) + j\omega \rho(\mathbf{x}) V_k(\mathbf{x}, \omega) = 0 \quad (2.65)$$

and

$$\partial_k V_k(\mathbf{x}, \omega) + j\omega \kappa(\mathbf{x}) P(\mathbf{x}, \omega) = 0. \quad (2.66)$$

From Equation (2.65) it follows that

$$\partial_k V_k(\mathbf{x}, \omega) = -\frac{1}{j\omega \rho(\mathbf{x})} (\partial_k \partial_k P(\mathbf{x}, \omega) - \partial_k P(\mathbf{x}, \omega) \partial_k \ln \rho(\mathbf{x})). \quad (2.67)$$

Using this in (2.66) leads to

$$\partial_k \partial_k P(\mathbf{x}, \omega) + \left(\frac{\omega}{c(\mathbf{x})} \right)^2 P(\mathbf{x}, \omega) - \partial_k P(\mathbf{x}, \omega) \partial_k \ln \rho(\mathbf{x}) = 0 \quad (2.68)$$

where the acoustic velocity c is defined as

$$c(\mathbf{x}) = \frac{1}{\sqrt{\kappa(\mathbf{x})\rho(\mathbf{x})}}. \quad (2.69)$$

Homogeneous medium

A fluid is homogeneous if the constitutive parameters are shift-invariant. Since in this case $\rho(\mathbf{x}) = \rho$ and $\kappa(\mathbf{x}) = \kappa$ — and hence $c(\mathbf{x}) = c = (\kappa\rho)^{-1/2}$ —, Equation (2.68) transforms into the Helmholtz equation:

$$\partial_k \partial_k P(\mathbf{x}, \omega) + \left(\frac{\omega}{c} \right)^2 P(\mathbf{x}, \omega) = 0. \quad (2.70)$$

2.2.2 Plane wave theory

In this subsection, the seismic convention will be used where one axis, the x_3 or z -axis, points downward into the material — in seismics, the earth. If the pressure only varies along the z -axis and if the medium is homogeneous in a considered domain, the Helmholtz equation (2.70) is written as

$$\partial_z^2 P(z, \omega) + \left(\frac{\omega}{c} \right)^2 P(z, \omega) = 0. \quad (2.71)$$

The general solution of this differential equation is well known and given by

$$P(z, \omega) = P^+(z, \omega) + P^-(z, \omega), \quad (2.72)$$

with

$$P^\pm(z, \omega) = \bar{P}^\pm(\omega) \exp(\mp j\omega z/c), \quad (2.73)$$

where $\bar{P}^+(\omega)$ and $\bar{P}^-(\omega)$ are space-independent parameters. These parameters are determined by boundary-conditions, leading to a particular solution for a given problem.

In the time domain, the solution is written as

$$p(z, t) = p^+(t - z/c) + p^-(t + z/c). \quad (2.74)$$

The two terms in Equations (2.72) as well as (2.74) represent two plane waves.

A wavefront is defined to be the combination of points in space-time where the considered wave function has a constant value. Following the seismic conventions,

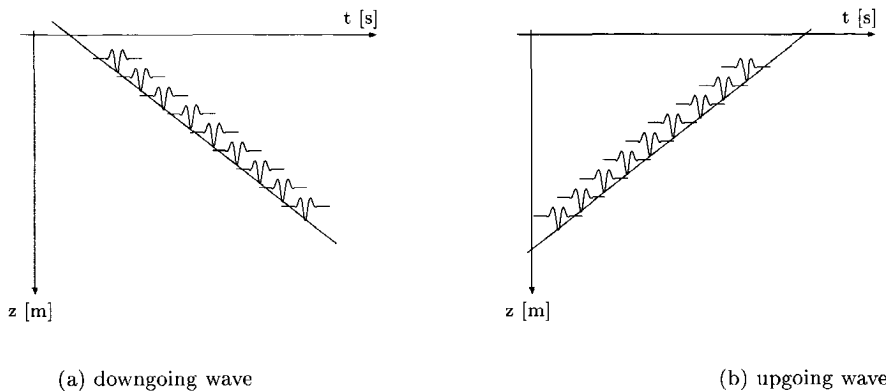


Fig. 2.3 Downgoing and upgoing plane waves. The straight line represents a *downgoing wave*, since its wavefront — given by

$$z = ct - u, \quad (2.75)$$

with u a constant value, "travels" downward into the material. This means that for increasing time, the wavefront will be located at a larger value of z — deeper into the target.

For the same reason, $P^-(z, \omega)$ or its time-representation $p^-(t + z/c)$ is called an upgoing wave. This principle is clarified in Figure 2.3.

Consider two points in a homogeneous medium, at different depths z_A and z_B , where $z_B > z_A$. The pressure at these points due to the presence of a downgoing wave are in the frequency domain given by

$$P^+(z_A, \omega) = \bar{P}^+(\omega) \exp(-j\omega z_A/c) \quad (2.76)$$

and

$$P^+(z_B, \omega) = \bar{P}^+(\omega) \exp(-j\omega z_B/c). \quad (2.77)$$

It follows that, when the pressure at a given depth z_A is known, the pressure at a different depth z_B can be expressed as

$$P^+(z_B, \omega) = P^+(z_A, \omega) \exp\left(-j\omega \frac{z_B - z_A}{c}\right). \quad (2.78)$$

The propagation factor W is now defined as

$$W(\omega, \Delta z) = \exp\left(-j\omega \frac{\Delta z}{c}\right). \quad (2.79)$$

Using this definition, Equation (2.78) becomes

$$P^+(z_B, \omega) = P^+(z_A, \omega)W(\omega, z_B - z_A). \quad (2.80)$$

An analogous derivation for the upgoing wavefield leads to

$$P^-(z_A, \omega) = P^-(z_B, \omega)W(\omega, z_B - z_A). \quad (2.81)$$

Specific acoustic impedance

In the following, $V(z, \omega)$ is a short notation for $V_3(\mathbf{x}, \omega)$, the only non-zero component of $\mathbf{V}(\mathbf{x}, \omega)$ in the considered situation. From Equations (2.72), (2.73) and (2.65), it follows that

$$V(z, \omega) = V^+(z, \omega) + V^-(z, \omega), \quad (2.82)$$

where

$$V^\pm(z, \omega) = \bar{V}^\pm(\omega) \exp(\mp j\omega z/c), \quad (2.83)$$

with

$$\bar{V}^\pm(\omega) = \pm \frac{1}{\rho c} \bar{P}^\pm(\omega). \quad (2.84)$$

The specific acoustic impedance for a down- or upgoing plane wave is defined by

$$Z^\pm(z, \omega) = \frac{P^\pm(z, \omega)}{V^\pm(z, \omega)}. \quad (2.85)$$

Using Equation (2.84), the specific acoustic impedance for a plane wave in an instantaneously reacting medium is given by

$$Z^\pm = \pm \rho c. \quad (2.86)$$

2.3 Medium with relaxation

In this section, wave propagation in a medium with relaxation is studied. In such a medium, acoustic energy is irreversibly converted into another form — and therefore dissipated. The phenomena that cause this behaviour are very complex. For a study

of relaxation effects and consequences, the reader is referred to the literature — e.g. Toksoz and Johnston (1981) and Tolstoy (1992). In this thesis, the approach of De Hoop (1995) is followed.

Although the wave propagation operator in a medium with relaxation is different from the wave propagation operator in an instantaneously reacting medium, the expressions for the upgoing and downgoing wavefield can have the same form as they have in an instantaneously reacting medium.

2.3.1 General wave equation

Equations (2.53) and (2.54) incorporate causality in a medium with relaxation, but are very general.

Therefore, in practical cases, the constitutive equations are expanded with terms that account for the conversion of acoustic energy into another form. In the case of an isotropic medium with dissipation of acoustic energy into heat, the constitutive equations are often written as — using the low-velocity approximation

$$\dot{\phi}_k(\mathbf{x}, t) = K(\mathbf{x})v_k(\mathbf{x}, t) + \rho(\mathbf{x})\partial_t v_k(\mathbf{x}, t) \quad (2.87)$$

and

$$\dot{\theta}(\mathbf{x}, t) = -\Gamma(\mathbf{x})p(\mathbf{x}, t) - \kappa(\mathbf{x})\partial_t p(\mathbf{x}, t), \quad (2.88)$$

where K is the coefficient of frictional force and Γ is the coefficient of bulk inviscidness. It will be shown later in this section that the introduction of these terms indeed leads to the conversion of acoustic energy into dissipated energy.

In the frequency domain, these constitutive equations are given by

$$\dot{\Phi}(\mathbf{x}, \omega) = (K(\mathbf{x}) + j\omega\rho(\mathbf{x})) \mathbf{V}(\mathbf{x}, \omega) \quad (2.89)$$

and

$$\dot{\Theta}(\mathbf{x}, \omega) = -(\Gamma(\mathbf{x}) + j\omega\kappa(\mathbf{x})) P(\mathbf{x}, \omega). \quad (2.90)$$

Using the constitutive Equations (2.87) and (2.88) in the equation of motion (2.33) and the deformation equation (2.39), the basic equations become

$$\partial_k p(\mathbf{x}, t) + \rho(\mathbf{x})\partial_t v_k(\mathbf{x}, t) + K(\mathbf{x})v_k(\mathbf{x}, t) = f_k(\mathbf{x}, t) \quad (2.91)$$

and

$$\partial_k v_k(\mathbf{x}, t) + \kappa(\mathbf{x})\partial_t p(\mathbf{x}, t) + \Gamma(\mathbf{x})p(\mathbf{x}, t) = q(\mathbf{x}, t). \quad (2.92)$$

Applying a Fourier-transformation to equations (2.91) and (2.92) leads to

$$\partial_k P(\mathbf{x}, \omega) + j\omega \rho(\mathbf{x}) V_k(\mathbf{x}, \omega) + K(\mathbf{x}) V_k(\mathbf{x}, \omega) = F_k(\mathbf{x}, \omega) \quad (2.93)$$

and

$$\partial_k V_k(\mathbf{x}, \omega) + j\omega \kappa(\mathbf{x}) P(\mathbf{x}, \omega) + \Gamma(\mathbf{x}) P(\mathbf{x}, \omega) = Q(\mathbf{x}, \omega). \quad (2.94)$$

When no sources are present, equations (2.93) and (2.94) become

$$\partial_k P(\mathbf{x}, \omega) + j\omega \rho(\mathbf{x}) V_k(\mathbf{x}, \omega) + K(\mathbf{x}) V_k(\mathbf{x}, \omega) = 0 \quad (2.95)$$

and

$$\partial_k V_k(\mathbf{x}, \omega) + j\omega \kappa(\mathbf{x}) P(\mathbf{x}, \omega) + \Gamma(\mathbf{x}) P(\mathbf{x}, \omega) = 0. \quad (2.96)$$

Defining the generalised density $\hat{\rho}(\mathbf{x}, \omega)$ and the generalised compressibility $\hat{\kappa}(\mathbf{x}, \omega)$ as

$$\hat{\rho}(\mathbf{x}, \omega) = \rho(\mathbf{x}) + \frac{1}{j\omega} K(\mathbf{x}) \quad (2.97)$$

and

$$\hat{\kappa}(\mathbf{x}, \omega) = \kappa(\mathbf{x}) + \frac{1}{j\omega} \Gamma(\mathbf{x}), \quad (2.98)$$

Equations (2.95) and (2.96) can be written as

$$\partial_k P(\mathbf{x}, \omega) + j\omega \hat{\rho}(\mathbf{x}, \omega) V_k(\mathbf{x}, \omega) = 0 \quad (2.99)$$

and

$$\partial_k V_k(\mathbf{x}, \omega) + j\omega \hat{\kappa}(\mathbf{x}, \omega) P(\mathbf{x}, \omega) = 0. \quad (2.100)$$

Homogeneous medium

In the case of a homogeneous medium, the combination of Equations (2.95) and (2.96) leads to

$$\partial_k \partial_k P(\mathbf{x}, \omega) + \left(\frac{\omega^2}{c^2} - K\Gamma - j\omega(\rho\Gamma + \kappa K) \right) P(\mathbf{x}, \omega) = 0, \quad (2.101)$$

with the acoustic propagation velocity c defined in Equation (2.69). A solution of this equation for a lateral invariant medium will be given in subsection 2.3.2. Using the generalised density $\hat{\rho}(\omega)$ and the generalised compressibility $\hat{\kappa}(\omega)$, it follows from Equations (2.99) and (2.100) that Equation (2.101) can also be written as

$$\partial_k \partial_k P(\mathbf{x}, \omega) + \left(\frac{\omega}{\hat{c}} \right)^2 P(\mathbf{x}, \omega) = 0, \quad (2.102)$$

with the generalised acoustic velocity defined as

$$\hat{c} = \frac{1}{\sqrt{\hat{\kappa}\hat{\rho}}}. \quad (2.103)$$

Energy considerations

At this point, it will be shown that the presence of the coefficient of frictional force K and the coefficient of bulk inviscidness Γ in the constitutive equations lead to the dissipation of acoustic energy.

Multiplying Equation (2.91) with $v_k(\mathbf{x}, t)$ and Equation (2.92) with $p(\mathbf{x}, t)$, and adding the results leads to

$$\partial_k(pv_k) + \partial_t \left(\rho \frac{v_k v_k}{2} + \kappa \frac{p^2}{2} \right) + Kv_k v_k + \Gamma p^2 = f_k v_k + qp. \quad (2.104)$$

After integration of Equation (2.104) over any time invariant domain \mathcal{D} where Equations (2.91) and (2.92) hold, it follows that

$$\int_{\partial\mathcal{D}} p v_k \nu_k dA + \partial_t \int_{\mathcal{D}} \left(\rho \frac{v_k v_k}{2} + \kappa \frac{p^2}{2} \right) dV + \int_{\mathcal{D}} \dot{Q}^d dV = \dot{W}^{\text{ext}}, \quad (2.105)$$

where Gauss' theorem has been used to convert the volume integral to the boundary integral in the first term of Equation (2.105). The volume density of dissipated power and the total acoustic power delivered by the sources are given by respectively

$$\dot{Q}^d = Kv_k v_k + \Gamma p^2 \quad (2.106)$$

and

$$\dot{W}^{\text{ext}} = \int_{\mathcal{D}} (f_k v_k + qp) dV. \quad (2.107)$$

Based on Equation (2.105), the following energy equation can be deduced:

$$P^a + \partial_t (W^{\text{kin}} + W^{\text{def}}) + P^d = \dot{W}^{\text{ext}}, \quad (2.108)$$

with P^a the net acoustic power flow across $\partial\mathcal{D}$, and defined as

$$P^a = \int_{\partial\mathcal{D}} p v_k \nu_k dA. \quad (2.109)$$

Further, the kinetic energy of the acoustic wavefield in the domain \mathcal{D} , and the deformation energy stored in the acoustic wavefield in this domain are defined by, respectively

$$W^{\text{kin}} = \int_{\mathcal{D}} \rho \frac{v_k v_k}{2} dV \quad (2.110)$$

and

$$W^{\text{def}} = \int_{\mathcal{D}} \kappa \frac{p^2}{2} dV. \quad (2.111)$$

The term P^d is the acoustic power dissipated in \mathcal{D} and is given by

$$P^d = \int_{\mathbf{x} \in \mathcal{D}} \dot{Q}^d dV. \quad (2.112)$$

It follows that when both K and Γ are zero, the dissipated acoustic power vanishes and the energy delivered by the sources is converted into kinetic and deformation energy stored in the acoustic wave field in \mathcal{D} and into an acoustic power flow through the boundary of the considered domain.

Since acoustic losses can not lead to an increase of the energy in the domain, both K and Γ must be non-negative.

2.3.2 Plane wave theory

In this subsection, the same conventions as in subsection 2.2.2 will be used. If the pressure only varies along the z -axis, the wave equation (2.101) is written as

$$\partial_z^2 P(z, \omega) + \left(\frac{\omega^2}{c^2} - K\Gamma - j\omega(\rho\Gamma + \kappa K) \right) P(z, \omega) = 0. \quad (2.113)$$

The general solution for this differential equation is given by

$$P(z, \omega) = P^+(z, \omega) + P^-(z, \omega), \quad (2.114)$$

with

$$P^+(z, \omega) = \bar{P}^+(\omega) \exp(\gamma_2 z) \quad (2.115)$$

$$P^-(z, \omega) = \bar{P}^-(\omega) \exp(\gamma_1 z), \quad (2.116)$$

where γ_1 and γ_2 are the roots of

$$-\gamma^2 = \omega^2 \rho \kappa - K\Gamma - j\omega(\rho\Gamma + \kappa K). \quad (2.117)$$

Using the generalised acoustic velocity \hat{c} as defined in Equation (2.103), the down- and upgoing waves in Equation (2.114) can be written as

$$P^\pm(z, \omega) = \bar{P}^\pm(\omega) \exp(\mp j\omega z/\hat{c}). \quad (2.118)$$

In Equation (2.117), γ has a real and an imaginary part, and can be written as

$$\gamma(\omega) = \gamma_r(\omega) + j\gamma_i(\omega), \quad (2.119)$$

where both γ_r and γ_i are real values. From Equation (2.117), it follows that

$$2\gamma_r\gamma_i = \omega(\rho\Gamma + \kappa K). \quad (2.120)$$

Since the right-hand side of this equation is always non-negative for $\omega > 0$, it follows that γ_r and γ_i have equal sign.

In this thesis, γ_1 will be chosen to be the root with positive real and imaginary parts, and will be denoted as γ . As a consequence, γ_2 will be denoted as $-\gamma$.

After some algebra, an explicit expression for γ_r and γ_i is obtained:

$$\gamma_r = \left[\frac{1}{2} \left(K\Gamma - \omega^2 \rho\kappa + \left\{ (K\Gamma)^2 + \omega^2 \left[(\Gamma\rho)^2 + (K\kappa)^2 \right] + \omega^4 (\rho\kappa)^2 \right\}^{1/2} \right) \right]^{1/2} \quad (2.121)$$

$$\gamma_i = \left[\frac{1}{2} \left(-K\Gamma + \omega^2 \rho\kappa + \left\{ (K\Gamma)^2 + \omega^2 \left[(\Gamma\rho)^2 + (K\kappa)^2 \right] + \omega^4 (\rho\kappa)^2 \right\}^{1/2} \right) \right]^{1/2} \quad (2.122)$$

For high frequencies — when the terms in ω are dominant — Equations (2.121) and (2.122) can be approximated by

$$\gamma_r \simeq \sqrt{\rho\kappa} \frac{\Gamma/\kappa + K/\rho}{2} \quad (2.123)$$

and

$$\gamma_i \simeq \omega \sqrt{\rho\kappa}. \quad (2.124)$$

Consider two points in a homogeneous medium, at different depths z_A and z_B . The pressure at these points due to the presence of a downgoing wave are given by

$$P^+(z_A, \omega) = \bar{P}^+(\omega) \exp(-\gamma z_A) \quad (2.125)$$

and

$$P^+(z_B, \omega) = \bar{P}^+(\omega) \exp(-\gamma z_B). \quad (2.126)$$

It follows that, when the pressure at a given depth z_A is known, the pressure at a different depth z_B can be expressed as

$$P^+(z_B, \omega) = P^+(z_A, \omega) \exp(-\gamma(z_B - z_A)). \quad (2.127)$$

The definition of the propagation factor W — as given by Equation (2.79) — is now generalised to

$$W(\omega, \Delta z) = \exp(-\gamma \Delta z). \quad (2.128)$$

Using this definition, Equation (2.127) becomes

$$P^+(z_B, \omega) = P^+(z_A, \omega) W(\omega, z_B - z_A). \quad (2.129)$$

An analogous derivation for the upgoing wavefield leads to

$$P^-(z_A, \omega) = P^-(z_B, \omega)W(\omega, z_B - z_A). \quad (2.130)$$

Using the separation of Equation (2.119), the propagation factor becomes

$$W(\omega, \Delta z) = \exp(-\gamma_r \Delta z) \exp(-j\gamma_i \Delta z). \quad (2.131)$$

The first factor in the right-hand side of Equation (2.131) is responsible for the attenuation effect during the propagation and is therefore called the attenuation factor — γ_r is called the attenuation coefficient. The second factor determines the phase-behaviour and is called the phase factor.

In the case of an instantaneously reacting medium — which means that both K and Γ are zero — it follows from Equations (2.121) and (2.122) that γ has only an imaginary part, and Equation (2.131) reduces to Equation (2.79).

Specific acoustic impedance

Combining Equations (2.99), (2.114) and (2.118) gives an expression for the vertical velocity component in a plane wave in a medium with relaxation:

$$V(z, \omega) = \bar{V}^+(\omega) \exp(-j\omega z/\hat{c}) + \bar{V}^-(\omega) \exp(j\omega z/\hat{c}), \quad (2.132)$$

with

$$\bar{V}^\pm(z, \omega) = \pm \frac{1}{\hat{\rho}\hat{c}} \bar{P}^\pm(\omega). \quad (2.133)$$

Using the definition of Equation (2.85), it follows that the specific acoustic impedance for a plane wave in a medium with relaxation is given by

$$Z^\pm = \pm \hat{\rho}\hat{c}. \quad (2.134)$$

Using the definitions in Equations (2.97), (2.98) and (2.103), it follows that

$$Z^\pm = \pm \sqrt{\frac{\rho + \frac{1}{j\omega} K}{\kappa + \frac{1}{j\omega} \Gamma}} \quad (2.135)$$

For non-vanishing values of Γ and K , the specific acoustic impedance now has a real and an imaginary part. Theoretical and practical studies concerning the complex specific acoustic impedance can be found in the literature — e.g. Legouis and Nicolas (1987), Paul (1957).

It can be observed that for high frequencies, i.e. $\omega \rightarrow \infty$, the influence of frictional forces and bulk inviscidness on the specific acoustic impedance is less pronounced, and ultimately Equation (2.135) reduces to Equation (2.86).

2.4 Boundary conditions

In the case the constitutive parameters are non-continuous functions of the spatial parameter \mathbf{x} , the wave equations derived in subsections 2.2.2 and 2.3.2 do not longer hold throughout space. At the points where the constitutive parameters do not show a continuous behaviour, boundary conditions have to be introduced.

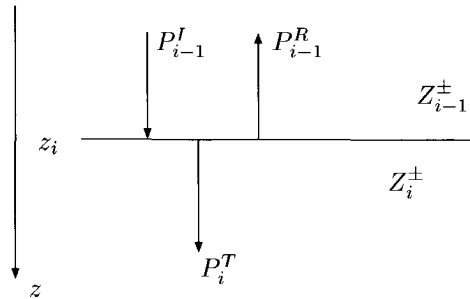


Fig. 2.4 Boundary conditions at the interface z_i between layer $i-1$ with a specific acoustic impedance of Z_{i-1}^\pm and layer i with an acoustic impedance of Z_i^\pm .

In Figure 2.4, the case of a vertically travelling downgoing plane wave encountering an interface — an acoustic impedance contrast — is illustrated. The frequency representation of this wave is denoted by P_{i-1}^I .

Part of the energy of the downgoing wave will be reflected, giving rise to a new upgoing wave P_{i-1}^R , another part P_i^T will be transmitted downwards.

The reflection and transmission coefficients at the boundary between layer $i-1$ and i are given by

$$R_{i-1} = \frac{P_{i-1}^R}{P_{i-1}^I} \quad (2.136)$$

and

$$T_{i-1} = \frac{P_i^T}{P_{i-1}^I}. \quad (2.137)$$

Since the pressure has to be continuous at the interface z_i , it must hold that

$$P_{i-1}^I + P_{i-1}^R = P_i^T, \quad (2.138)$$

leading to the relationship

$$T_{i-1} = 1 + R_{i-1}. \quad (2.139)$$

Also the particle velocity has to be continuous at the interface z_i :

$$V_{i-1}^I + V_{i-1}^R = V_i^T. \quad (2.140)$$

Using the definitions of the specific acoustic impedance — Equation (2.85) — it follows from Equation (2.140) that

$$\frac{P_{i-1}^I}{Z_{i-1}^+} + \frac{P_{i-1}^R}{Z_{i-1}^-} = \frac{P_i^T}{Z_i^+}. \quad (2.141)$$

For simplification, Z^+ will be denoted as Z . It then holds for an instantaneously reacting medium — Equation (2.86) — and a medium with relaxation — Equation (2.135) — that $Z^- = -Z$.

Combining Equations (2.136), (2.137), (2.139) and (2.141) gives an expression for the reflection coefficient R_{i-1} at the interface z_i :

$$R_{i-1} = \frac{Z_i - Z_{i-1}}{Z_i + Z_{i-1}}. \quad (2.142)$$

For an instantaneously reacting medium, the acoustic impedance is real valued see Equation (2.86). As a consequence, also the reflection coefficient is real valued. For a medium with relaxation, however, the acoustic impedance is a complex and frequency-dependent function — see Equation (2.135). It follows that in this case, the reflection coefficient is complex and frequency-dependent too. This complex and frequency-dependent behaviour is less pronounced for high frequencies or low values of K and Γ , as can be observed from Equation (2.135).

2.5 Forward model in a layered configuration

In Sections 2.2 and 2.3, the acoustic wavefield is described for a medium where the constitutive parameters vary as a continuous function of space and time.

In Section 2.4, boundary conditions are given for the wavefield at positions where one or more constitutive parameters show a discontinuity.

A combination of the equations obtained in these previous sections allows to describe the acoustic wavefield in any configuration. In this section, the wavefield in a medium where a laminated material is located, will be studied. The laminated material — also called the target — consists of n parallel layers and is located between two half-spaces.

Inside the layers, the constitutive parameters are assumed to be constant. This allows the use of Equations (2.79) and (2.80) in the case of an instantaneously reacting medium, and Equations (2.129) and (2.131) in the case of a medium with

relaxation. In both cases, if the down- or upgoing wavefield at one position is known, the wavefield at another position is given by

$$P^+(z_B, \omega) = P^+(z_A, \omega)W(\omega, z_B - z_A), \quad (2.143)$$

$$P^-(z_A, \omega) = P^-(z_B, \omega)W(\omega, z_B - z_A). \quad (2.144)$$

The difference between an instantaneously reacting medium and a medium with relaxation is expressed in the propagation factor $W(\omega, \Delta z)$. Apart from the two expressions for the propagation factor that are given in this thesis, also other expressions can be used³ — as long as they describe the wave propagation in a domain where the wavefield quantities vary continuously.

At the interface between the different layers, these equations can not be used, and the reflection and transmission coefficients introduced in the previous section have to be used.

The reflection coefficient between two instantaneously reacting media is calculated in a different way than in the case one or both layers at the interface show relaxation phenomena. The expression for the reflection coefficient — Equation (2.142) — holds for both cases, however. The difference between instantaneously reacting media and media with relaxation is expressed in the definition of their specific acoustic impedance — Equation (2.135) and (2.86).

In addition to the geometrical configuration and the acoustic properties of the different layers, the location and characteristics of possible sources need to be known, in order to calculate the wavefield.

In the configuration shown in Figure 2.5, a source is located in the upper half-space, at depth z_0 . This source emits a plane wave propagating perpendicular to the interfaces orientation and then the above-mentioned equations can be used.

The goal of this section is to derive a representation for the wavefield at the same position as the location of the source. The measured wavefield will be dependent on the used source and on the acoustic parameters of the material the waves interact with.

When a wave is sent downward into a material, a resulting upgoing wavefield will occur at the transducer, which is also located in the upper half-space. Since this wavefield exists due to scattering of energy in the material, this resulting wavefield is also called the scattered wavefield. The total wavefield at the transducer thus consists of a source wavefield emitted by the transducer — also called the downgoing wavefield since the energy travels downwards from the transducer into the investigated medium — and a scattered wavefield — also called the upgoing wavefield since

³For example, a better understanding of friction can lead to another formulation of Equation (2.87), resulting in another expression for $W(\omega, \Delta z)$.

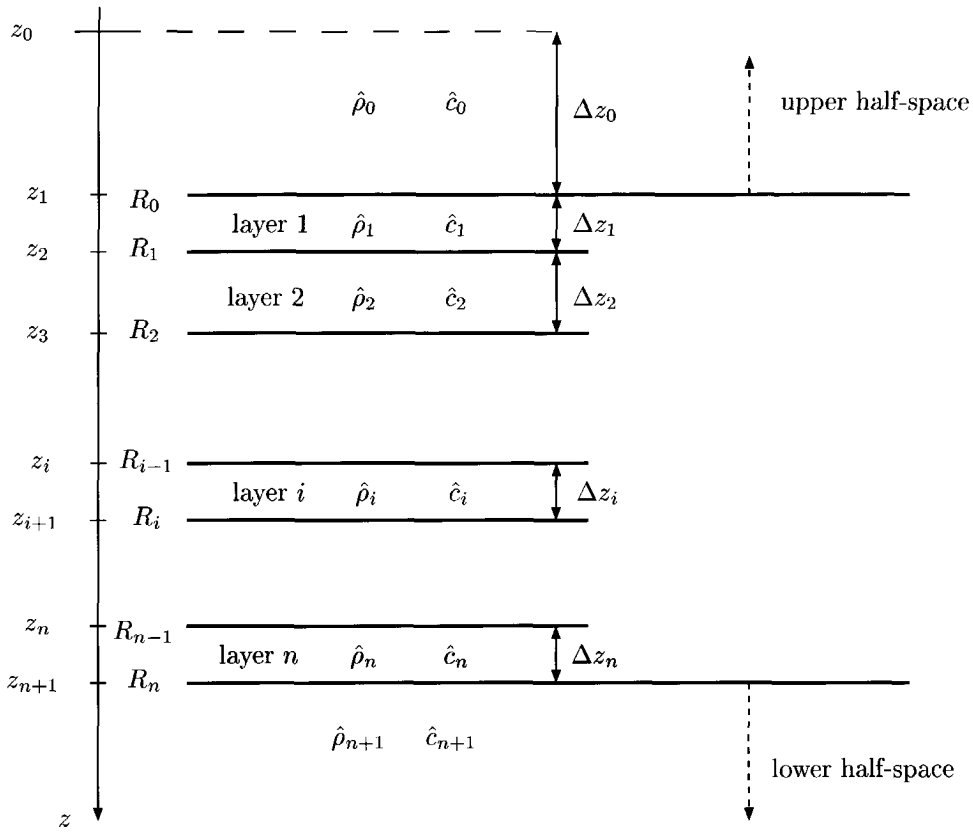


Fig. 2.5 Configuration and naming conventions for a laminated target. The different layers are characterised by their thickness Δz , generalised density $\hat{\rho}$ and generalised acoustic velocity \hat{c} . Note that in the case the medium in the layer is instantaneously reacting, $\hat{\rho}$ and \hat{c} reduce to respectively ρ and c .

the energy travels upwards from the medium towards the transducer.

A recursive procedure will be applied in order to obtain the scattered wavefield at the transducer. Such a recursive formulation for the one dimensional model has been given by a.o. Kennett (1974). A recursion algorithm consists of two parts:

- an initiation step;
- a number of recursion steps.

2.5.1 Initiation step

In the first step, only the bottom layer n of the target is considered, and this layer is assumed to be unbounded at the top — as a consequence, it is a half-space. A — virtual — source is positioned at z_n , and the scattered wavefield at the same position is calculated.

The configuration is shown in Figure 2.6.

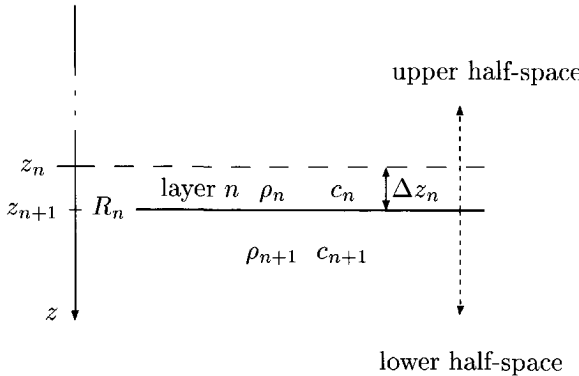


Fig. 2.6 Configuration in the initiation step for the recursion algorithm. The interface-free transfer function at z_n will be calculated.

According to Equation (2.143), the downgoing wavefield just above interface z_{n+1} is in the frequency domain given by

$$P^+(z_{n+1}, \omega) = W(\omega, \Delta z_n) P^+(z_n, \omega), \quad (2.145)$$

where $P^+(z_n, \omega)$ is the frequency-representation of the downgoing wavefield emitted by the virtual source at z_n .

As explained in Section 2.4, part of the energy in the downgoing wavefield will be transmitted in the lower half-space — as a consequence, this part will never appear at the transducer —, while another part will be reflected back into layer n . The reflected energy gives rise to an upgoing wavefield $P^-(z_{n+1}, \omega)$, which is given by

$$P^-(z_{n+1}, \omega) = R_n W(\omega, \Delta z_n) P^+(z_n, \omega). \quad (2.146)$$

This upgoing wavefield propagates through layer n . Using Equation (2.144) leads to the upgoing wavefield at the interface z_n :

$$P^-(z_n, \omega) = W(\omega, \Delta z_n) R_n W(\omega, \Delta z_n) P^+(z_n, \omega). \quad (2.147)$$

The transfer function of a system is defined as the response of the system when a single pulse in the time-domain is used as the source function. This source function

is in the frequency domain denoted by $S_X(\omega)$ and is defined as

$$S_X(\omega) = 1. \quad (2.148)$$

In this case, the frequency content of the downgoing wavefield at the interface z_n is given by

$$P^+(z_n, \omega) = S_X(\omega) = 1. \quad (2.149)$$

The transfer function of the considered configuration is then given by

$$X_n^0(\omega) = W(\omega, \Delta z_n) R_n W(\omega, \Delta z_n). \quad (2.150)$$

The superscript 0 is used to indicate that no interface is assumed on top of the material – thus preventing that upgoing energy will be reflected back into the configuration. Therefore, X_n^0 will also be called the interface-free transfer function at z_n .

2.5.2 Recursion steps

The goal of one recursion step is to obtain the interface-free transfer function X_{i-1}^0 provided that X_i^0 is known. Each recursion steps consist of two parts: in the first part, an interface is put in the top-most layer at depth z_i and the material parameters of layer $i-1$ are assigned to the new top half-space. In the second part, the interface-free transfer function is calculated at z_{i-1} . Ultimately, the interface-free transfer function at z_0 is obtained.

After $n-i$ recursive steps, the configuration looks like Figure 2.7(a). The upper half-space has the material properties of layer i , and the interface-free transfer function X_i^0 is known.

addition of interface i

In this step, it is assumed that layer i is bounded at the top side and the half-space on top on it has the properties of layer $i-1$.

In this case, a part $-R_{i-1}$ of the upgoing wavefield $P^-(z_i, \omega)$ just below z_i will be reflected back, due to the impedance contrast between layer i and layer $i-1$. The resulting downgoing wavefield is thus $P_i^+ - R_{i-1} P_i^-$. It follows that the total upgoing wavefield at z_i is implicitly written as

$$P_i^- = X_i^0 (P_i^+ - R_{i-1} P_i^-). \quad (2.151)$$

The total transfer function X_i at depth z_i is implicitly defined as

$$P_i^- = X_i P_i^+. \quad (2.152)$$

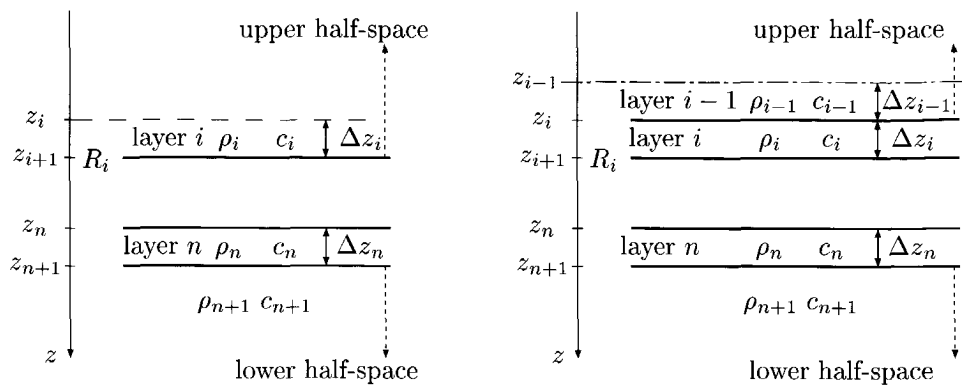
(a) Configuration after $n - i$ steps, before the addition of interface i (b) Configuration in i th step, extrapolation towards z_{i-1}

Fig. 2.7 Configuration after $n - i$ recursion steps, before and after the addition of interface z_i and extrapolation towards z_{i-1} .

It follows from Equation (2.151) that

$$X_i = X_i^0 (1 - R_{i-1} X_i), \quad (2.153)$$

from which an explicit form of the transfer function can be obtained:

$$X_i = \frac{X_i^0}{1 + R_{i-1} X_i^0}. \quad (2.154)$$

A scheme of this is shown in Figure 2.8.

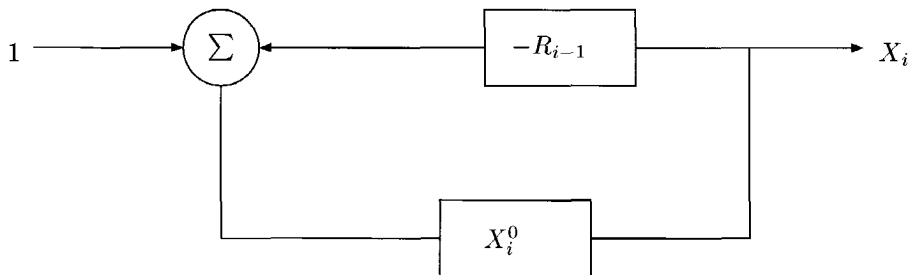


Fig. 2.8 Stream diagram for the calculation of the transfer function X_i .

extrapolation towards z_{i-1}

In the second step, the virtual source is moved from z_i — just below interface i — towards z_{i-1} . The total transfer function for the case where source and receiver are located at z_i is obtained in the previous step and given by X_i . The wavefield at z_{i-1} for this configuration consists of two contributions: a directly reflected contribution, and a transmitted contribution through interface i .

According to Equation (2.143), the downgoing wavefield at z_i is given by

$$P^+(z_i, \omega) = W(\omega, \Delta z_{i-1}) P^+(z_{i-1}, \omega). \quad (2.155)$$

Due to the impedance contrast between layer $i-1$ and layer i , a part R_{i-1} of the energy in the downgoing wavefield $P^+(z_i, \omega)$ will be reflected. This part will give a contribution $W(\omega, \Delta z_{i-1}) R_{i-1} W(\omega, \Delta z_{i-1}) P^+(z_{i-1}, \omega)$ at z_{i-1} . Another part of this downgoing wavefield, given by $(1 + R_{i-1}) W(\omega, \Delta z_{i-1}) P^+(z_{i-1}, \omega)$ is transmitted into layer i , where it acts as a source for the configuration in the previous step. As a consequence, the upgoing wavefield at z_i is given by $X_i (1 + R_{i-1}) W(\omega, \Delta z_{i-1}) P^+(z_{i-1}, \omega)$. A part $1 - R_{i-1}$ of this wavefield is transmitted into layer i and will propagate to z_{i-1} .

The total upgoing wavefield at z_{i-1} can thus be written as

$$P^-(z_{i-1}, \omega) = W_{i-1} (R_{i-1} + (1 - R_{i-1}^2) X_i) W_{i-1} P^+(z_{i-1}, \omega), \quad (2.156)$$

where W_{i-1} is a short notation for $W(\omega, \Delta z_{i-1})$.

This procedure is shown in Figure 2.9. It follows that the interface free transfer

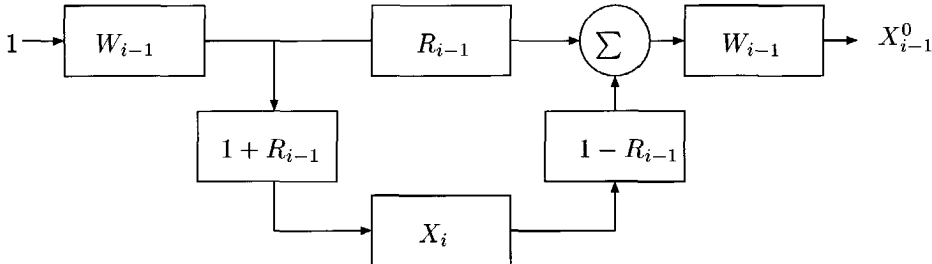


Fig. 2.9 Schematic calculation of the extrapolation step in the recursion algorithm.

function at z_{i-1} can be written as

$$X_{i-1}^0 = W_{i-1} (R_{i-1} + (1 - R_{i-1}^2) X_i) W_{i-1}. \quad (2.157)$$

overview of the recursion steps

The iterative algorithm that calculates the total response of a horizontal layered medium can thus be initiated by

$$X_n^0 = W_n R_n W_n. \quad (2.158)$$

The iteration steps are defined by

$$X_i = \frac{X_i^0}{1 + R_{i-1} X_i^0}, \quad (2.159)$$

$$X_{i-1}^0 = W_{i-1} (R_{i-1} + (1 - R_{i-1}^2) X_i) W_{i-1}. \quad (2.160)$$

The derived equations calculate the impulse response for a given configuration. When the source is not a delta-pulse, but an actual wavelet with a time-representation $s(t)$ and a frequency content $S(\omega)$, the scattered pressure is the time-convolution of the response function with the source signal. In practice only the scattered pressure is recorded. Therefore P_i will be used in the remainder of this thesis to indicate the scattered pressure P_i^- . Also P_i^0 will be used to indicate interface-free scattered pressure at depth z_i .

In the frequency domain, the scattered pressure is given by

$$P_i^0 = X_i^0 S, \quad (2.161)$$

$$P_i = X_i S. \quad (2.162)$$

By combining Equations (2.158), (2.159), (2.160), (2.162) and (2.162), an iterative procedure for calculating the scattered pressure at a transducer located at the top of the material can be obtained. The algorithm is initiated by

$$P_n^0 = W_n R_n W_n S. \quad (2.163)$$

The iteration steps are given by

$$P_i = \frac{P_i^0 S}{S + R_{i-1} P_i^0}, \quad (2.164)$$

$$P_{i-1}^0 = W_{i-1} (R_{i-1} S + (1 - R_{i-1}^2) P_i) W_{i-1}. \quad (2.165)$$

P_i^0 is often called the interface-multiple free pressure at the top of layer i , since this pressure is obtained assuming that layer i has no surface – it is unbounded at its top. As a consequence, there are no multiples⁴ related to the top of this layer in the expression. Note however that multiples due to reflections in layers $i + 1$ till n are present in the expression.

⁴Following the seismic terminology, the term "multiples" refers to waves that propagate in the target (downward and upward) and have bounced at least twice before detection. A description and classification of multiples can be found in Verschuur (1991).

2.6 Simulations

The theory developed in the previous sections can be used to predict the acoustic transfer function of a laminated material — by means of Equations (2.158), (2.159) and (2.160). For a given source distribution $S(\omega)$, Equations (2.163), (2.164) and (2.165) can be used to predict the resulting pressure.

One reason for performing simulations, is to check the validity of the developed theory. A good match between simulated results and measurements is an indication for the quality of the theory — although even an incorrect theory can give correct results.

In Chapter 3, the results of real measurements will be shown. In order to compare these measurements with the theoretical predictions, it is important that the source signal used in the measurements is also used in the simulations.

The source signal will be studied in Section 3.4. For convenience, the most frequently used source signal is already shown in Figure 2.10⁵. This source signal will be used in the following simulations.

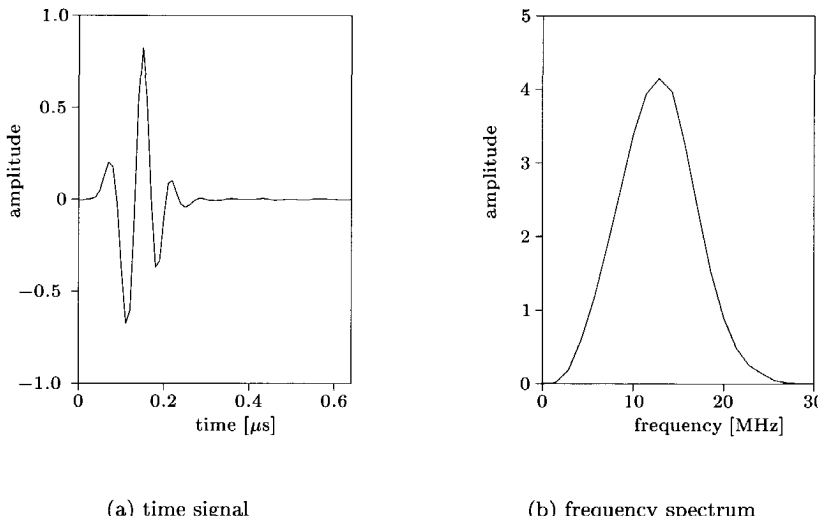


Fig. 2.10 Source signal obtained with a transducer with a centre frequency at 15 MHz, focussed at 76.2mm. The signal is obtained after a reflection on a glass beam located in the focus zone.

⁵It should be noted here that in the following simulations, the source signal is scaled so that its maximum value is 1.

2.6.1 Aluminium layer

In this subsection, the target material is a homogeneous aluminium disk. The lateral dimensions are large compared with the thickness. The material is assumed to be instantaneously reacting. As a consequence Equation (2.79) can be used to calculate the propagation factor W .

The material properties of the constituting layers are given in Table 2.1. The thickness of the water layer is chosen to be 76 mm, since in this case the target is located in the focus zone of the used transducer⁶.

Aluminium disk in water				
Layer	material	Δz (mm)	ρ (kg/m ³)	c (m/s)
0	water	76	1000	1480
1	aluminium	.5	2740	6300
2	water	∞	1000	1480

Table 2.1 Material properties for an aluminium disk embedded in water.

Using the conventions illustrated in Figure 2.5, the configuration and the definitions of the parameters are shown in Figure 2.11.

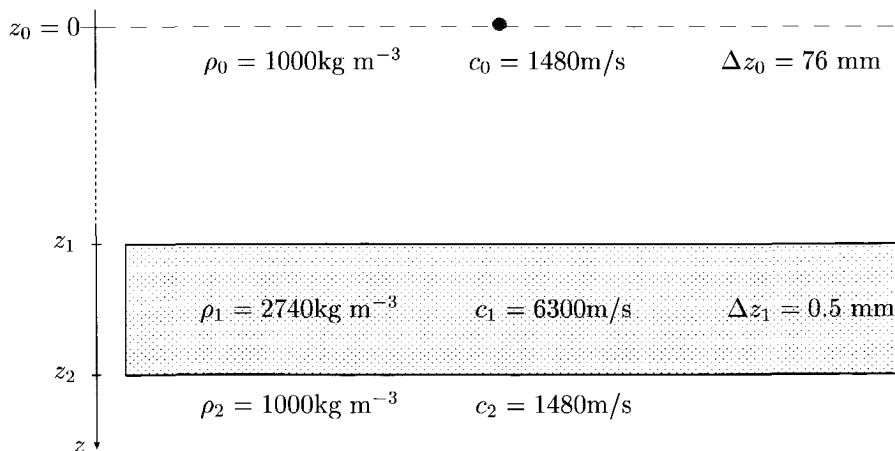


Fig. 2.11 Configuration for a reflection measurement on an aluminium layer embedded in water.

Based on these parameters, the reflection coefficients R_0 and R_1 and the travel times

⁶The term *focus zone* is explained in the next chapter, and it will be shown that the best results are obtained when the target is placed in the focus zone of the used transducer.

t_0 and t_1 — needed for the calculation of the propagation factor — can be calculated. Using the theory described in the previous sections, the scattered pressure $P_0(\omega)$ — in the frequency domain — and its time counterpart $p_0(t)$ is calculated. The result is shown in Figure 2.12. Since the distance between the transducer and the material is large compared with the thickness of the target, only a small part of the response time-signal is of interest.

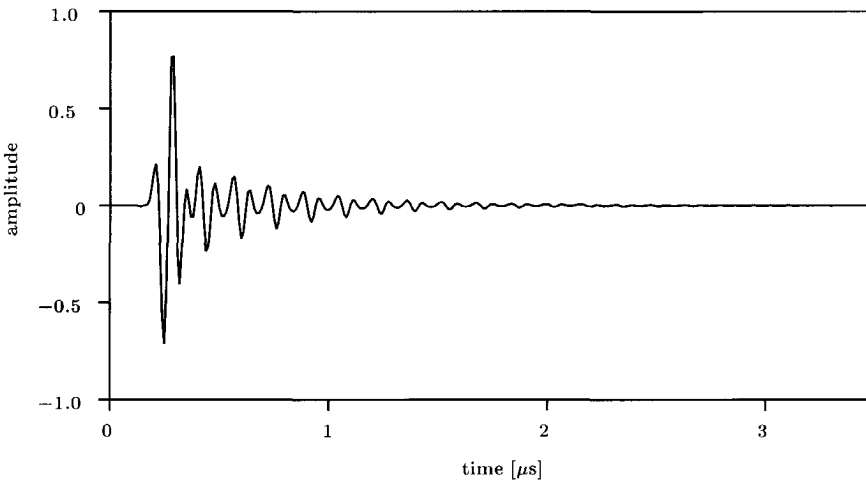


Fig. 2.12 Simulated reflection measurement on an aluminium layer embedded in water. The geometrical configuration is shown in Figure 2.11 and the material parameters are given in Table 2.1.

Although they are not completely separated from each other, the different arrivals due to primary reflections — at the top and the bottom of the aluminium disk — and multiple reflections can easily be distinguished in Figure 2.12.

In Figure 2.13, the influence of the layer thickness on the resulting scattered wavefield is shown. It is clear that the thinner the layer, the more difficult it becomes to separate the different arrivals from each other without using any processing tools.

2.6.2 Prepreg

The high impedance contrast between water and aluminium has some consequences for the amplitude of the different arrivals:

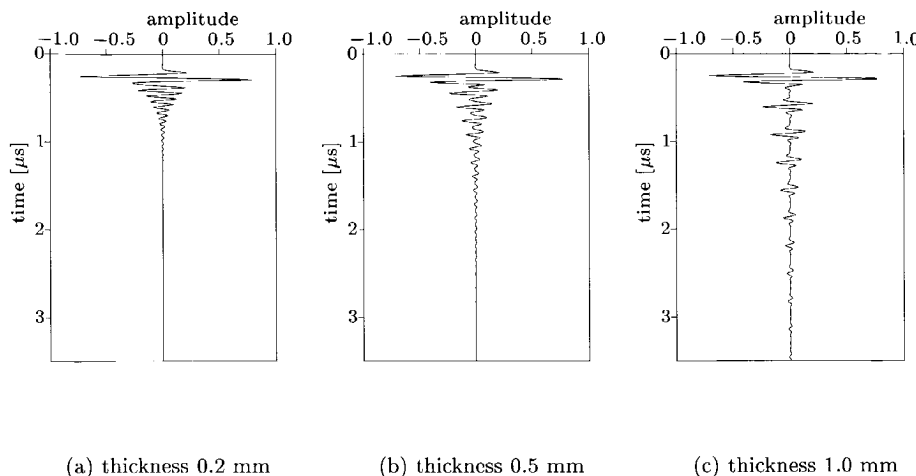


Fig. 2.13 Simulated reflection response of an aluminium layer with a variable thickness. Note the influence of the thickness of the aluminium layer on the ability to distinguish the different arrivals.

1. the first arrival — due to a reflection at the top of the layer — has a high amplitude;
2. as a consequence of the low transmission from water into aluminium, the second arrival — due to a reflection at the bottom of the layer — has a low amplitude;
3. the multiples have relatively high amplitudes, and the amplitude decreases slowly with the order of the multiple due to the two strong reflections on either interface of the aluminium layer.

The above mentioned effects will be less pronounced for the reflection measurement on a prepreg layer due to the lower impedance contrast between water and prepreg. Furthermore, it is expected that acoustic losses in the epoxy-fibre prepreg layers occur due to frictional forces and bulk viscosity. As a consequence, the theory of Section 2.3 has to be used, and two extra parameters — the coefficient of frictional force K and the coefficient of bulk inviscidness Γ — have to be taken into account. These coefficients will influence both the propagation and the reflection of the acoustic waves.

propagation effects

By comparing the propagation factor for an instantaneously reacting fluid — Equation (2.79) — with the propagation factor for a medium with relaxation — Equa-

tion (2.128) —, it follows that the extra factor for dealing with the attenuation effects is in the high-frequency approach given by $\exp(-\gamma_r \Delta z)$. It follows from Equation (2.123) that this factor is dependent on both K and Γ .

At this point, the influence of the attenuation coefficient γ_r will be examined. The values of Γ and K will be chosen such that they give an equal contribution in γ :

$$\frac{\sqrt{\rho\kappa} \Gamma}{2 \kappa} = \frac{\gamma_r}{2} \quad (2.166)$$

and

$$\frac{\sqrt{\rho\kappa} K}{2 \rho} = \frac{\gamma_r}{2}. \quad (2.167)$$

The acoustic response of a prepreg layer with a thickness of 0.25 mm will be calculated. Three different attenuation coefficients will be used, and the results will be compared with measurements in the next chapter. The geometrical configuration is shown in Figure 2.14 and the material parameters are given in Table 2.2.

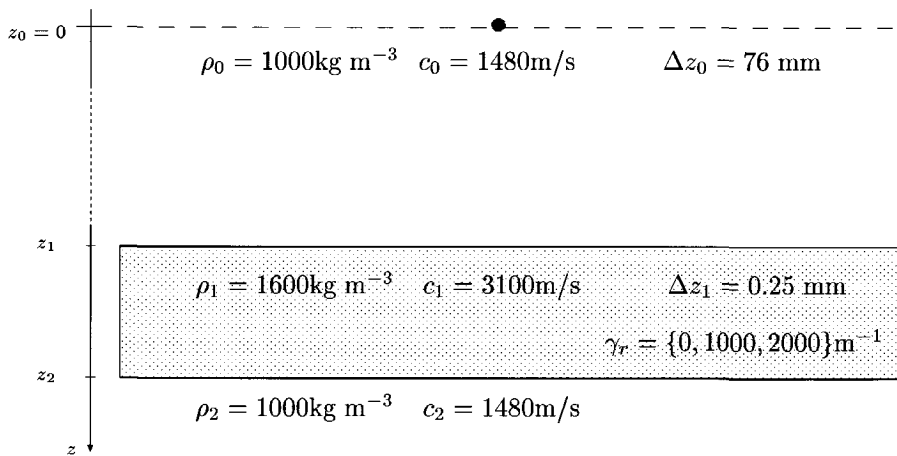


Fig. 2.14 Configuration for a reflection measurement on a prepreg layer embedded in water.

The acoustic responses on the source signal shown in Figure 2.10 for the different configurations are shown in Figure 2.15.

As expected, a stronger attenuation coefficient results in a decrease of acoustic energy⁷ — and thus a decrease of the measured signal amplitude. The more often a

⁷It was shown in subsection 2.3.1 that part of the acoustic energy is dissipated.

Prepreg layer in water					
Layer	material	Δz (mm)	ρ ($\frac{\text{kg}}{\text{m}^3}$)	c ($\frac{\text{m}}{\text{s}}$)	γ_r (1/m)
0	water	76	1000	1480	0
1	prepreg	.25	1600	3100	{ 0, 1000, 2000 }
2	water	∞	1000	1480	0

Table 2.2 Material properties for a prepreg layer embedded in water.

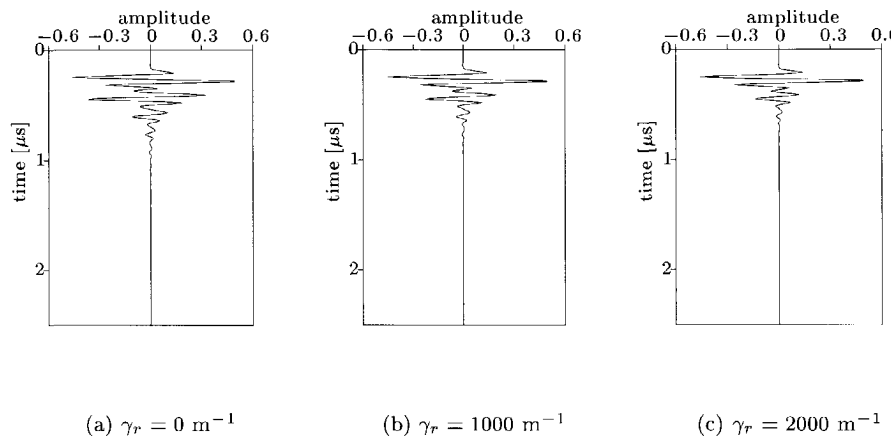


Fig. 2.15 Simulated acoustic response for a prepreg layer with different attenuation coefficients. It can be observed that the higher the attenuation coefficient, the less acoustic energy is present in the signal.

wave travels through a layer with a high attenuation coefficient, the more the resulting arrival will be attenuated.

reflection effects

The reflection coefficients are, by means of Equation (2.142), dependent on the acoustic impedances of the layers. For a medium with relaxation, the acoustic impedance is given by Equation (2.135). It has been shown in Section 2.4 that for high frequencies, the influence of both K and Γ on the reflection coefficient is minimal. This will be illustrated here with a numerical example.

At this point, γ_r in layer 1 will be held constant at 1000 m^{-1} . By varying Γ and K , the reflection coefficient will change, but the propagation factor remains unchanged. When the attenuation is completely due to frictional forces, it holds that

$$\gamma_r = \frac{\sqrt{\rho\kappa}}{2} \frac{\Gamma}{\kappa} \quad (2.168)$$

$$K = 0. \quad (2.169)$$

In the case the attenuation is completely due to viscosity, it holds that

$$\gamma_r = \frac{\sqrt{\rho\kappa}}{2} \frac{K}{\rho} \quad (2.170)$$

$$\Gamma = 0. \quad (2.171)$$

Three different configurations will be examined now: the extreme cases where the attenuation is completely due to one of the two phenomena, and an intermediate case. The configurations are given in Table 2.3. The acoustic responses on the

Prepreg layer in water			
Layer	material	Γ (ms/kg)	$K(\text{kg m}^{-3}\text{s}^{-1})$
0	water	0	0
1	prepreg	$\{ 0, 2.02 \cdot 10^{-4}, 4.03 \cdot 10^{-4} \}$	$\{ 9, 92 \cdot 10^9, 4.96 \cdot 10^9, 0 \}$
2	water	0	0

Table 2.3 Material properties for a prepreg layer embedded in water for ρ and c given in Table 2.2. The attenuation coefficient γ_r is kept constant

source signal shown in Figure 2.10 for the different prepreg-configurations is shown in Figure 2.16.

The three configurations give very similar acoustic responses, which is in agreement with the analysis of Equation (2.142). Therefore, it is reasonable to neglect the extra effects due to attenuation in reflection in the considered situations⁸. This is illustrated in Figure 2.17, where a simulation incorporating the attenuation effects in reflection is compared with a simulation where these effects are neglected. As a consequence, the effect of attenuation due to frictional forces or bulk inviscidness, whether it is due to one or both of these phenomena, can be described by one parameter, the attenuation coefficient γ_r .

The attenuation coefficient γ_r , which is used here using the high-frequency approximation of Equation (2.121) is only dependent on the material properties K , Γ , ρ and κ — and not on the used frequency. As a consequence, γ_r is a material parameter too, and once the value of γ_r for a particular material is known, it can be used in any simulation for a configuration where the considered material is part of.

⁸Neglecting these effects means that the specific acoustic impedance of the considered layer is calculated using Equation (2.86) instead of using Equation (2.135).

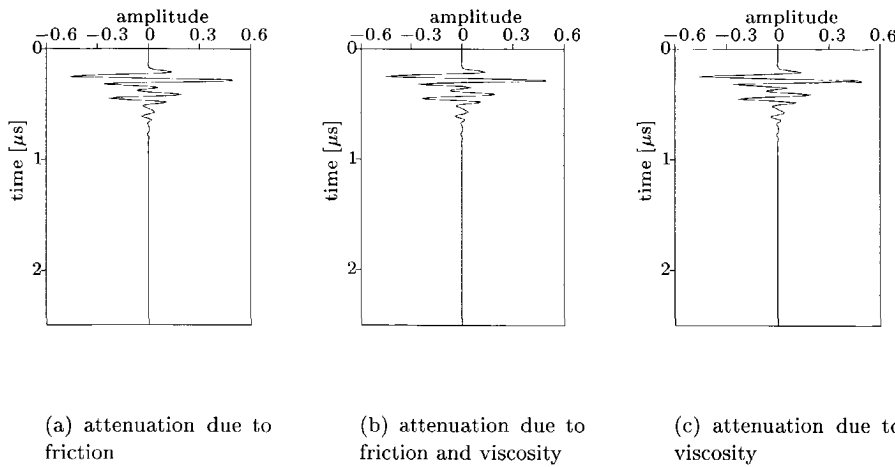


Fig. 2.16 Simulated acoustic response for a prepreg layer. The attenuation coefficient is 1000 m^{-1} for the three cases. The values of Γ and K are given in Table 2.3.

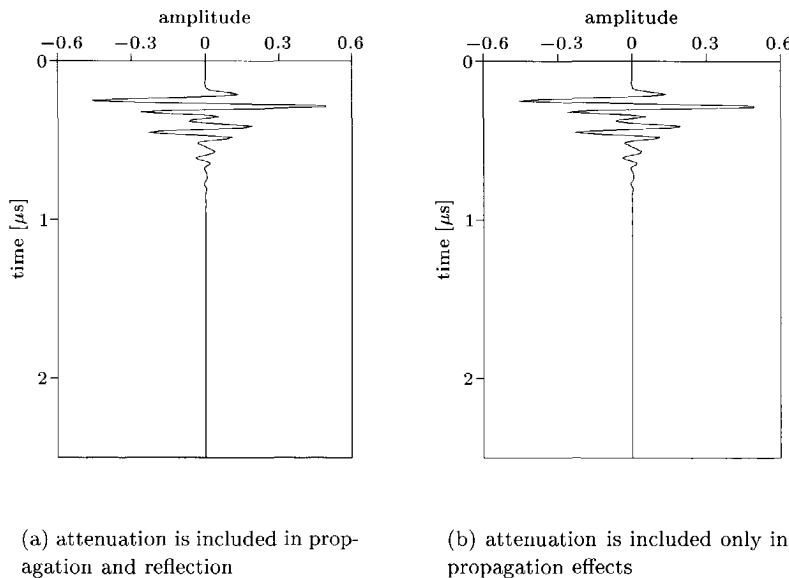


Fig. 2.17 Simulated acoustic response for a prepreg layer with $\Gamma = 2.02 \cdot 10^{-4} \text{ m s kg}^{-1}$ and $K = 4.96 \cdot 10^9 \text{ kg m}^{-3} \text{ s}^{-1}$, leading to $\gamma_r = 1000 \text{ m}^{-1}$. A comparison of the two figures shows that the extra effects due to attenuation in reflection can be neglected.

2.6.3 Glare

Until now, the target material exists of only one layer. Laminated materials consist of more constituting layers, however. In this subsection, the target material is a glare laminate. The glare naming convention is explained in Appendix A.

Glare 2/1

As a first case, a glare 2/1 laminate is considered. The model is shown in Figure 2.18.

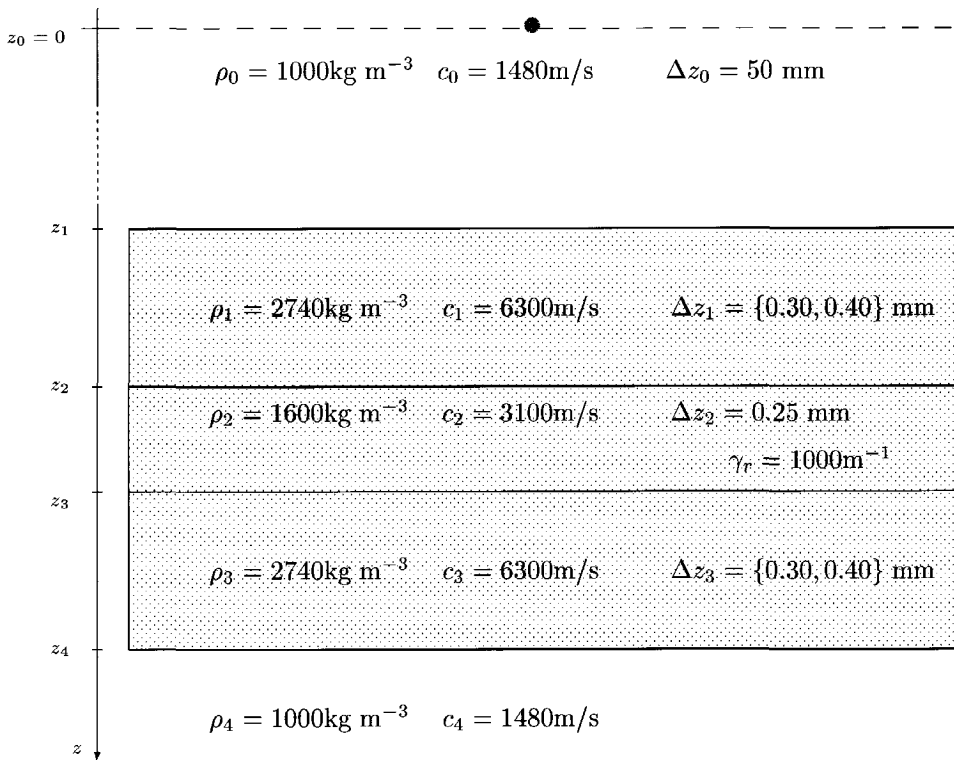


Fig. 2.18 Configuration for a reflection measurement on a glare 2/1 material embedded in water.

Two different configurations $\{a, b\}$ will be simulated: a first one with aluminium layers with a thickness of 0.3 mm and a second one with the thickness of the aluminium layers equal to 0.4 mm. The properties of the configuration are given in Table 2.4.

The aluminium layers are assumed to be instantaneously reacting. As a consequence, no attenuation factor is needed and Equation (2.79) can be used for the calculation

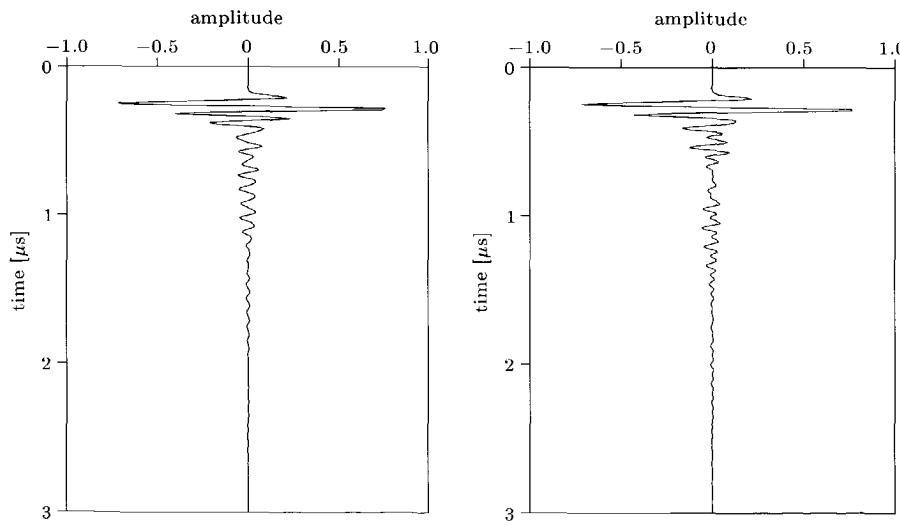
Glare 2/1 $\{a, b\}$ target in water					
Layer	material	Δz (mm)	ρ (kg/m ³)	c (m/s)	γ_r (1/m)
0	water	76	1000	1480	0
1	aluminium	{0.3,0.4}	2740	6300	0
2	prepreg	0.250	1600	3100	1000
3	aluminium	{0.3,0.4}	2740	6300	0
4	water	∞	1000	1480	0

Table 2.4 Material properties for a Glare 2/1 material embedded in water.

of the propagation factor in these layers.

As stated in the previous subsection, it is assumed that acoustic losses may occur in the prepreg layer. As a consequence, Equation (2.128) has to be used for the calculation of the propagation factor in the prepreg layer.

The acoustic response of these configurations on the source signal shown in Figure 2.10 is given in Figure 2.19.



(a) Configuration a, the thickness of the aluminium layer is 0.3 mm

(b) Configuration b, the thickness of the aluminium layer is 0.4 mm

Fig. 2.19 Acoustic response for two glare 2/1 configurations.

It can be seen that even for this relatively simple configuration — with only three

constituting layers — the acoustic response can look rather complex. Since primary reflections interfere with multiple reflections, it is impossible to reveal the positions of the primary reflections without doing some processing.

Glare 3/2

In this example, it will be shown how the response of a more complex configuration is built up using the recursive algorithm. A Glare 3/2 material is considered and the acoustic parameters of this configuration are given in Table 2.5. The same source-

Glare 3/2 target in water					
Layer	material	Δz (mm)	ρ (kg/m ³)	c (m/s)	γ_r (1/m)
0	water	76	1000	1480	0
1	aluminium	0.3	2740	6300	0
2	prepreg	0.250	1600	3100	1000
3	aluminium	0.3	2740	6300	0
4	prepreg	0.250	1600	3100	1000
5	aluminium	0.3	2740	6300	0
6	water	∞	1000	1480	0

Table 2.5 Material properties for a Glare 3/2 material embedded in water.

signal as in the previous subsection is used to calculate the response. Figure 2.20 shows how the recursive equations are used to build the total scattered wavefield by recursively adding one layer, starting from the bottom layer. In Figure 2.20(a), the interface free wavefield of a virtual configuration, consisting only of layers 5 and 6 is shown. In each of the next figures, one layer is added to the virtual configuration, and the interface free wavefield is calculated. Ultimately, Figure 2.20(f) shows the acoustic response of the complete configuration — the Glare 3/2 material.

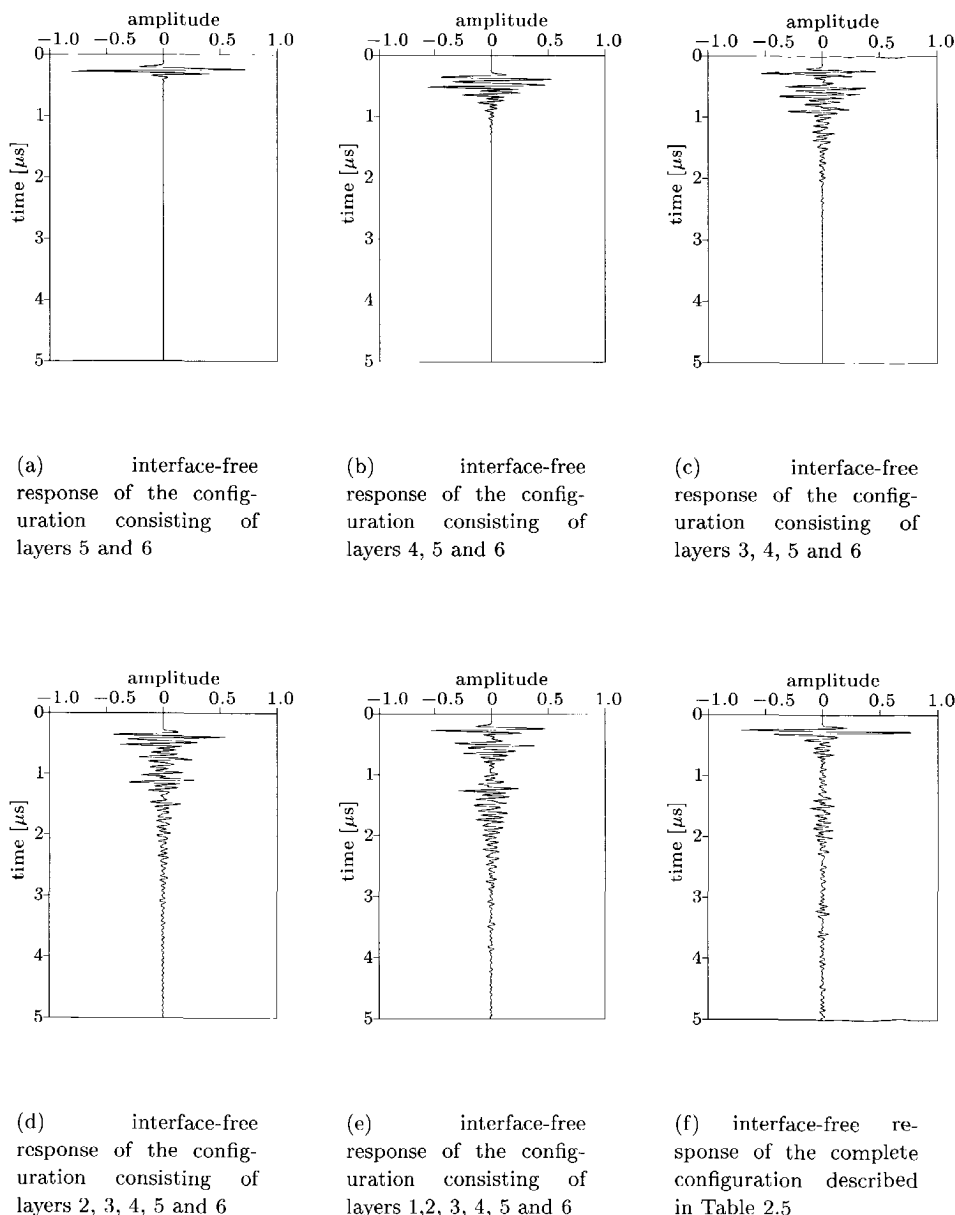


Fig. 2.20 Initial, intermediate and final results of the forward recursive algorithm applied to a Glare 3/2 configuration. In Figure (a), only the bottom most layer is taken into account. In the next figures, one layer is added each time.

Glare 3/2 with void inclusions

In this last example, the influence of void inclusions on the scattered pressure is examined. A Glare 3/2 disk is scanned at 100 positions on one line, the space between the scan positions amounts 0.5mm. Although this is a two-dimensional configuration, the results are obtained by performing 100 one-dimensional simulations. The configuration is given in Figure 2.21.

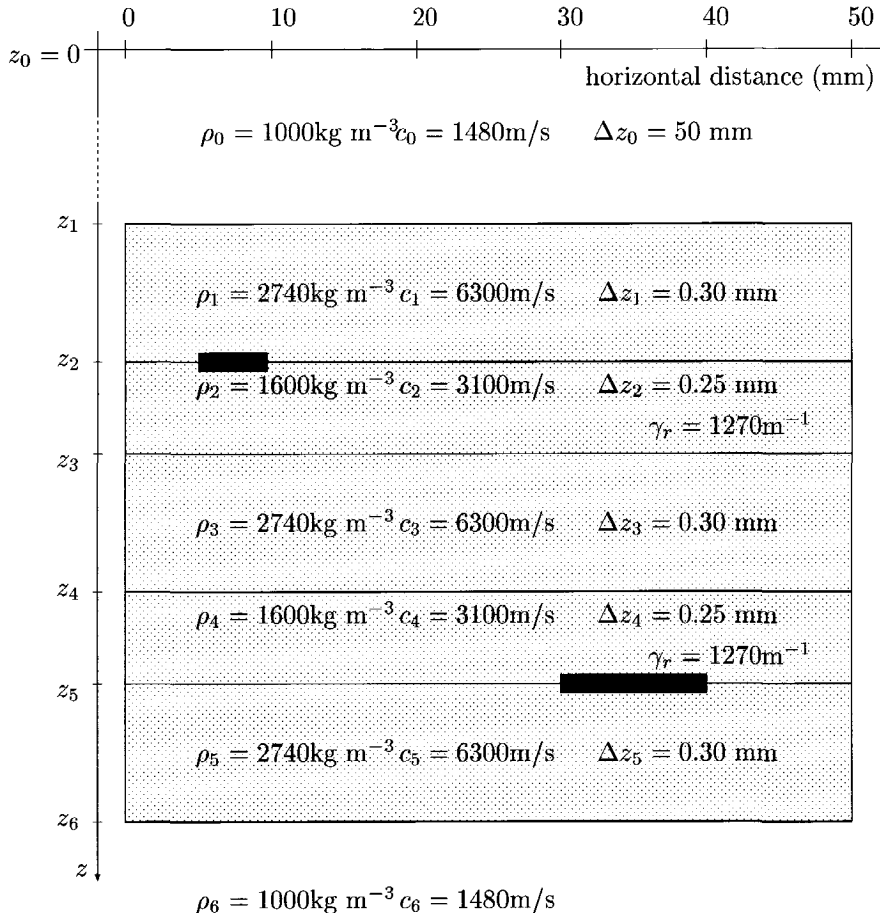


Fig. 2.21 Configuration for reflection measurements on a glare 3/2 material embedded in water. Void inclusions are indicated with dark spots.

In this figure, two void inclusions⁹ are indicated with a dark spot. The results of

⁹Throughout this thesis, the term void inclusion refers to a volume with a small thickness, that is either vacuum or filled with air.

three scans are compared with each other in Figure 2.22:

- the first one is taken at a horizontal distance of 3 mm — in the intact region,
- the second one is taken at a horizontal offset of 7 mm — at the location of the first void inclusion, which is situated between layer 1 and layer 2,
- the third one is taken at a horizontal offset of 35 mm — at the location of the second void inclusion, which is situated between layer 4 and layer 5.

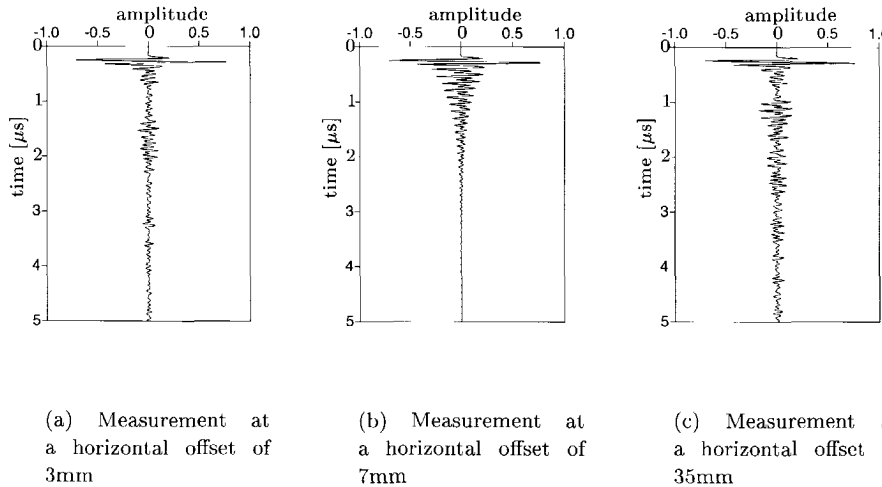


Fig. 2.22 Simulated acoustic response for a Glare 3/2 layer, comparison between positions with and without delaminations. It can be seen that the presence and position of delaminations influence the acoustic response of the material.

It can be clearly seen that the presence and the position of possible void inclusions alters the scattered pressure. The results of the 100 successive scans are shown in one plot in Figure 2.23. In this grey level plot, the scattered pressure is shown as a function of time and horizontal distance. Positive values are shown in dark, low (i.e. negative) values have light colours.

In Chapter 4 and Chapter 5, two inversion techniques will be explained for retrieving information about void inclusions from the scattered wavefield.

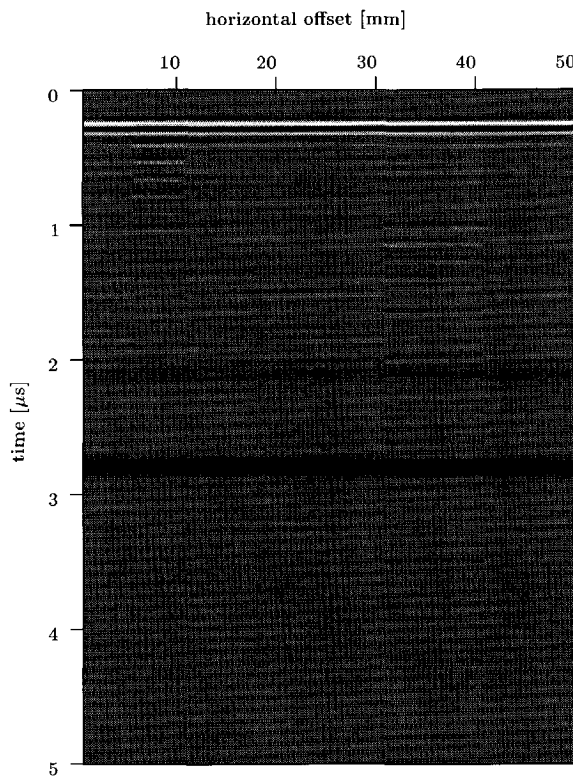


Fig. 2.23 Grey level plot of 100 successive measurements on a Glare 3/2 disk. The distance between two scan points is 0.5 mm, and the configuration is shown in Figure 2.21.

Chapter 3

Measurements

In order to check the validity of a theory, it is useful that the results predicted by the theory are confirmed by actual measurements. Although the assumptions in the previous chapter are rather fair, they are not completely satisfied in all practical cases.

Also, computers that are used for digital data processing are not designed to work with acoustic pressures or velocities. Therefore, the acoustic wavefield has to be converted into a series of digital numbers — the numerical wavefield representation. This conversion might introduce even more errors to the resulting wavefield representation in the computer.

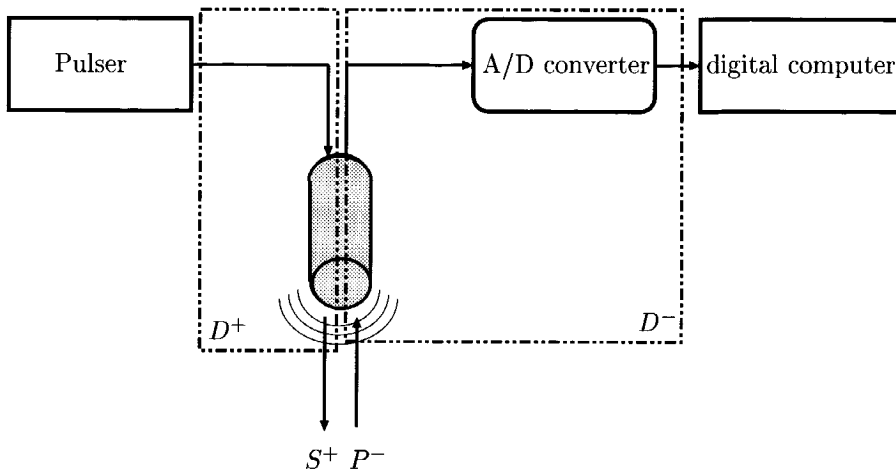
In this chapter, the generation of an actually recorded wavefield and the conversion of this wavefield — the acoustic pressure or velocity — to the numerical wavefield representation — a series of numbers — will be discussed. Next, the numerical results of actual measurements will be shown and compared with the results predicted by the theory described in the previous chapter.

3.1 Conversion of the acoustic pressures

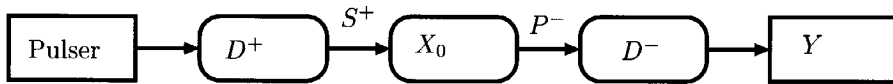
The acoustic wavefield evaluated at a point can be described by the particle velocity as well as the acoustic pressure in the considered point. In the simulations in Chapter 2, the acoustic pressure of the wavefield is calculated. Therefore, it is reasonable to restrict the analysis here to acoustic pressures.

The acoustic transducers used in the following experiments convert an electric signal into an acoustic wavefield and vice versa. Since a source wavefield is needed in order to measure the response of the target on an acoustic excitation, an electric signal has to be supplied to the transducer. The source wavefield will interact with the target as described in the previous chapter. The resulting wavefield at the transducer is

then converted into an electric signal, and this signal will be converted into a series of numbers. A schematic overview of these conversions is given in Figure 3.1(a).



(a) Practical setup for performing measurements



(b) Transfer function from an electric pulser to a digital computer

Fig. 3.1 Signal flow of the complete measurement process. The conversions are illustrated. The symbols used in this figures are explained throughout the text.

The transfer function X_0 as given in the forward algorithm of the previous chapter — see Equation (2.152) — only describes the transfer from the downgoing pressure S^+ generated by the acoustic source towards the upgoing scattered acoustic pressure P^- . This transfer function can now be extended as in Figure 3.1(b). In this figure, D^+ is the operator that converts the electric pulse into a downgoing acoustic source wavefield, while D^- is the operator that converts the upgoing acoustic pressure into a digital representation Y in the computer.

The transducer that generates the wavefield may or may not be the same transducer that measures the wavefield. For the measurements described in this chapter, the same transducer is used for generating and registering the wavefield. In the next sub-

sections, the transducer that generates the wavefield is called the source transducer, while the transducer that measures the resulting wavefield is called the receiver transducer. The reader has to keep in mind, though, that for the measurements discussed in the following sections, these terms refer to the same transducer.

3.1.1 Conversion to acoustic energy

A pulser generates a high-voltage electric signal and sends it to the transducer, where the resulting mechanical vibrations act as an acoustic source. Transducers as well as pulsers have specific characteristics, and it is important that the electric signal sent by the pulser is appropriate for the transducer that receives it.

The characteristics of a pulser are often given by the maximum amplitude of the emitted signal, and by the rise-time — the time it takes to reach the maximum amplitude.

The acoustic source wavefield that is generated by the transducer is dependent on the transducer characteristics and on the input signal, delivered by the pulser. Transducers are often characterised by the time- and frequency behaviour of the wavefield they generate — given a well defined electric input signal. The characteristics of the transducers used in the following experiments are given in Section 3.4.

3.1.2 Conversion from acoustic energy

The resulting scattered acoustic pressure P^- registered by the transducer, has to be converted into a format that computers can work with: a series of numbers. The acoustic pressure is converted into an electrical signal by means of the transducer. The resulting signal is a continuous, analogue signal. Since computers work with discrete, digital signals however, a second conversion is needed. In this step, an A/D converter converts the analogue voltage into a series of digital values. A/D converters are characterised by their sampling frequency — the number of conversions they can perform per second — and their resolution — the number of discrete values that a converted signal can have. Typically, the resolution is expressed in the number of bits used by the A/D converter. In the following experiments, an A/D converter with a sampling frequency of 100MHz and a resolution of 12 bits is used.

After the A/D conversion, an integer value in the range $[0 \dots 4096]$ is obtained and stored in ASCII format on a storage medium.

3.2 Transducers

Piezoelectric transducers are described by Bray and Stanley (1997). These transducers convert electric signals into mechanical waves and vice versa. The surface of

a transducer is assumed to be perfectly rigid. As a consequence, the particle velocity is constant along this surface.

3.2.1 Wavefield emitted by a flat cylindrical radiator

A description of the radiation of cylindrical sources can be found in Pierce (1989) or Koek (1991). The surface of the radiator is located in the $\{x, y\}$ plane, with the origin of the coordinate system in the centre of this surface. The configuration is shown in Figure 3.2. Once the normal velocity $V_n(\omega)$ on the surface S of a radiator

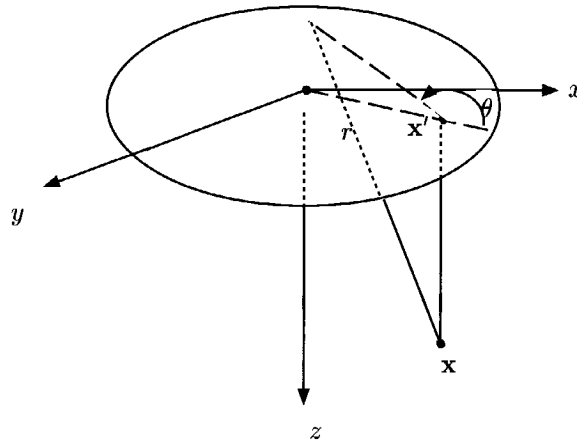


Fig. 3.2 Geometry of a cylindrical radiator with a flat surface. The resulting pressure will be calculated at the point $\mathbf{x} = (x, y, z)$.

is known, the pressure at a point outside this radiator can be calculated using the Rayleigh Integral of the first kind — see Berkhout (1987):

$$P(\mathbf{x}, \omega) = \frac{j\omega\rho}{2\pi} \int_S V_n(\omega) \frac{\exp(-j\frac{\omega}{c}r)}{r} dS, \quad (3.1)$$

where r is the distance between the evaluation point \mathbf{x} and the point of integration on S . If the vertical projection of the evaluation point \mathbf{x} on the plane of the surface of the radiator is located inside this surface, it follows from Equation (3.1) that

$$P(\mathbf{x}, \omega) = \rho c V_n(\omega) \exp(-j\frac{\omega}{c}z) - \frac{\rho c V_n(\omega)}{2\pi} \oint_{\theta=0}^{2\pi} \exp(-j\frac{\omega}{c}r_2(\theta)) d\theta, \quad (3.2)$$

where $r_2(\theta)$ is the distance between the boundary of the surface S and the considered point \mathbf{x} . In Figure 3.3, the amplitude of the wavefield as a function of distance along

the symmetry axis and along the radius is shown for 4 monochromatic waves with a frequency of respectively 5, 10, 15 and 20 MHz. The transducer has a flat circular surface with a radius of 6.356 mm. From the figures, it can be seen that — at

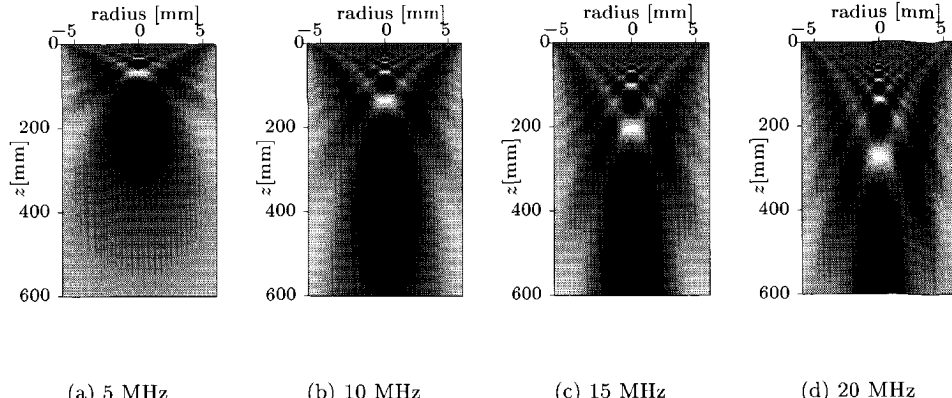


Fig. 3.3 Amplitude of the monochromatic wavefield emitted by a cylindrical transducer with a flat surface. High amplitudes are coloured dark, low (i.e. negative) amplitudes have lighter colours. The radius of the surface is 6.356 mm.

least in the considered region — the positions of the extreme values of the wavefield amplitude are very dependent on the used frequency.

The wavefield at the axis of the transducer can be calculated by varying \mathbf{x} along the z -axis. In this case, Equation (3.2) is written as

$$P(0, 0, z, \omega) = \rho c V_n(\omega) \left(\exp(-j \frac{\omega}{c} z) - \exp(-j \frac{\omega}{c} \sqrt{(R^2 + z^2)}) \right) \quad (3.3)$$

with R the radius of the transducer surface.

Equation (3.3) represents the superposition of two waves, the first being emitted by a plane wave source on the surface of the transducer, the second being emitted by the edge of this surface. Since these waves interfere constructively and destructively with each other, the wavefield along the z -axis shows local minima and maxima. Furthermore, due to the presence of ω in Equation (3.3), the locations of these local extrema are frequency-dependent. The amplitude term of the pressure in Equation (3.3) is given by

$$|P(0, 0, z, \omega)| = \rho c V_n(\omega) \sqrt{2 - 2 \cos \left[\frac{\omega}{c} \left(\sqrt{R^2 + z^2} - z \right) \right]}. \quad (3.4)$$

Figure 3.4 shows this amplitude term for different frequencies. It is clearly observed

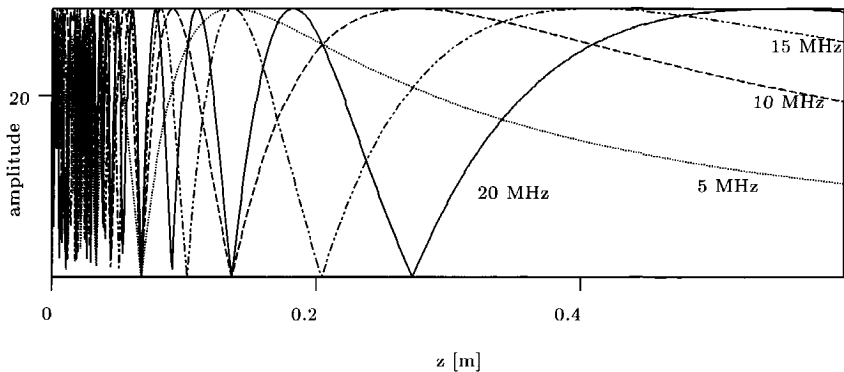


Fig. 3.4 Amplitude term of the acoustic pressure of a flat cylindrical transducer along the symmetry axis.

that close to the transducers surface, the wavefield varies rapidly. This is more pronounced for high frequencies. It can be shown that the last maximum on the symmetry axis occurs at $z = \frac{\omega R^2}{2\pi c}$. The region between the transducer and the position of the last maximum is called the near field.

It will be checked now whether the wavefield in a small region can be considered as a plane wavefield.

From Equations (2.79), (2.80) and (2.81), two important characteristics for plane waves can be derived:

- the amplitude of the wavefield is independent of the depth;
- the phase of the wavefield decays linearly along the z -axis with $\frac{\omega z}{c}$.

In Figure 3.5, the amplitude variations along the z -axis in a small region are shown. It is clearly seen that the amplitude variations are rather large and very frequency dependent.

In Figure 3.6, the phase variations along the z -axis are shown, after being corrected for the linear phase behaviour that occurs in a plane wave. Again, it is clear that these residual phase variations are frequency dependent.

As a consequence, the wavefield emitted by a flat cylindrical radiator can not be assumed to be plane in the region of interest for the experiments in this chapter¹.

¹Due to practical limitations, the distance between the transducer and the target is typically between 10 mm and 100 mm.

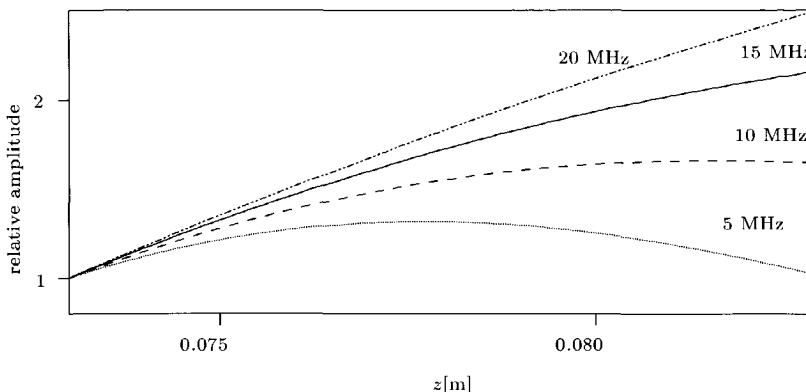


Fig. 3.5 Relative amplitude of the acoustic pressure of a flat cylindrical transducer along a small region at the symmetry axis for different frequencies.

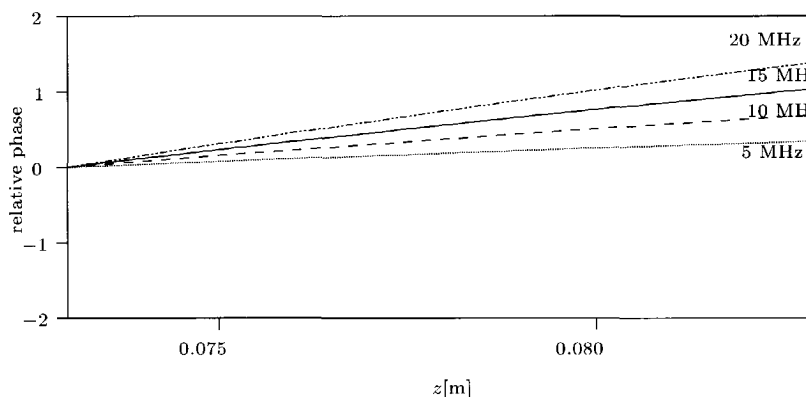


Fig. 3.6 Relative phase of the acoustic pressure of a flat cylindrical transducer along a small region at the symmetry axis for different frequencies, after correcting for the linear plane wave phase term.

3.2.2 Wavefield emitted by a cylindrical focusing radiator

In this subsection, the wavefield emitted by a radiator with a concave cylindrical-symmetric surface vibrating with a uniform normal velocity is calculated. Expressions for this configuration are derived by O'Neil (1949).

A typical example of a vibrating concave radiator is a focussed transducer, used in ultrasonic inspection. Unlike flat transducers, focussed transducers have a curved

radiating surface. One of the consequences of this geometry is that the energy emitted by the secondary sources present at the radiating surface is "focussed" at a specified point. It will be shown that the location of this *focus point* is only slightly frequency dependent.

In addition to the geometry of Figure 3.2, the definitions in Figure 3.7 have to be considered.

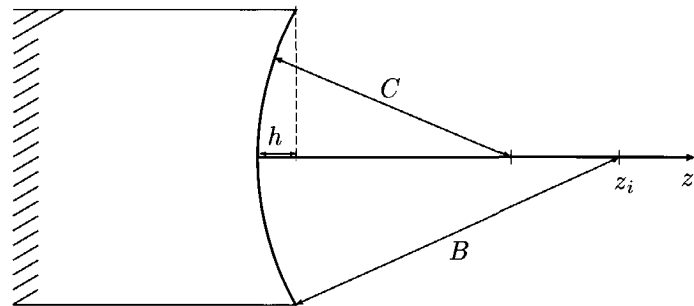


Fig. 3.7 Geometry of concave spherical radiator.

The radius of curvature of the radiating surface is given by C and the depth of the transducer, h , is the distance between the centre of the transducer surface and the projection of the boundary of the surface on the z -axis (see Figure 3.7). Further, B is the distance between the observation point on the axis and the boundary of the surface. Assuming that both the wavelength and the depth of the transducer h are small compared with the radius C , the Rayleigh integral of Equation (3.1) for an observation point located at the symmetry axis $\{x, y\} = 0$ can be approximated by

$$\begin{aligned} P(\mathbf{x}, \omega) = P(0, 0, z, \omega) &\simeq j\omega\rho V_n(\omega) \frac{C}{C-z} \int_z^B \exp(-j\frac{\omega}{c}r) dr \\ &= j\rho c V_n(\omega) \frac{2C}{C-z} \sin\left(\frac{\omega}{c} \frac{t(z)}{2}\right) \exp\left(-j\frac{\omega}{c} M(z)\right) \end{aligned} \quad (3.5)$$

with

$$t(z) = B - z \quad (3.6)$$

and

$$M(z) = \frac{B+z}{2}. \quad (3.7)$$

An approximation for the position of the maximum pressure on the z -axis is given by

$$z_{max} \simeq C - \frac{12C}{\frac{\omega^2}{c^2}h^2 + 12} \quad (3.8)$$

In Figure 3.8, the amplitude of the pressure is given as a function of the distance z towards the transducer. The considered transducer has a surface radius of 6.35 mm and a curvature radius of 76 mm. The acoustic velocity c of the considered medium is 1480 ms^{-1} and the amplitude for 4 frequencies is displayed.

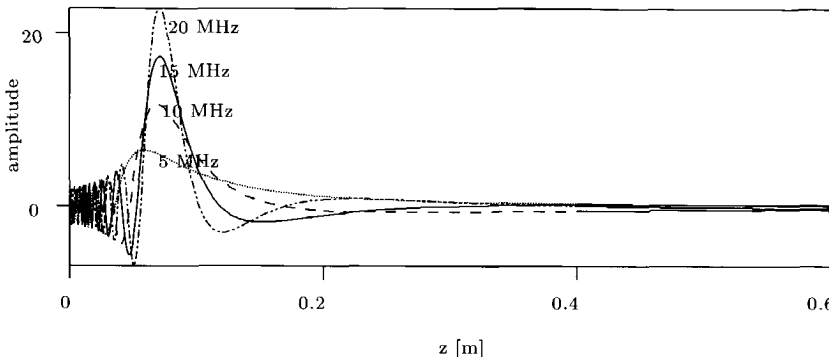


Fig. 3.8 Amplitude of the acoustic pressure of a focussed transducer along the symmetry axis.

Comparing Figure 3.8 with Figure 3.4, it follows that the locations of the maximum amplitude for different frequencies are closer to each other when a focussed transducer is used. In this context, the term focus zone is used to indicate the region along the z -axis where the monochromatic waves that are present in the source wavefield have their maximum value.

Between the transducer and z_{max} , the amplitude of the pressure shows rapid fluctuations. In this region, the pressure is extremely sensitive to changes in distances. In the neighbourhood of z_{max} , the pressure still shows variation with the distance but they are smoother. The amplitude variations in a region around the focus point are shown in Figure 3.9, and the phase variations — after being corrected for the linear plane wave phase term — are shown in Figure 3.10.

In a *small* region around the focus point, the amplitude term is almost constant, and the phase variations almost follow the phase variations that are present in plane waves. Therefore, the wavefield in a small region around the focus point — the focus zone — can be assumed to be plane. Note that the considered laminated target materials have a thickness that generally fits within this focus zone.

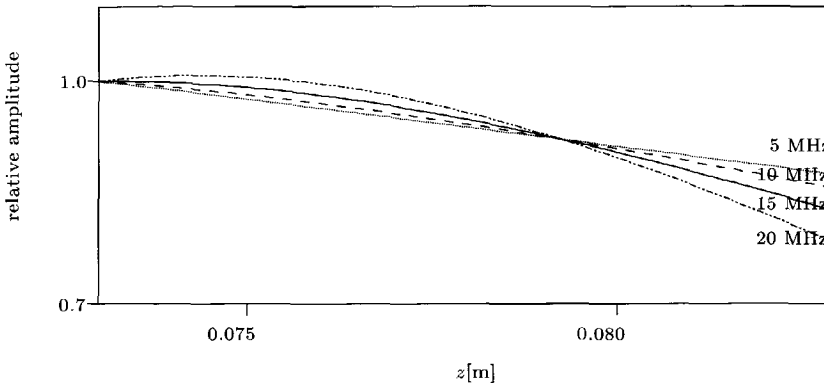


Fig. 3.9 Amplitude of the acoustic pressure of a focussed transducer along a small region at the symmetry axis for different frequencies.

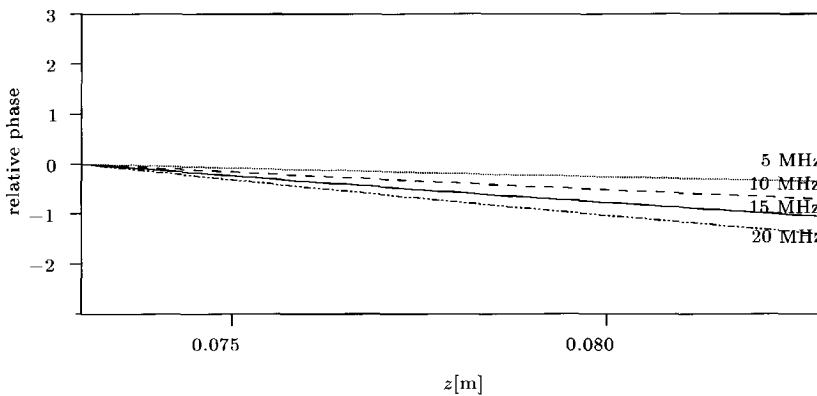


Fig. 3.10 Phase of the acoustic pressure of a focussed transducer along a small region at the symmetry axis for different frequencies, after correction for the linear plane wave phase term.

3.3 Preprocessing

Since most processing algorithms use floating point values, it is necessary to convert the ASCII numbers into a floating point format. The first step in the preprocessing converts the obtained ASCII values into a 32-bit IEEE float-representation. During this conversion, the floating point values are "centred" around the zero-axis, since the ASCII values all are positive numbers, while the pressure can be both positive and negative.

In the forward model — as developed in Chapter 2 — the influence of "noise" is neglected. It is assumed that the measured values are the perfect mathematical results of a functional acting on a test function. The devices that convert these physical quantities into a series of numbers, are not perfect though.

In practice, the *clean* signal will be more or less disturbed, due to several phenomena. The influence of the measurement on the measured value is described by Sydenham (1982) and a statistical treatment of the measured values can be found in Johnson and Leone (1977). The difference between the actual signal and the signal that would be present if only the phenomena described in Chapter 2 were present, will be called *noise*.

A classification of measurement errors that result in the presence of noise, is given by Sydenham (1982). Two types of noise are distinguished here²: noise due to systematic errors, and noise due to random errors. The first type of noise may occur in the A/D converter, when some component is badly calibrated and produces an erroneous value, independent of the nature of the measurement — i.e. an amplifier having a constant but non-linear behaviour.

The second type of noise is also called random noise, *white noise* or *uncorrelated noise* since — in contradistinction to systematic noise — the noise in one measurement is independent from the noise in another measurement. The expected value for this noise is zero, which is expressed by

$$\mathcal{E}(n) = \lim_{N \rightarrow \infty} \frac{1}{N} \sum_{j=1}^N n_j = 0. \quad (3.9)$$

The operator \mathcal{E} returns the expected value of the argument, n_j is the noise present in measurement j and N is the number of performed measurements. If there is only white noise present in a measurement, the measured value y_j is related to the noise-free signal s_j by

$$y_j = s_j + n_j. \quad (3.10)$$

Since the signal part s_j is assumed to be repeatable and constant, it follows that

$$\mathcal{E}(s_j) = s_j = s. \quad (3.11)$$

If the wavefield is represented by its pressure, the energy in that wavefield is proportional with the squared pressure. Since the wavefield contains a real signal-portion and a noise-portion, the signal-to-noise ratio can be defined by

$$sn = \sqrt{\frac{|s|^2}{|n|^2}}. \quad (3.12)$$

²The two types of noise described here are only two extreme types. In practice, there exist many intermediate types of noise, which are a combination of systematic noise and random noise.

The expected value for this signal to noise ratio is, for a single measurement, given by

$$\mathcal{E}(sn) = \sqrt{\frac{s^2}{\mathcal{E}(|n|^2)}}. \quad (3.13)$$

stacking

Adding the results of measurements all done under repeatable conditions leads to

$$\sum_{j=1}^N y_j = \frac{1}{N} \sum_{j=1}^N (s_j + n_j). \quad (3.14)$$

This procedure is known as *stacking*. The expected value for the signal to noise ratio in the stack is now given by

$$\mathcal{E}(sn) = \sqrt{\frac{N^2 s^2}{\mathcal{E}(\sum_{j=1}^N n_j^2)}}. \quad (3.15)$$

Since for uncorrelated noise it holds that $\mathcal{E}(\sum_{j=1}^N n_j^2) = N\mathcal{E}(|n_j|^2)$, it follows that the signal to noise ratio for the sum of the measurements has increased with a factor \sqrt{N} .

Stacking also allows one to predict the probability that the result of a measurement will occur in a given interval. The standard deviation on a series of N measurements y_j is defined as

$$\sigma_y = \sqrt{\frac{\sum_{j=1}^N y_j^2}{N - 1}}. \quad (3.16)$$

If the measured quantity y is randomly distributed around a central value $\mathcal{E}(y)$ — i.e. the noise follows a Gaussian distribution —, probability-intervals can be defined. For example, there is a 99% probability that a next measurement will be located in the interval $[\mathcal{E}(y) - 3\sigma_y, \mathcal{E}(y) + 3\sigma_y]$. More information on probability, standard deviation and its applications can be found in the statistical literature — e.g. Mood (1987).

aligning

For reasons explained below, it is not relevant to simply add the data obtained by the measurements performed in this research. The trigger system is known to be very inaccurate and not reliable. This shortcoming in hardware is compensated

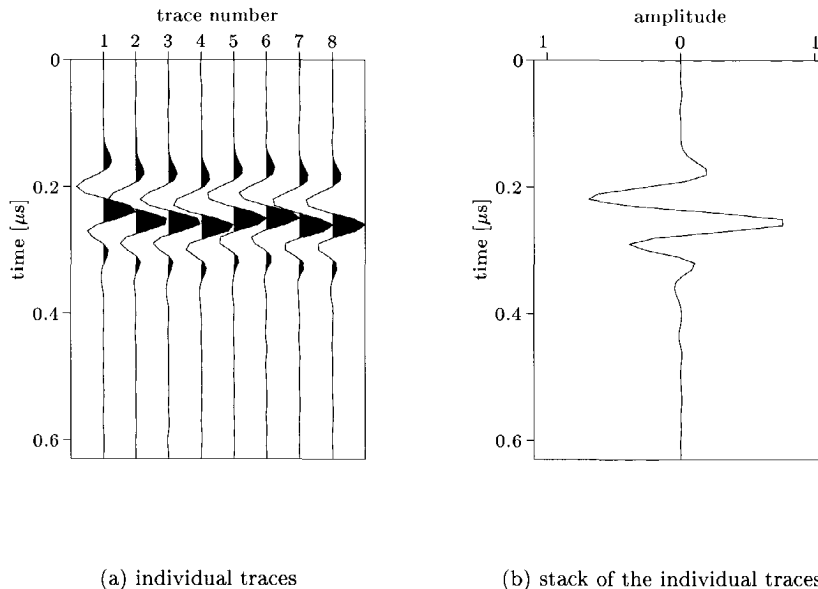


Fig. 3.11 Stacking of 8 successive reflection measurements of a glass beam embedded in water. After stacking, the signal has a maximum value of 0.758.

for by software. The data obtained by 8 successive measurements is shown in Figure 3.11(a). These measurements are obtained from the reflection of the source wavefield due to a glass beam embedded in water, and are treated in more detail in the next section. The traces are normalised, i.e. all samples are divided by the value of the maximum sample occurring in the trace.

The measurements were taken without changing any environment variable, and the arrival time should be the same, but this is apparently not the case. The trace in Figure 3.11(b) is obtained by adding the 8 corresponding values in the different traces for each time sample. The values in the resulting trace are divided by the number of traces added.

Since the positions of the maximum value in the different traces are not the same in each trace, the maximum value in the stack will not equal the sum of the maximum values in each trace divided by the number of traces. An improvement is obtained by aligning the traces in such a way that the maximum value in each trace occurs at a fixed position. In Figure 3.12(a), each trace is shifted and the maximum value occurs at sample 15 — which occurs at $0.14 \mu\text{s}$. Due to the normalisation of the individual traces, the maximum value of the averaging procedure after this alignment equals unity. Comparing the average of these traces — Figure 3.12(b) — with Figure 3.11(b) shows that the obtained signal is higher now, resulting in a better signal-to-noise ratio.

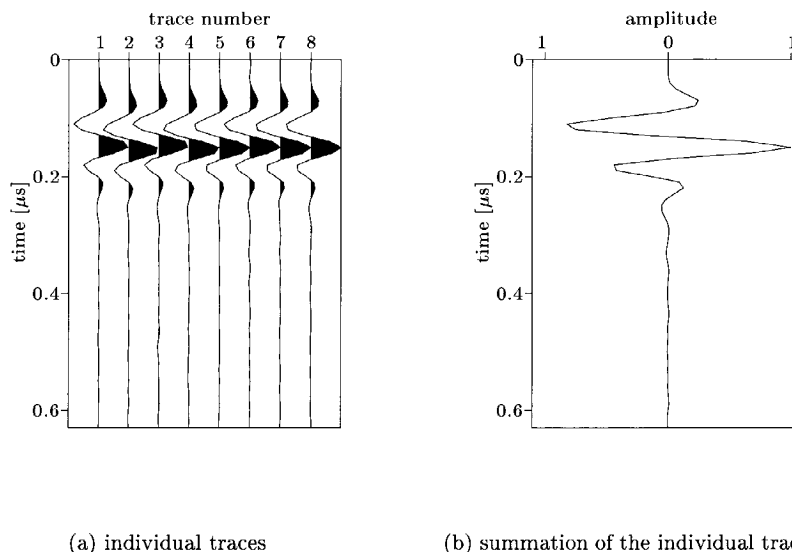


Fig. 3.12 Stacking of 8 successive reflection measurements of a glass beam embedded in water. The traces in Figure 3.12(a) are obtained by shifting the traces in Figure 3.11(a) with a discrete number of samples until their maximum value occurs at sample 15. The maximum value in the stacked signal is now 1.00.

Also, when adding non-aligned traces to each other, the resulting wavelet will be smoother, and high-frequency information is lost.

peak detection

Due to the fact that the signal is sampled at discrete time intervals, it is very unlikely that the maximum value of the continuous signal will occur at a sample point. Different methods can be applied in order to estimate the position and value of the maximum value that occurs in the continuous signal. These peak detection methods will be described in the next chapter. A fast and — for the current purpose — sufficient method is the polynomial interpolation.

A second-order polynomial interpolation is performed for obtaining a better approximation of the position of the maximum. The sampled maximum value and the two adjacent points are used for this interpolation. This method will return the exact position of the maximum if the signal can be described by a parabolic equation in the neighbourhood of its maximum. The result of this procedure is given in Figure 3.13. Although the improvement obtained by this method might be rather small it is an important one — as will be shown later.

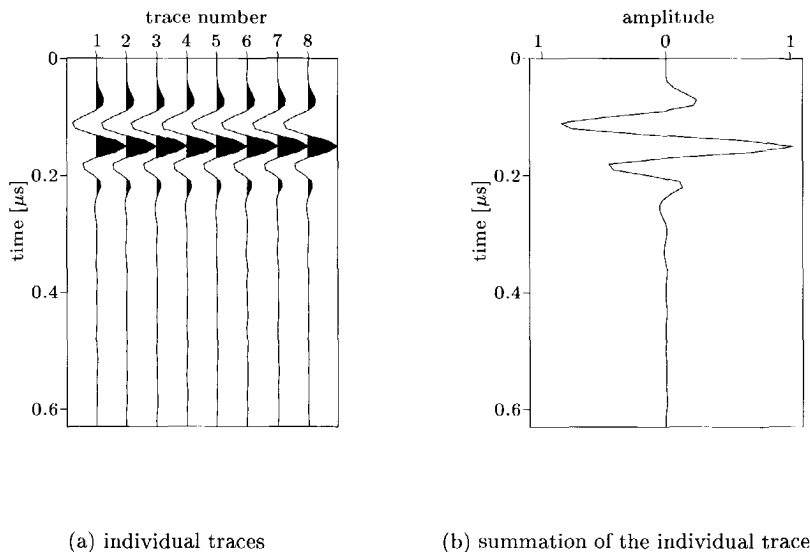


Fig. 3.13 Stacking of 8 successive reflection measurements of a glass beam embedded in water. The traces in Figure 3.12(a) are obtained by shifting the traces in Figure 3.11(a) with their maximum value at sample 15. A second order polynomial interpolation is used to detect the maximum in each trace. The maximum value in the stacked signal is now 1.03.

The grey level plots in Figure 3.14 show the influence of the alignment by means of a peak-detection and a second order polynomial interpolation in the preprocessing for a set of 256 successive measurements.

3.4 Source signal

Together with the response function of the configuration, the signal emitted by a transducer is responsible for the received scattered wavefield. In the frequency domain, this is expressed by

$$P_0(\omega) = X_0(\omega)S(\omega), \quad (3.17)$$

where P_0 is the pressure of the scattered wavefield at the transducer, X_0 is the response function of the material due to an impulse at the transducer position and S is the frequency-domain representation of the used source.

The knowledge of the source-signal is important both for performing simulations — as is shown in Chapter 2 — and for applying the inversion algorithms — as will be shown in Chapter 4 and Chapter 5.

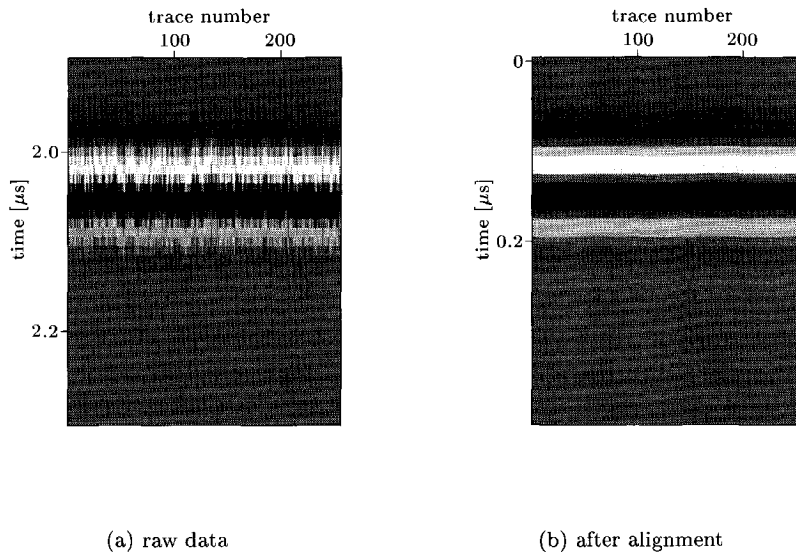


Fig. 3.14 Preprocessing of 256 successive measurements. A time-shift is applied to all traces in (a) until their maximum value occurs at $0.15 \mu\text{s}$

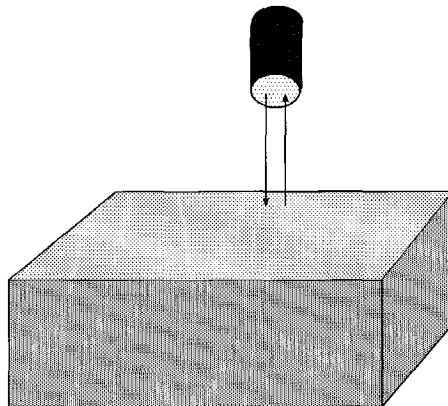


Fig. 3.15 Setup for the measurement of the source signal. A transducer and a glass beam are embedded in water.

The signal emitted by a transducer is dependent on the geometrical and material properties of the transducer. In order to perform reliable simulations, the source signal has to be highly repeatable. This property is tested for three different transducers. The source signal is obtained by measuring the reflection of the emitted wavefield on a homogeneous glass beam. The setup is shown in Figure 3.15.

The whole configuration — transducer and target material — is embedded in water. The energy emitted by the transducer travels through the water towards the glass beam. Part of the energy is reflected there, and another part is transmitted into the glass. The reflected energy travels through the water back to the transducer where it is recorded. The thickness of this glass beam is chosen such that no other reflections occur in a time window that is large enough to hold the first reflection.

The distance between the transducer and the target will be chosen in such a way that the first reflection contains as much energy as possible. For focussed transducers this means that the target should be placed near the focus point — see subsection 3.2.2. For flat cylindrical transducers, the maximum value of the wavefield along the axis of the transducer is strongly frequency dependent. The distance between transducer and target is chosen in such a way that the energy of the first reflection is maximal.

3.4.1 15 MHz, unfocused transducer

A 15 MHz Panametrics transducer³ is placed at about 50 mm above a glass beam. The source-signal, being the result of the preprocessing procedure described in the previous section, is shown in Figure 3.16(a). The resulting signal in this figure is obtained by adding 512 aligned measurements⁴. In order to check for the repeatability of the signal, some basic statistical operations are performed. The individual traces are denoted by $s_j(t)$ or more compactly s_j where j varies from 1 till N with N the number of performed measurements. The resulting source signal obtained by the preprocessing is called $s(t)$. For each sample point of $s(t)$, the standard deviation $\sigma(t)$ can be calculated, using

$$\sigma(t) = \sqrt{\frac{\sum_{j=1}^N (s_j(t) - s(t))^2}{N - 1}}. \quad (3.18)$$

The standard deviation is an indication for the repeatability of the signal. Larger variations between the different traces will result in a higher standard deviation. In Figure 3.16(b), the 99% probability interval is plotted for all samples in the time-region of interest. The smaller this interval is, the more repeatable the measurements are.

Since a number of calculations — both in simulations and inversion algorithms — are performed in the frequency-domain, the frequency-content of the source-signal

³The term 15 MHz is used for naming conventions, and it does not mean that this transducer only generates a monochromatic wave of 15 MHz. The name is used to indicate that the energy content in the frequency domain of the wavefield emitted by this transducer is centred around 15 MHz, as will be shown in this subsection.

⁴Before the measurements are aligned, the traces are scaled so that they contain an equal amount of energy.

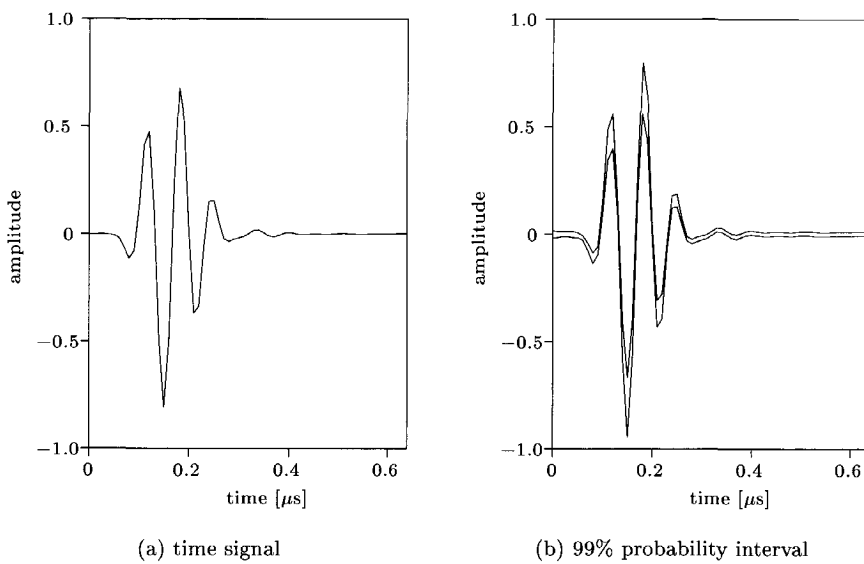


Fig. 3.16 Source signal emitted by a non-focussed Panametrics transducer with a centre frequency of 15 MHz.

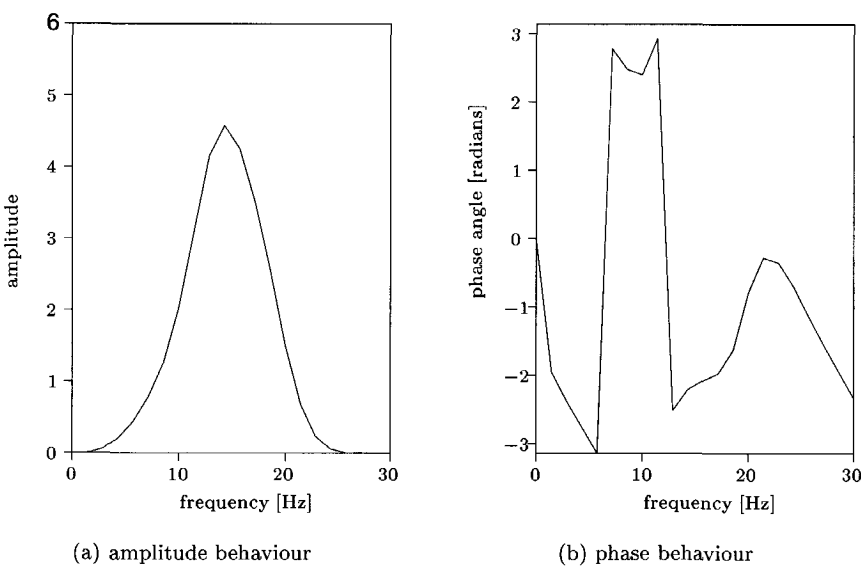


Fig. 3.17 Frequency content of the source signal from the 15 MHz non-focussed transducer — see Figure 3.16(a).

is of particular interest. In Figure 3.17, the amplitude and phase information of the source-signal as a function of the frequency is given.

A problem with this transducer is that the plane wave approach is not valid at the depth of 50 mm. Indeed, it has been shown in section 3.2.1 that fast and frequency-dependent fluctuations of the energy contained in the wavefield occur in this region.

3.4.2 15 MHz, focussed transducer

The experimental results in this section are obtained using a Panametrics transducer with a centre frequency of 15 MHz, and with a focus point at 76.2 mm. Applying the preprocessing procedure on 256 successive measurements results in a time-signal shown in Figure 3.18(a). The 99% probability interval is given in Figure 3.18(b).

The frequency behaviour of this transducer is shown in Figure 3.19 — both the amplitude term and the phase term are given.

An advantage of this transducer over the previous one is that the plane wave approach is valid at a reasonable depth — 76.2 mm.

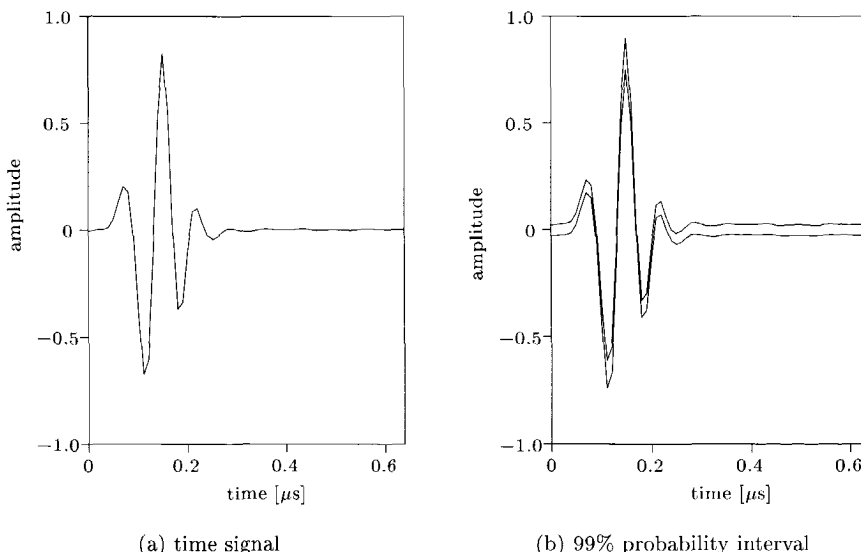


Fig. 3.18 Source signal from a 15 MHz transducer, focussed at 76.2 mm.

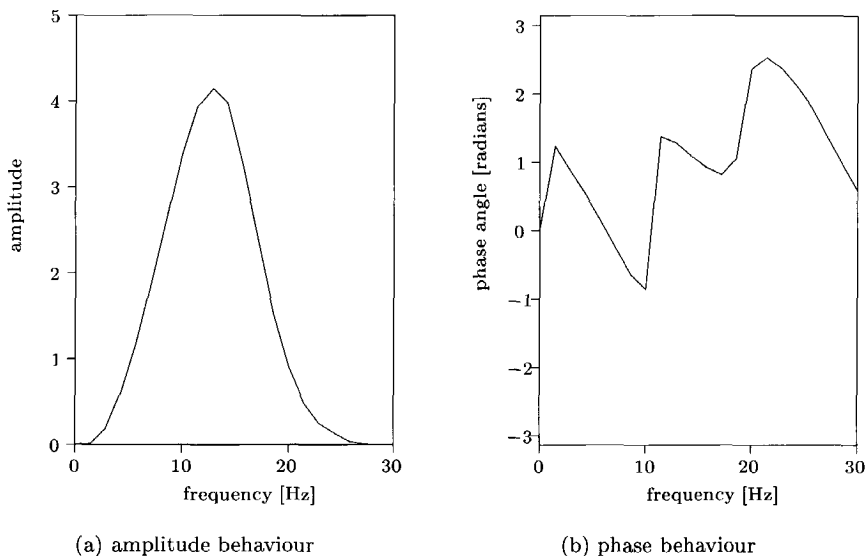


Fig. 3.19 Frequency content of the source signal from a 15 MHz transducer focussed at 76.2 mm.

3.4.3 20 MHz, focussed transducer

The results in this section are obtained using a Panametrics transducer with a centre frequency of 20 MHz, and with a focus point at 50.8 mm. Applying the preprocessing procedure on 256 successive measurements results in a time-signal shown in Figure 3.20(a). The 99% probability interval is given in Figure 3.20(b). The frequency behaviour of this transducer is shown in Figure 3.21. The frequency behaviour of this transducer is shown in Figure 3.21. From the frequency spectrum, it follows that this transducer shows relatively high amplitudes for higher frequencies. As a consequence, finer details can be distinguished. A drawback of this transducer, however, is that the emitted energy is smaller than the energy emitted by the 15 MHz focussed transducer. Also, the repeatability of the signals from the 20 MHz transducers tends to be lower than the repeatability of the source signal from the 15 MHz focussed transducer — compare Figure 3.20(b) with Figure 3.16(b) and Figure 3.18(b).

The choice of an optimal transducer therefore is a compromise between time resolution, repeatability and power.

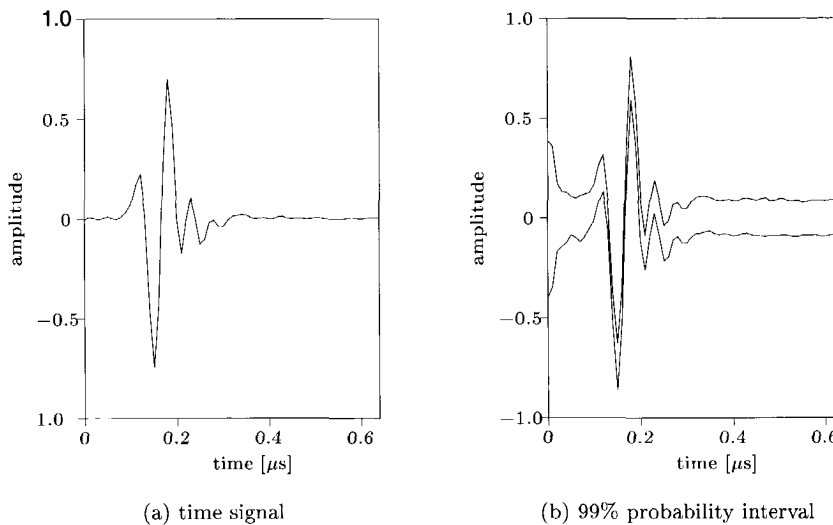


Fig. 3.20 Source signal from a 20 MHz transducer, focussed at 50.8 mm.

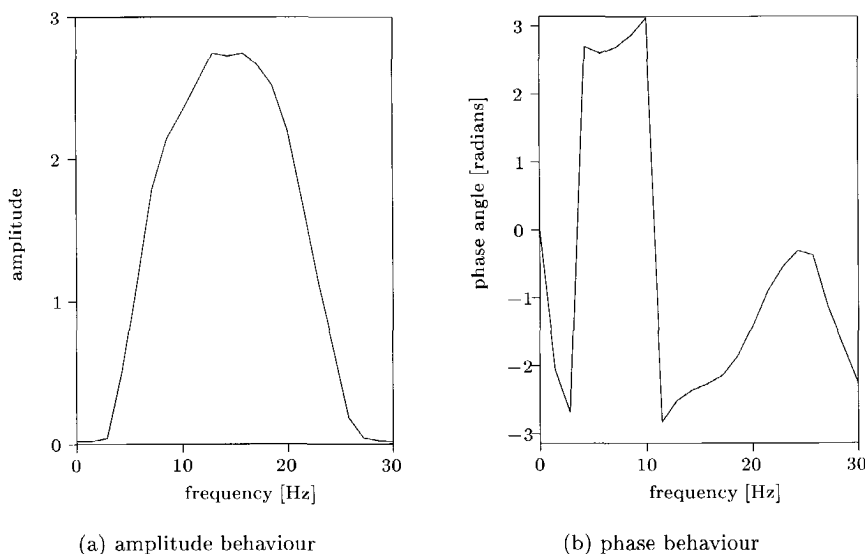


Fig. 3.21 Frequency content of the source signal from a 20 MHz transducer focussed at 50.8 mm.

3.5 Reflection measurements

The measurements in the previous section are reflection measurements — the wavefield is generated and recorded at the same side of the material. They are primarily meant for qualifying and quantifying the source wavefield, though.

In this section, more reflection measurements are performed. After preprocessing the data, they are compared with the results from simulations — using the theory developed in Chapter 2.

3.5.1 Aluminium disk

In this experiment, a homogeneous aluminium disk is embedded in water. The thickness of the disk is about 0.8 mm and the lateral dimensions are large compared with the thickness. A transducer with a focus zone at 76.2 mm and a centre frequency of 15 MHz is placed at about 77 mm above the material — the transducer is under the water level. The setup is the same as the configuration for the characterisation of the source signal, except that the glass beam is replaced by a thin aluminium disk. In this experiment 256 successive measurements are performed. Each measurement contains 4096 samples, making the recording time for each trace $40\mu\text{s}$. In Figure 3.22(a) the result of this scan is shown. Again, note the different time-offset values of the first reflections, due to a non-consistent hardware trigger. In Figure 3.22(b) the traces are aligned so the first reflection of each trace occurs at the same time.

Since the measurements are all performed using the same geometrical configuration, it is expected that all traces look the same. To check this repeatability, a statistical analysis is performed on the 256 traces. In Figure 3.23(a) the average of the 256 traces is calculated. In Figure 3.23(b) the 99% probability interval is shown.

The 99% probability interval is rather large for small values in the trace. This is understandable since there is always some level of background noise present. When the signal has a low amplitude, the noise is more noticeable. Especially in regions where the signal is low, the effect of stacking is important.

In Figure 3.24, the predicted wavefield based on the theory in Chapter 2 is shown and compared with the measured data. For this prediction, the actually measured source signal of the 15 MHz focussed transducer has been used. The predicted wavefield looks very similar to the actual measured data.

Obtaining information from internal multiples

Both in the measured and the predicted wavefield, multiple reflections can clearly be distinguished. Although multiples are often considered as doing harm to the data, in some cases they provide valuable information.

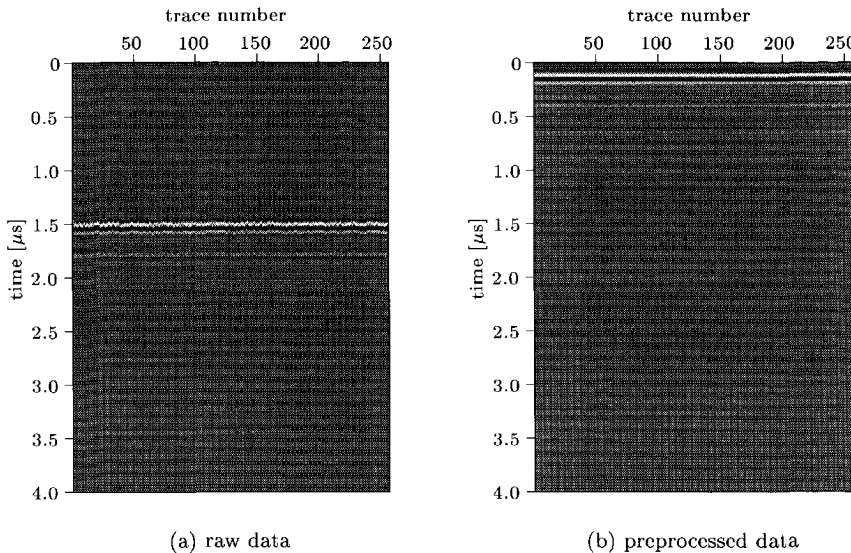


Fig. 3.22 Reflection measurements on an aluminium disk of 0.8 mm thickness. The effect of preprocessing is shown.

The distance between the multiples is an indication for the thickness of the layer, and the decrease in amplitude is related to the reflection coefficients at the interfaces between the layers.

Performing cubic interpolation with the use of 3 samples around the peak value in each multiple reflection reveals the two-way traveltimes in a layer and the amplitudes of the considered reflections with a sufficient accuracy.

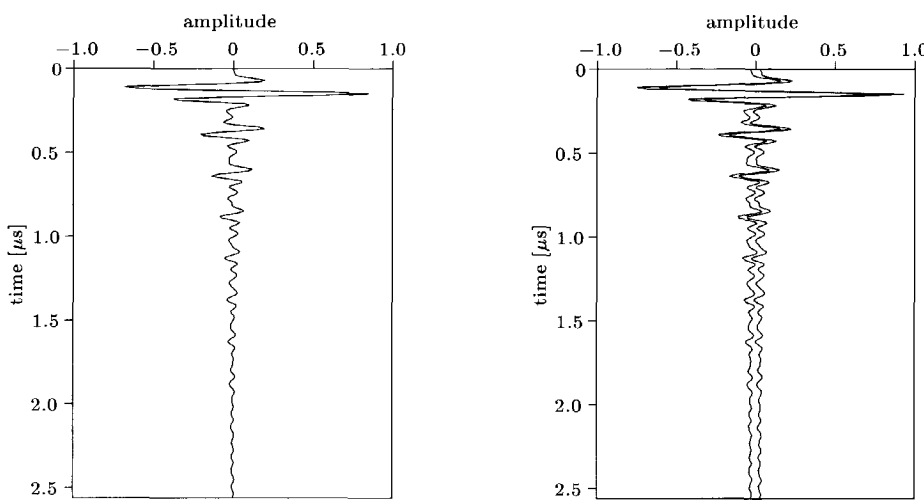
It can easily be shown that in the case of a one-layered material, the decrease in amplitude is related to the reflection coefficient water-aluminium – being R_0 – by

$$\frac{A_{i+1}}{A_i}^{-1} = R_0^2, \quad (3.19)$$

where A_i is the amplitude of the maximum value in the i -th multiple.

In Table 3.1, the calculated reflection coefficients and the two-way traveltimes based on a comparison between subsequent multiples are given.

The series of estimated reflection coefficients is reasonably centred around the real reflection coefficient – which is $R_0 = 0.84206$ – with only minor deviations. This is an indication that the plane wave theory for an instantaneously reacting medium – as developed in Section 2.2.2 – can be applied to the case of a "thin" aluminium layer embedded in water and located in the focus zone of a focussed transducer.



(a) Reflection measurement on an aluminium disk after preprocessing

(b) 99% probability interval

Fig. 3.23 Reflection measurement on an aluminium disk with 0.8 mm thickness.
Figure 3.23(a) shows the time signal after stacking 256 aligned measurements.

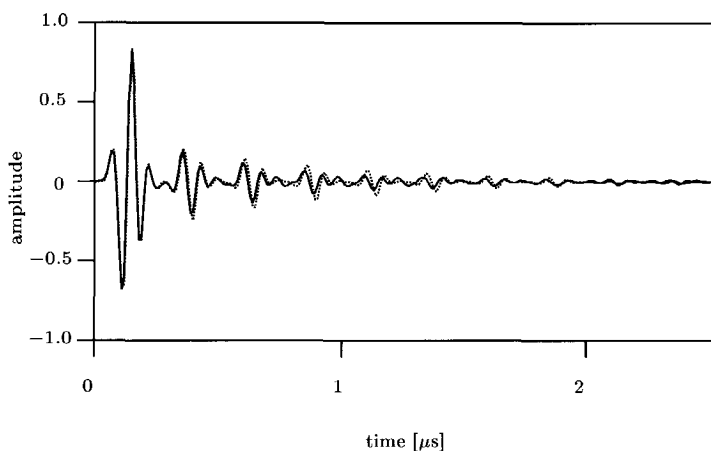


Fig. 3.24 Reflection on aluminium disk, a comparison between the measured (solid line) and predicted (dotted line) signal.

Derivation of R_0 and Δt			
Multiple	R_0	$\Delta t[\mu\text{s}]$	thickness (mm)
1-2	0.8663	0.24380	0.768
2-3	0.7989	0.24610	0.775
3-4	0.7897	0.24416	0.769
4-5	0.8039	0.24549	0.773
5-6	0.8557	0.24803	0.781
6-7	0.8241	0.24929	0.785
7-8	0.8253	0.25370	0.799
8-9	0.7832	0.25488	0.803

Table 3.1 Calculated reflection coefficient for a water-aluminium interface, two-way traveltimes in the aluminium layer and thickness of the layer, based on each pair of subsequent internal multiples.

Composition of Prepreg samples			
Name	number of layers	orientation	thickness (mm)
Prepreg-2	2	0-90	0.25
Prepreg-3	3	0-90-0	0.375

Table 3.2 Structure of the two different inspected prepreg samples.

3.5.2 Prepreg

A prepreg layer consists of glass fibres in an epoxy resin. The structure of prepreg is discussed in Appendix A. In this subsection, two configurations of prepreg are inspected. Their composition is given in Table 3.2.

Again, for each prepreg sample 256 successive measurements are performed, recording 4096 samples with a sampling rate of 100 MHz. Figure 3.25 shows a time-window of these measurements after removing the static component and applying a Butterworth bandpass filter⁵ suppressing frequencies below 3 MHz and above 26 MHz. The first preprocessing step is the same as in the case of a reflection on an aluminium disk: the traces are aligned in a way that the peaks of the first reflections occur at the same position. The result of this step is given in Figure 3.26. Again, the average time-traces for both experiments are calculated after the traces have been aligned. Together with the 99% probability interval, the results are shown in Figure 3.27. Comparing the preprocessed signal from Figure 3.27(a) with the predicted signal from Figure 2.15 shows that the forward model without attenuation cannot be used here. The amplitude of the arrivals at later times are overestimated in Fig-

⁵A description of this bandpass filter can be found in the literature — e.g. Chua et al. (1987).

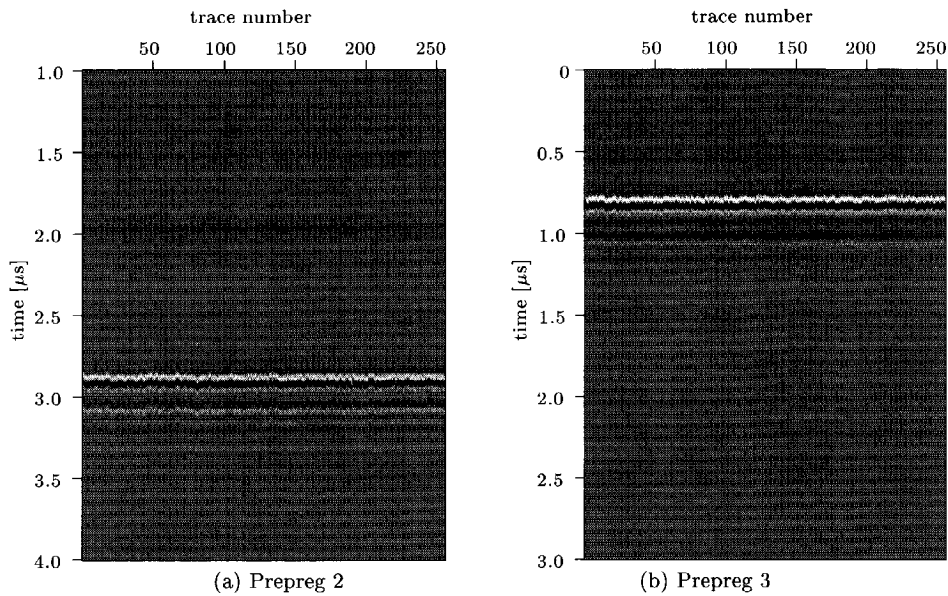


Fig. 3.25 Reflection measurements on two prepreg samples. A Butterworth bandpass filter has been applied, but no further preprocessing has been done.

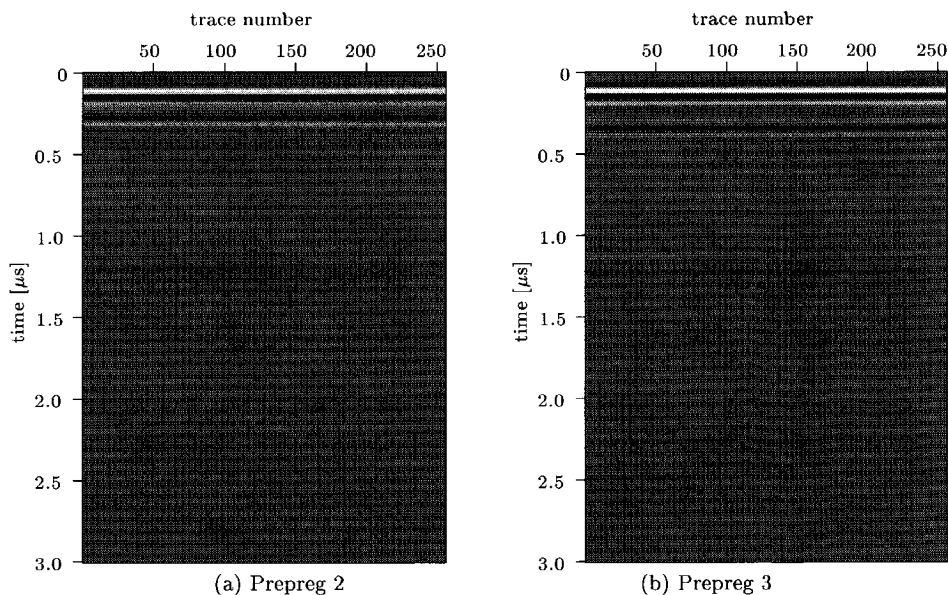


Fig. 3.26 Reflection measurements on the prepreg samples from Figure 3.25 after aligning the traces to each other.

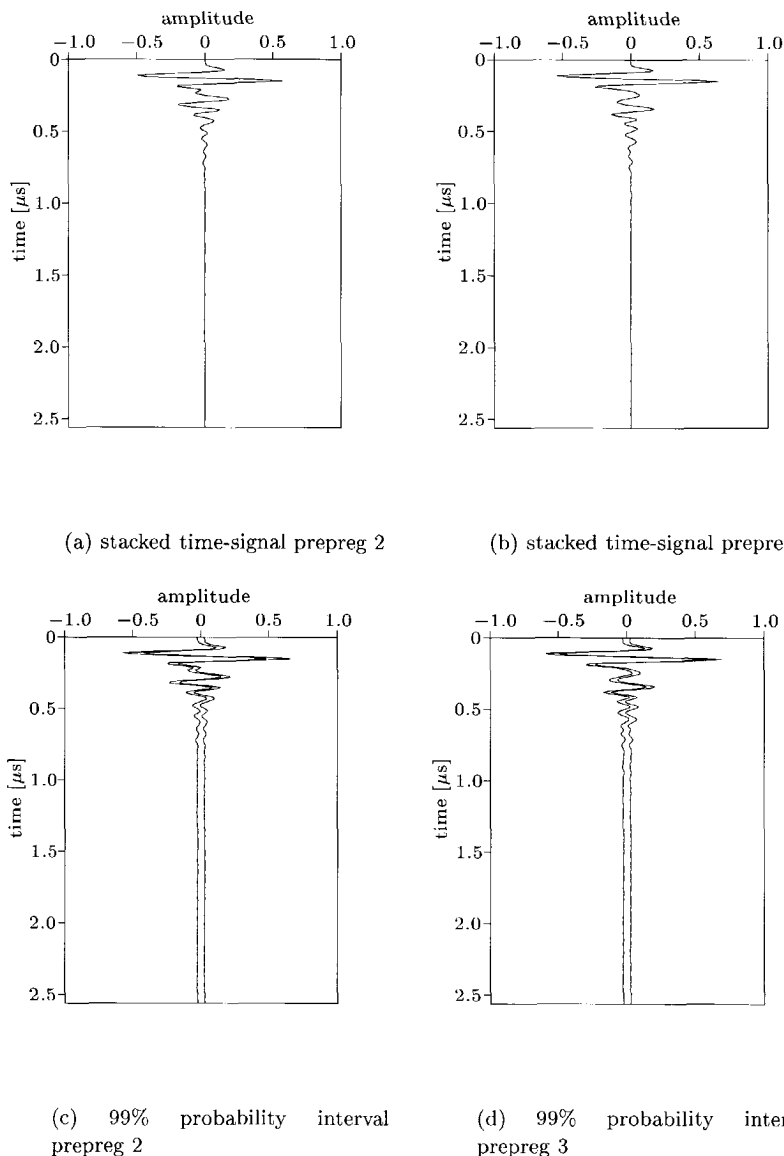


Fig. 3.27 Reflection measurements on two prepreg samples according to the configurations of Table 3.2; 256 traces are aligned and stacked. (a) and (b) show the time-averaged values, (c) and (d) show the 99% probability interval.

ure 2.15(a).

The measurement is compared with the results predicted by the forward model using attenuation coefficients of respectively 0, 1000 and 2000 m^{-1} and the results are shown in Figure 3.28.

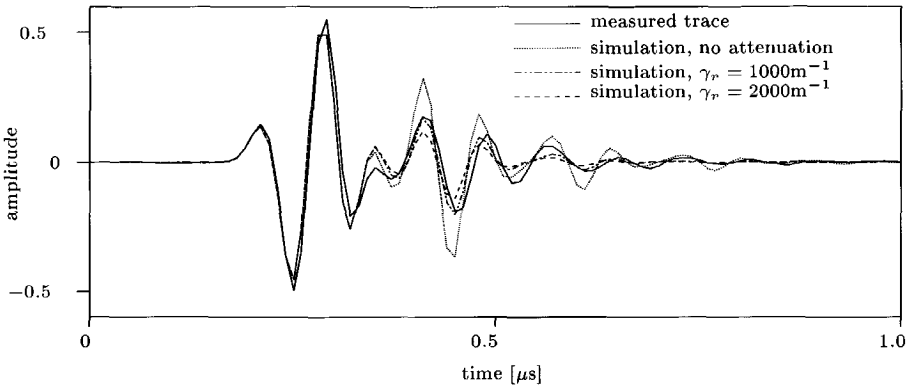


Fig. 3.28 Comparison between predicted and measured prepreg reflection responses on a Prepreg-2 sample.

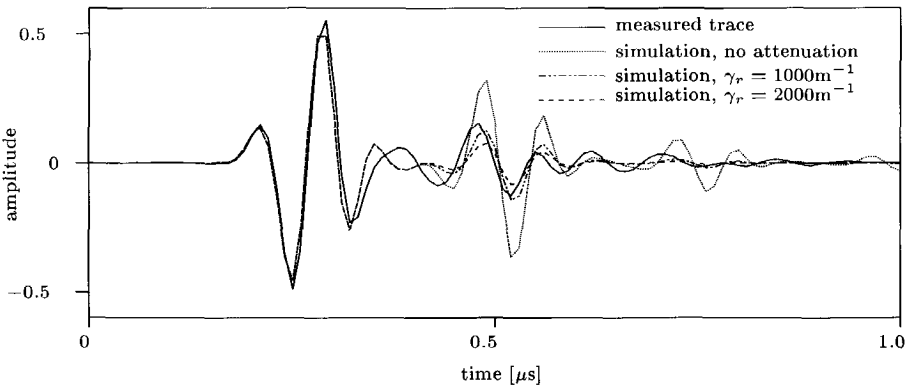


Fig. 3.29 Comparison between predicted and measured prepreg reflection response on a Prepreg-3 sample.

The same procedure is followed for the Prepreg-3 sample, and the results are shown in Figure 3.29. Although there is no perfect match, it can be seen that the use of an attenuation coefficient of 1000 m^{-1} gives the best result.

Hence, including the attenuation phenomena introduced in Section 2.3 in the for-

First Glare 2/1 target in water					
Layer	material	Δz (mm)	ρ ($\frac{\text{kg}}{\text{m}^3}$)	v ($\frac{\text{m}}{\text{s}}$)	γ_r (1/m)
0	water	76	1000	1480	0
1	aluminium	0.3	2740	6300	0
2	prepreg	0.250	1600	3100	1000
3	aluminium	0.3	2740	6300	0
4	water	∞	1000	1480	0

Table 3.3 Structure of the first Glare sample

Second Glare 2/1 target in water					
Layer	material	Δz (mm)	ρ ($\frac{\text{kg}}{\text{m}^3}$)	v ($\frac{\text{m}}{\text{s}}$)	γ_r (1/m)
0	water	76	1000	1480	0
1	aluminium	0.4	2740	6300	0
2	prepreg	0.250	1600	3100	1000
3	aluminium	0.4	2740	6300	0
4	water	∞	1000	1480	0

Table 3.4 Structure of the second Glare sample

ward model, results in better predictions when the target material is prepreg. The model incorporates friction and viscosity in the medium, two phenomena that allow the dissipation of acoustic energy.

Since there is no perfect match yet, it is reasonable to assume that also other phenomena occur inside the prepreg material. Note that prepreg is a heterogeneous medium (fibres are embedded in resin), and the exact wavefield propagation effects are not fully understood yet.

Furthermore, there can be an actual deviation for material properties (density, velocity) and thickness that can contribute to this mismatch.

3.5.3 Glare

The structure and naming convention of Glare is explained in Appendix A. In this subsection, reflection measurements are performed on two different glare-configurations. Their setups are given in Tables 3.3 and 3.4.

The targets are embedded in water, and the distance between the target and the focussed 15 MHz transducer — described in Subsection 3.4.2 — is about 76.2 mm. This means that the target is located in the focus zone of the transducer.

For each glare configuration 256 successive measurements are performed, recording

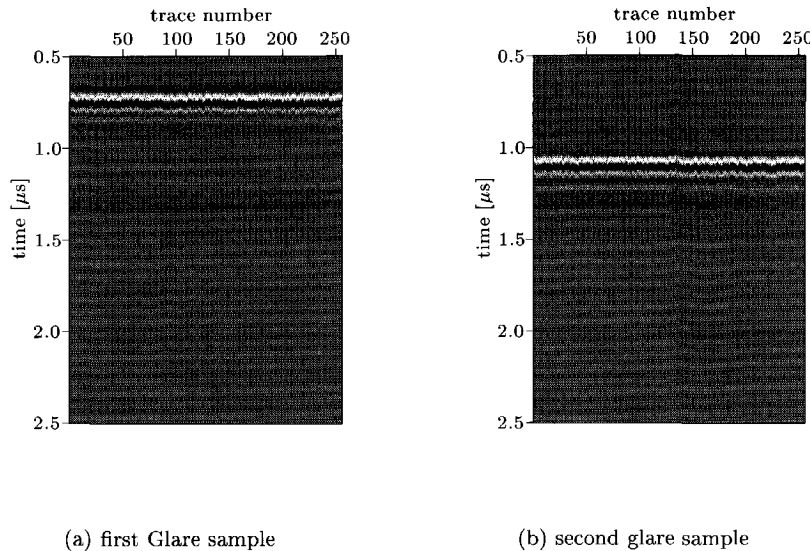


Fig. 3.30 Reflection measurements on two Glare samples, before data preprocessing. The configurations of the samples are given in Table 3.3 and Table 3.4.

4096 samples with a sampling rate of 100 MHz. Figure 3.30 shows a time-window of these measurements after removing the static component and applying a Butterworth bandpass filter suppressing frequencies below 3MHz and above 26MHz.

The first preprocessing step is the same as in the case of a reflection on an aluminium disk or on a prepreg sample: the traces are aligned in such a way that the peaks of the first reflections occur at the same position in each trace. The result of this step is given in Figure 3.31. Again, the average time-traces for the two experiments are calculated. Together with the 99% probability interval, the results are shown in Figure 3.32.

The measured reflection signals are compared with simulated results. The configuration for these simulations is given in Table 3.3 and Table 3.4 — which contain the parameters of the used materials. The result of this comparison is given in Figure 3.33.

It can be observed that there is a good match between the simulated reflection response and the measured signal. Differences between the simulated and measured signal can be due to errors in the developed model and to incorrect product specifications (layer thickness, density and velocity) by the manufacturer.

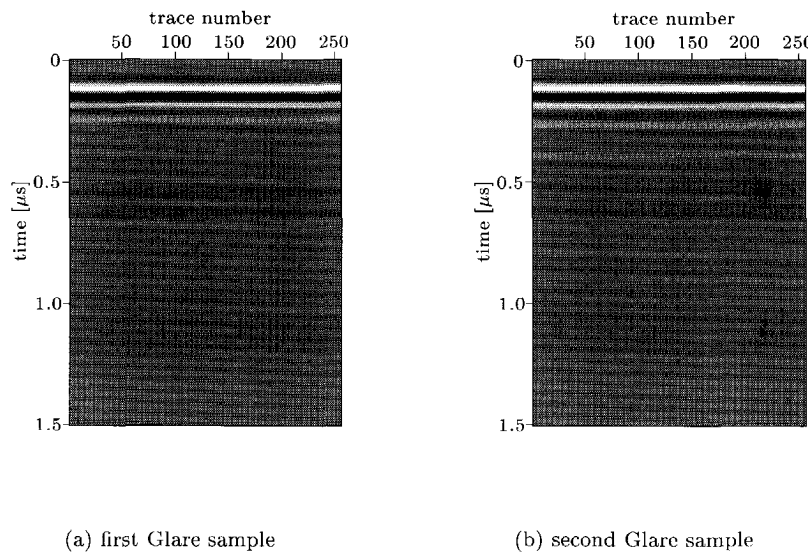
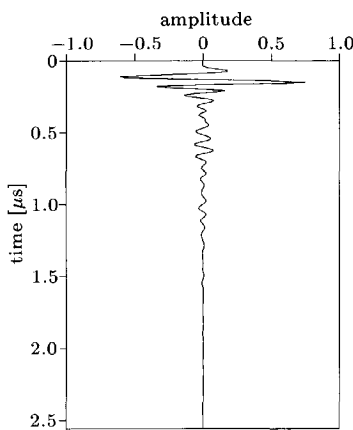
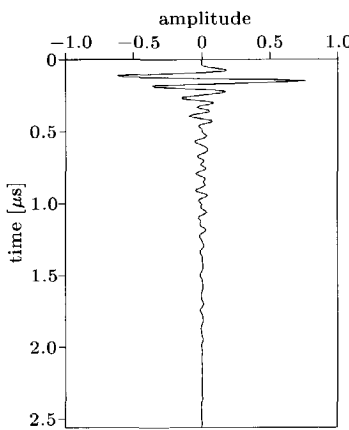


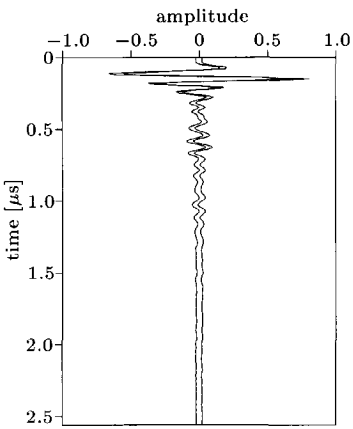
Fig. 3.31 Reflection measurements on two Glare samples, after aligning the traces to each other. The configurations of the samples are given in Table 3.3 and Table 3.4.



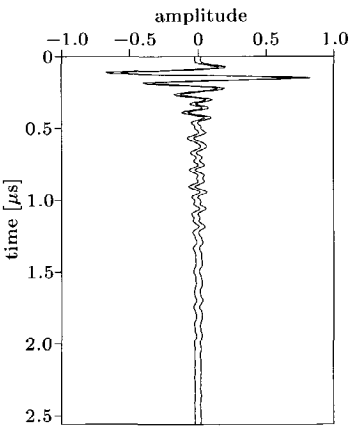
(a) stacked time-signal Glare of the first Glare 2/1 sample



(b) stacked time-signal Glare of the second Glare 2/1 sample

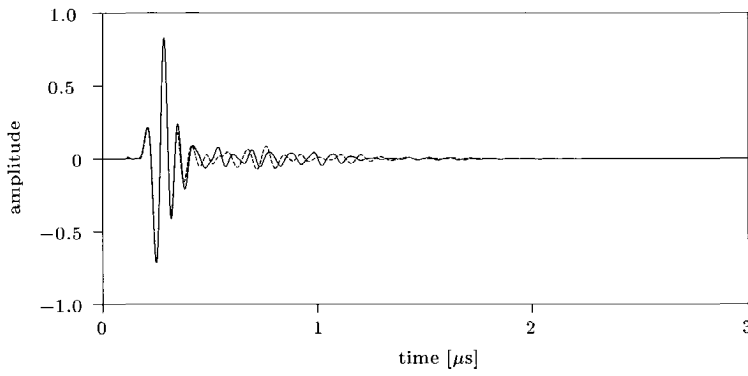


(c) 99% probability interval of the first Glare 2/1 sample

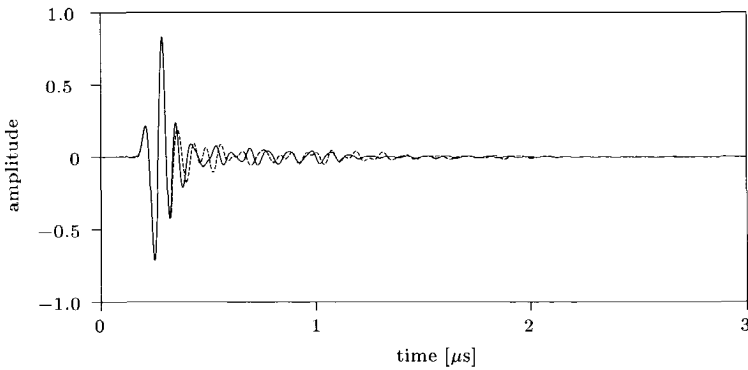


(d) 99% probability interval of the second Glare 2/1 sample

Fig. 3.32 Reflection measurements on two Glare samples according to the configurations of Table 3.3 and Table 3.4; 256 traces are aligned and stacked. (a) and (b) show the time-averaged values, (c) and (d) show the 99% probability interval.



(a) first Glare 2/1 sample



(b) second Glare 2/1 sample

Fig. 3.33 Comparison between simulated reflection response (solid line) and measured reflection response (dotted line) on two Glare 2/1 samples.

Chapter 4

Recursive Direct Inversion

In Chapter 2, a description of the acoustic wavefield as a function of the material parameters of a horizontally layered target has been derived. In most practical problems, the wavefield — the acoustic pressure or velocity — is the measured quantity and the material parameters have to be derived. In this chapter, the first of two methods is described that will yield the acoustic parameters of the material, based on the measured wavefield. The method described here is based on direct inversion of the equations in Chapter 2.

4.1 Inversion parameters and acoustic parameters

The forward algorithm developed in Chapter 2 makes use of the knowledge of the traveltimes in each layer and the reflection coefficient at each interface. Therefore, each inversion algorithm that is based on this forward algorithm will result in an estimation of the traveltimes and reflection coefficients.

In practice, one is often interested in parameters that are more directly related to the material. The traveltimes and reflection coefficients contain information about the material parameters, and a conversion can be applied in order to obtain the desired material parameters.

Four interesting parameters of layer i are the depth Δz_i , the density ρ_i , the acoustic velocity c_i and the specific acoustic impedance Z_i . Relationships between these parameters and the traveltimes and reflection coefficients are given by the following

equations:

$$Z_{i+1} = Z_i \frac{1 + R_i}{1 - R_i} \quad (4.1)$$

$$\Delta z_i = c_i t_i \quad (4.2)$$

$$c_i = \frac{\Delta z_i}{t_i} \quad (4.3)$$

$$\rho_i = \frac{Z_i}{c_i}. \quad (4.4)$$

Any of these equations can be used, depending on the application and the a-priori knowledge. For example, if the acoustic velocity of a layer is well-known a priori, Equation (4.2) can be used in order to estimate the layer thickness.

On the other hand, if the layer thickness is assumed to be well-known, the acoustic velocity is obtained using Equation (4.3). The specific acoustic impedance is given by Equation (4.1), and Equation (4.4) can be used to obtain the density.

4.2 Inverse theory

The forward algorithm is constructed in a recursive way, by adding the influence of a layer in each recursion step. For convenience, the construction steps are repeated here ¹.

The algorithm is initiated by the expression for the interface-free pressure at the top of layer n — the lower-most layer. In the frequency domain, this expression is given by Equation (2.163) ²:

$$P_n^0 = W_n R_n W_n S. \quad (4.5)$$

The frequency representations of the total scattered pressure at this point, and of the interface-free pressure at the top of the next layer are obtained by the recursive steps:

$$P_i = \frac{P_i^0 S}{S + R_{i-1} P_i^0}, \quad (4.6)$$

$$P_{i-1}^0 = W_{i-1} (R_{i-1} S + (1 - R_{i-1}^2) P_i) W_{i-1}. \quad (4.7)$$

It follows from this algorithm that in each step — obtaining an expression for P_{i-1}^0 based on an expression for P_i^0 — use is made of a frequency dependent scalar $W_{i-1}(\omega)$ — the propagation term — and a scalar R_{i-1} — the reflection coefficient. This

¹The explanation of the used symbols can be found in Chapter 2.

²For simplicity, the frequency-dependence is not explicitly written in the following equations. The reader has to keep in mind that P_i , P_i^0 , W and S are dependent on the angular frequency ω . If one of the media at interface i shows relaxation phenomena, also R_i is frequency-dependent.

reflection coefficient is a real-valued frequency independent scalar in the case the corresponding interface is located between two instantaneously reacting media. If one of the media shows relaxation phenomena, however, R_i is complex valued and frequency dependent. It was shown theoretically in Section 2.4 and with a numerical example in Subsection 2.6.2 that for the configurations discussed in this research, R_i can be approximated by a real frequency-independent scalar.

The propagation term W_{i-1} is, by means of Equation (2.79) directly related to the scalar Δz_{i-1} — the thickness of layer $i - 1$. As a consequence, two scalars that are related with the added layer and layer-interface are introduced in each step. In the inverse algorithm, these two scalars are obtained in each step.

The inverse expressions for Equations (4.6) and (4.7) are given by

$$P_i = \frac{P_{i-1}^0 - W_{i-1}R_{i-1}W_{i-1}S}{W_{i-1}(1 - R_{i-1}^2)W_{i-1}}, \quad (4.8)$$

$$P_i^0 = \frac{P_iS}{S - P_iR_{i-1}}. \quad (4.9)$$

Equations (4.8) and (4.9) give an expression for obtaining the interface-free pressure P_i^0 at the top of layer i as a function of the interface-free pressure P_{i-1}^0 at the top of layer $i - 1$.

Equation (4.8) has to be interpreted as follows: the acoustic pressure P_i at interface i is obtained from the pressure P_{i-1}^0 just below interface $i - 1$ by

- subtracting the primary arrival from the pressure measured at interface $i - 1$ — by means of the term $W_{i-1}R_{i-1}W_{i-1}S$.
- correcting for propagation effects — twice W_{i-1} in the denominator — and transmission effects — by means of $(1 - R_{i-1}^2)$.

In Equation (4.9), the multiples related to interface z_i are eliminated from the pressure P_i , resulting in the interface-free pressure P_i^0 .

The right-hand sides of Equations (4.8) and (4.9) have to be evaluated for a number of angular frequencies ω . It follows from the equations that these evaluations can be done separately — the value of $P_i^0(\omega_A)$ does not influence the value of $P_i^0(\omega_B)$ when $\omega_B \neq \omega_A$.

The algorithm is initiated by posing

$$P_0^0(\omega) = P_0(\omega), \quad (4.10)$$

which is in agreement with the assumption made in the previous chapter — the distance between transducer and material is large enough so no water layer-related multiples will occur during the considered time frame.

4.3 Obtaining the wavefield parameters

Ultimately, one is interested in the material parameters of the constituting layers. Unfortunately, these parameters are not measured directly by acoustic measurements. It is possible, however, to retrieve the acoustic parameters from the measurements. These acoustic parameters can then be translated into material parameters.

As mentioned in the previous section, each recursion step requires one frequency dependent scalar — $W_{i-1}(\omega_j)$ — and one scalar — R_{i-1} — to be known.

The scalar $W_{i-1}(\omega_j)$ is obtained by a discretization of the function $W_{i-1}(\omega)$, which is in the case of propagation in an instantaneously reacting medium defined as — see Equation (2.79)

$$W_{i-1}(\omega) = \exp(-j\omega t_{i-1}) \quad (4.11)$$

with $t_{i-1} = \Delta z_{i-1}/c_{i-1}$ the one-way traveltime in the considered layer.

It follows that the scalars $W_{i-1}(\omega_j)$ can be reconstructed once the traveltime in layer i is known.

According to Equation (2.128), the propagation factor in a medium with relaxation is given by

$$W_{i-1}(\omega) = \exp(-j\omega t_{i-1}) \exp(-\gamma_r \Delta z_{i-1}). \quad (4.12)$$

As a consequence, also the attenuation coefficient γ_r and the layer thickness Δz_{i-1} need to be known.

From Equation (4.8) it follows that the total pressure at the top of layer i can now be calculated, provided that also the source signal $S(\omega)$ is known³.

In the following discussion, it is assumed that this is the case.

Assumption 5: Repeatability of source

■ The source-signal is well-known.

This Assumption is satisfied when the source signal is highly repeatable. The source signal can then be obtained as explained in Section 3.4.

There are two reasons for obtaining the traveltimes in the constituting layers from the measured wavefield:

- the traveltime is necessary for the application of Equation (4.8);

³In practice, the source signal is obtained as a time series $s(t)$, and a Fourier transformation has to be applied to this series in order to obtain the frequency representation $S(\omega)$.

- the traveltime in a layer is related to the material parameters of that layer.

At this point, two cases will be considered. First, the ideal case where the primary arrival is completely separated from other arrivals is studied. After that, attention is paid to the case where later arrivals interfere with the primary arrival.

4.3.1 Separated arrivals

In Figure 4.1, the simulated result of a reflection measurement on an aluminium disk with a thickness of 2 mm is shown. The distance between transducer and target is 0.1 mm and the aluminium disk is embedded in water. Abstraction is made of the impedance contrast between the transducer and water and as a consequence, no water-layer related multiples will occur⁴. The material parameters of this configuration are given in Table 4.1

Aluminium layer in water						
Layer	material	Δz (mm)	ρ (kg/m ³)	c (m/s)	R	t (s)
0	water	0.1	1000	1480	0.842	6.757×10^{-8}
1	aluminium	2	2740	6300	-0.842	3.175×10^{-7}
2	water	∞	1000	1480	-	-

Table 4.1 Material properties for an aluminium disk embedded in water.

The source signal is emitted by a transducer with a centre frequency of 15 MHz and a focus point at 76.2 mm.

The first arrival — due to a reflection at the top interface — is clearly separated from the second arrival — due to a reflection at the bottom interface — and the multiple arrivals.

Three methods will be described now for obtaining the desired parameters — the traveltime in the layers and the reflection coefficient at the interfaces between the layers. In order to compare the different methods, only the traveltime in the water layer and the first reflection coefficient will be retrieved. A complete inversion is given in the subsequent sections.

Using the above mentioned configuration, the true one-way traveltime in the water layer is 6.757×10^{-8} s while the true reflection coefficient at the interface between water and aluminium is 0.8421.

⁴The water-layer related multiples are excluded in this simulation, since they will not show up in the recorded time-frame in actual measurements due to the large distance between transducer and target.

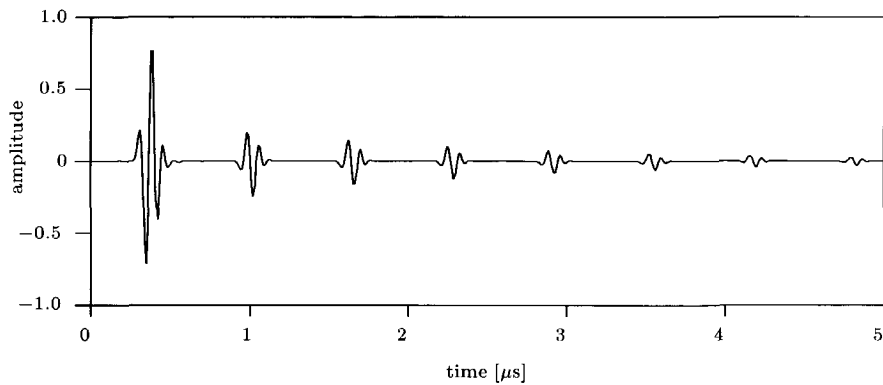


Fig. 4.1 Simulation of the reflection response of an aluminium disk with a thickness of 2 mm.

Absolute maximum

Since the first reflection in the response occurs after the wave travelled towards the target and back to the transducer, the difference in position between a fixed point in the source signal — which is determined in advance — and the corresponding point in the response is then the two-way travel time. In this first approach, the positions of the maximum values occurring in the source signal and the reflection response are compared. A closer view of the neighbourhood of the maximum values is given in Figure 4.2.

The maximum value in the source signal occurs at sample 26 ($t = 25 \times 10^{-8}$ s) while the reflection response reaches its highest value at sample 40 ($t = 39 \times 10^{-8}$ s). Since the sampling rate amounts 100 MHz, the obtained one way traveltimes in the water layer between the transducer and aluminium using this method is 7×10^{-8} s.

The estimated reflection coefficient is obtained by dividing the maximum value in the trace by the maximum value in the source signal, yielding 0.767.

Cubic interpolation

It is very unlikely that the maximum value in the analog signal — before sampling and digitising — occurs at the position of a sample. From Figure 4.2(b), it is clear that the maximum value in the trace occurs between samples 39 ($t = 38 \times 10^{-8}$ s) and 40 ($t = 39 \times 10^{-8}$ s).

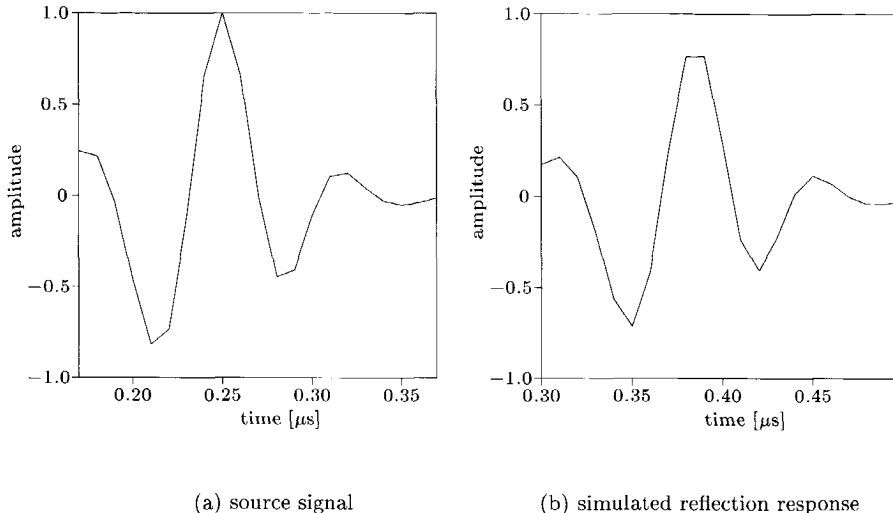


Fig. 4.2 Detailed look at the maximum values in the source signal and in the simulated reflection response of an aluminium disk embedded in water.

The cubic interpolation method aims to reconstruct the signal in the neighbourhood of the maximum by performing a second-order polynomial interpolation. This method will give better results when the actual signal behaves like a second-order polynomial in the neighbourhood of the maximum⁵. A second-order polynomial requires three known sample points. The sample point where the maximum occurs and its two adjacent points are used for this.

In Figure 4.3, the result of a second-order polynomial interpolation is compared with a linear interpolation of the response. It is clear that the maximum after cubic interpolation is at a different position and has a different value than the maximum occurring at a sample. Using this method, the estimated traveltime in the water layer is 6.76×10^{-8} s and the reflection coefficient is 0.827.

⁵ Although the source wavelet is not a second order polynomial, it follows from the measurements in Chapter 3 that it is reasonable to approximate the source signal in the neighbourhood of the maximum value with a second-order polynomial.

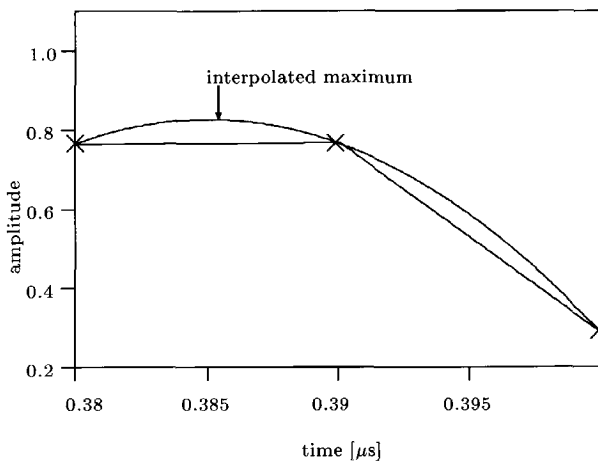


Fig. 4.3 Comparison between the signal with linear and cubic interpolation

Sinc interpolation

The method of the cubic interpolation assumes that the signal has a parabolic shape in the neighbourhood of the maximum. Also, the method only uses information from 3 sample points — the point where the maximum occurs and the two adjacent points.

A band-limited signal can be exactly and uniquely reconstructed if the Nyquist Frequency — half the sampling frequency — is larger or equal to the upper boundary of the frequency band of the signal. A smaller sample distance can be obtained by expanding the frequency spectrum with zeros — which is allowed as the signal has no frequency content at those frequencies. Since $\Delta t = \frac{1}{F_s}$ with F_s the sampling frequency, the sample-distance can be as low as wanted.

Using Shannon's sampling theorem⁶ it is possible to reconstruct the exact value at a given point, since

$$p(t) = \sum_{i=-\infty}^{\infty} p(i\Delta t)h_s(t - i\Delta t), \quad (4.13)$$

with

$$h_s(t) = \text{sinc}(F_s t) = \frac{\sin(\pi F_s t)}{\pi F_s t}. \quad (4.14)$$

The sinc function is shown in Figure 4.4.

Note that this method can only yield an exact solution if the trace is infinitely long. However, since $\text{sinc}(\tau) \leq \frac{1}{\pi\tau}$, the contribution from samples that are far away from

⁶A formulation and proof can be found in Körner (1993).

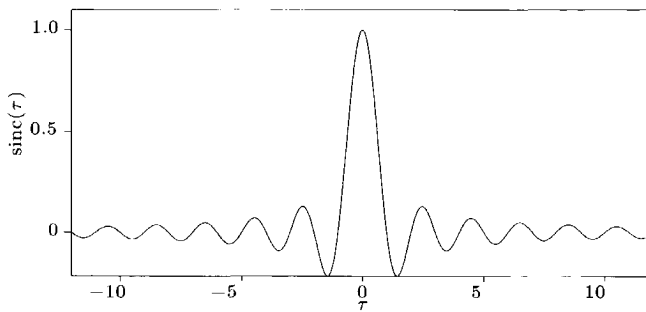


Fig. 4.4 Sinc function around $\tau = 0$.

the considered point will be small compared with the contributions from points in the neighbourhood *unless* the signal has a much higher value at the points far away.

In practice, Equation (4.13) will be approximated by

$$p(t) = \sum_{i=c-n}^{c+n} p(i\Delta t)h_s(t - i\Delta t) \quad (4.15)$$

where c is the nearest sample point in the neighbourhood of t and n is half the number of sample points that will be used in the approximation. It is clear that the more points are used, the better the approximation will be.

In Figure 4.5, two sinc-interpolation methods with a different number of sample-contributions are compared against the "exact" signal — which is obtained by resampling the signal by adding zeroes in the frequency domain beyond the Nyquist frequency. It is clear that using a sinc-interpolation method with a high number of evaluation-points results in a better approximation than a linear interpolation. When "enough" points are used for the sinc-evaluation, the resulting signal coincides with the "exact" signal.

Equation (4.15) gives the value of the signal at one specified point. A root-detection method must be used to yield the t -value which has the maximum signal-value. As a result of the combination of the sinc-method and the root-detection method, two accuracy-parameters have to be supplied: the number of samples used in the sinc-approximation and the accuracy with which the position of the maximum has to be known. These two parameters can be chosen independently from each other. However, a position-accuracy parameter of ϵ_τ does not guarantee that the distance between the calculated position and the position of the *real* maximum will be at most ϵ_τ . It only guarantees that the distance between the calculated position and the real maximum in the *sinc-interpolated* signal will be at most ϵ_τ .

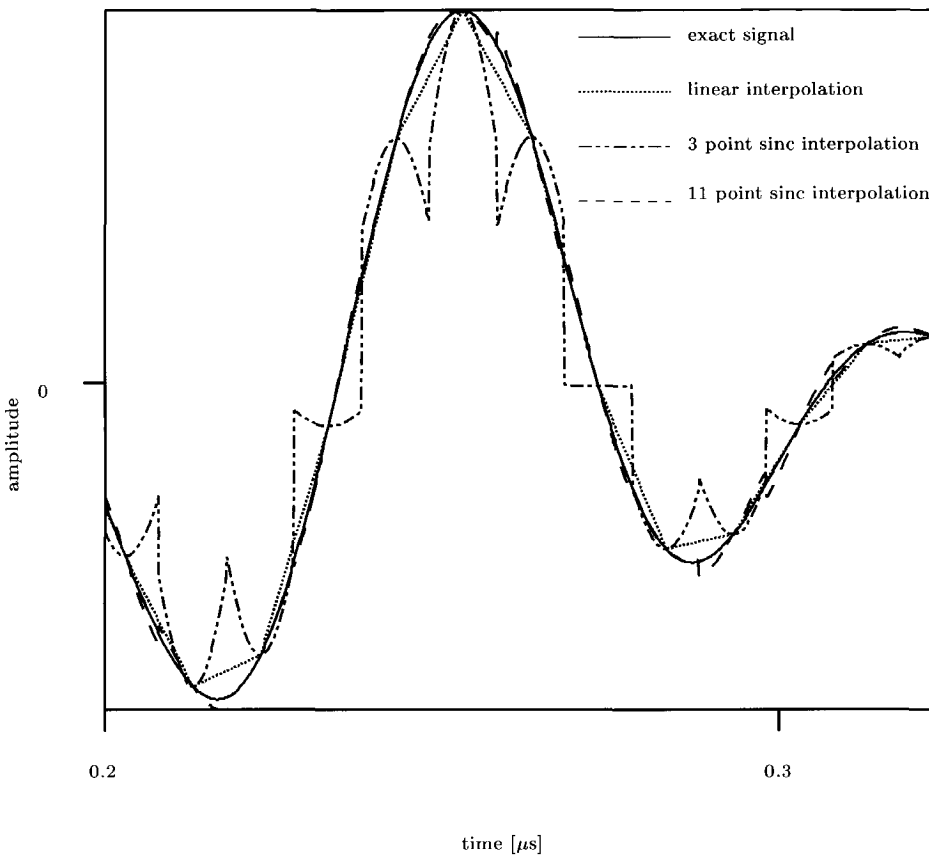


Fig. 4.5 Comparison between the exact signal and interpolated versions using a linear interpolation and two sinc-interpolations with 3 and 11 points.

In Figure 4.6, the influence of the number of samples used for the sinc-approximation is shown. For the configuration described in the beginning of this section, both the traveltime in the water layer and the reflection coefficient between the water layer and the aluminium disk are calculated with a position accuracy of 0.001 sample.

Comparison

The parameters returned by the different methods are compared with each other and with the exact parameters in Table 4.2. As expected, the sinc interpolation method uses more information and therefore gives better results — especially when

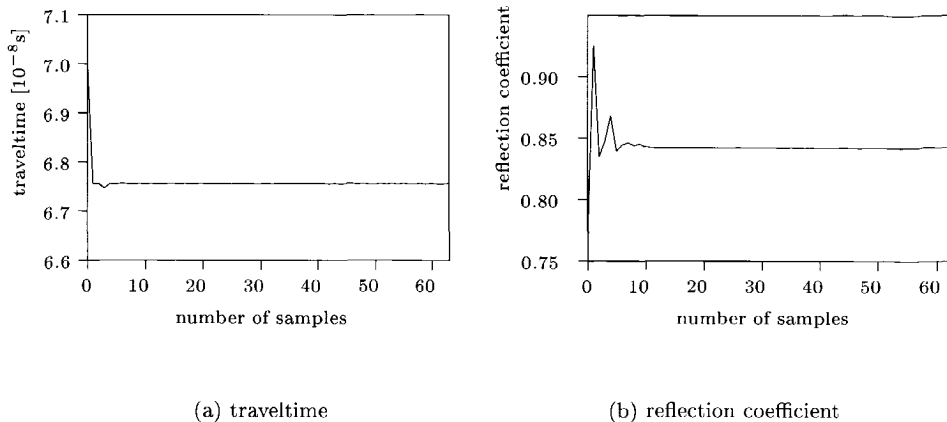


Fig. 4.6 Influence of the number of samples used in sinc-interpolation on the acquired material parameters.

Comparison of peak detection methods		
Method	t_0 (s)	R_0
exact	6.757×10^{-8}	0.8421
sample maximum	7×10^{-8}	0.7674
cubic interpolation	6.76×10^{-8}	0.8266
sinc interpolation 7 points	6.747×10^{-8}	0.8476
sinc interpolation 37 points	6.756×10^{-8}	0.8422

Table 4.2 Material parameters obtained by different peak detection methods.

more sample points are used.

It has to be taken into account though that the values in this table are only valid for one specific configuration. Even the method using the maximum sample can give correct results in the case the maximum occurs at a sample point.

4.3.2 Interfering arrivals

In the previous case, where all arrivals were completely separated from each other, it is guaranteed that the — interpolated — maximum value in a trace is the product of the maximum value in the source signal and the first reflection coefficient. This

no longer holds when a second event — be it a primary arrival from a second layer or a multiple reflection in the first layer — arrives before the first event has been completely detected.

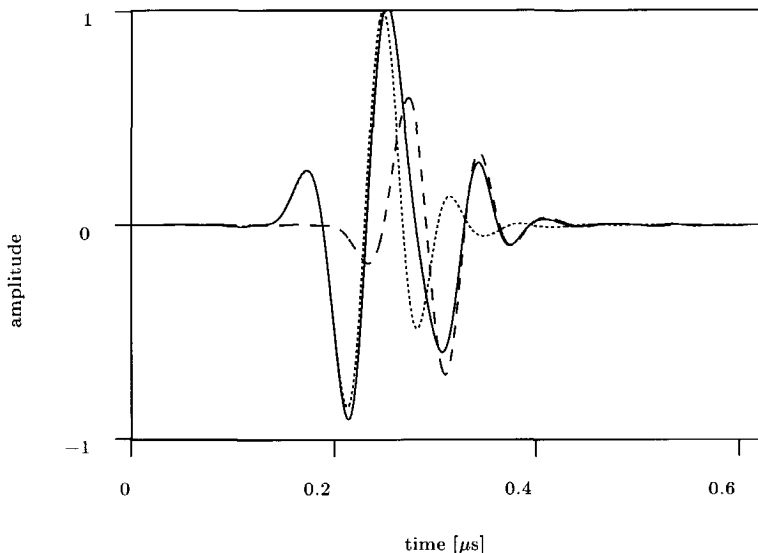


Fig. 4.7 Interference of the first (dotted line) and the second (dashed line) arrival. The superposition of these arrivals is shown with a solid line.

Figure 4.7 shows what happens when a second event interferes with the first arrival. The position and the value of the maximum are altered. This has serious consequences for the peak-detection. The methods described in the previous subsection will reveal the maximum that is the result of the superposition of the first and the second arrivals. The inversion method, however, is based on the maximum in the first arrival and will therefore yield incorrect results.

Whether the different arrivals interfere with each other or not depends on the configuration — the thickness and velocity of the layers — and on the length of the source wavelet. In order to avoid interference, the wavelet has to be as short as possible — with the delta pulse as the limiting case. Since in practice all wavelets are band-limited in the frequency domain, they all have a certain time length. It is possible however to change the length and shape of a wavelet by altering its frequency spectrum — by means of amplitude and phase modifications.

The frequency content of a signal consists of two properties for each frequency com-

ponent: the amplitude and the phase. The amplitude is a measure for the energy in this frequency component. Altering the amplitude therefore means altering the energy-content of the signal. Changing the phase-component, on the contrary, only changes the shape of the wavelet without changing the energy-content.

In many seismic applications, it is desirable to have a short wavelet, since this increases the resolution of the images.

More important than the length of the wavelet is the position of the peak. Indeed, the position and value of the peak will be used to obtain the material parameters of the considered layer, and to eliminate the effects of this layer in the wavefield. The wavelets in Figure 4.8 have the same power spectrum but a different phase spectrum. The maximum value in wavelet (a) occurs after 19.0×10^{-8} s, while the maximum

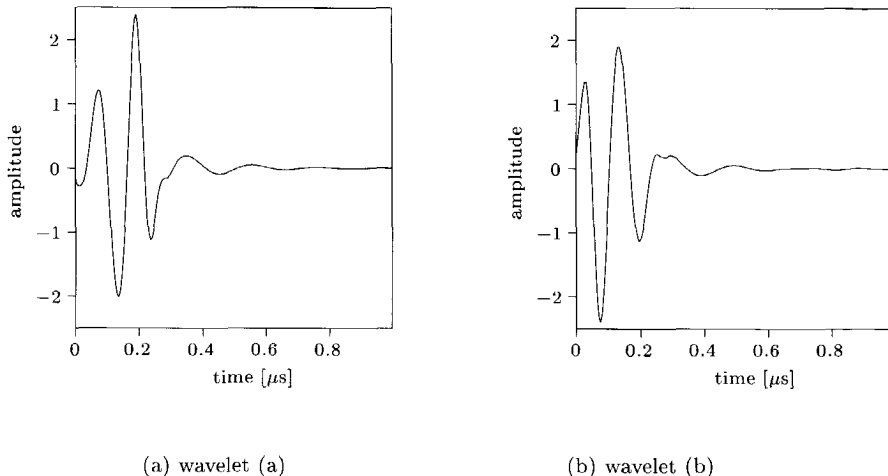


Fig. 4.8 Two wavelets with the same power spectrum but a different phase spectrum. The peak occurs at different positions and has a different value.

value in wavelet (b) is reached after 7.5×10^{-8} s. Consequently, when the two-way traveltime in a layer is less than 19.0×10^{-8} s respectively 7.5×10^{-8} s, the maximum in the reflection at the top of the layer will not be reached before the reflection at the bottom of the layer arrives.

In Figure 4.9, the simulated result of a reflection measurement on an aluminium disk with a variable thickness embedded in water is shown. The thickness varies from 0.05 mm on the left side to 1.6 mm on the right side⁷. Above the disk is

⁷Although the pictures show a linear increase in the thickness, it is assumed that the thickness

a water layer with a thickness of 0.8 mm. No water-layer related multiples are taken into account. The two wavelets from Figure 4.8 are used for performing 32 simulations, where the horizontal spacing between two simulations amounts 0.2 mm.

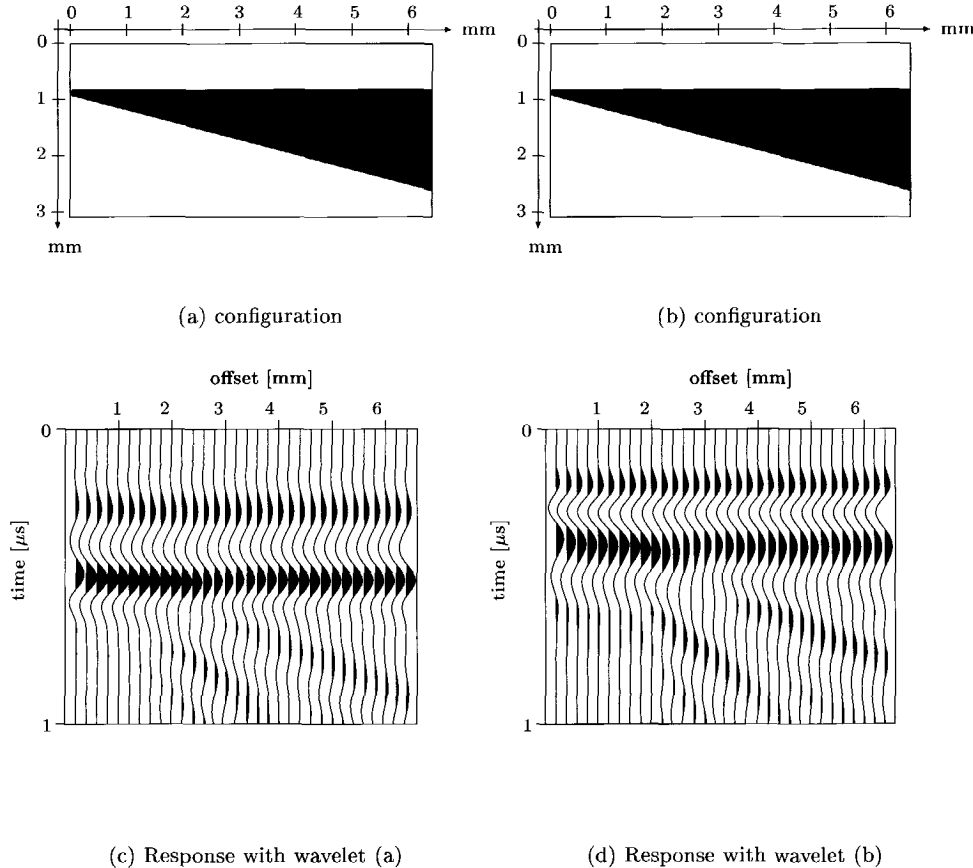


Fig. 4.9 Simulated reflection measurements on an aluminium disk with a variable thickness using the two wavelets of Figure 4.8.

For both situations, the reflection coefficient and the traveltime in water are obtained using a 12 point sinc peak-detection method. The results are shown in Figure 4.10.

varies stepwise. This is a requirement, since the forward model assumes that the incident wavefield has to propagate perpendicular to the interface orientation.

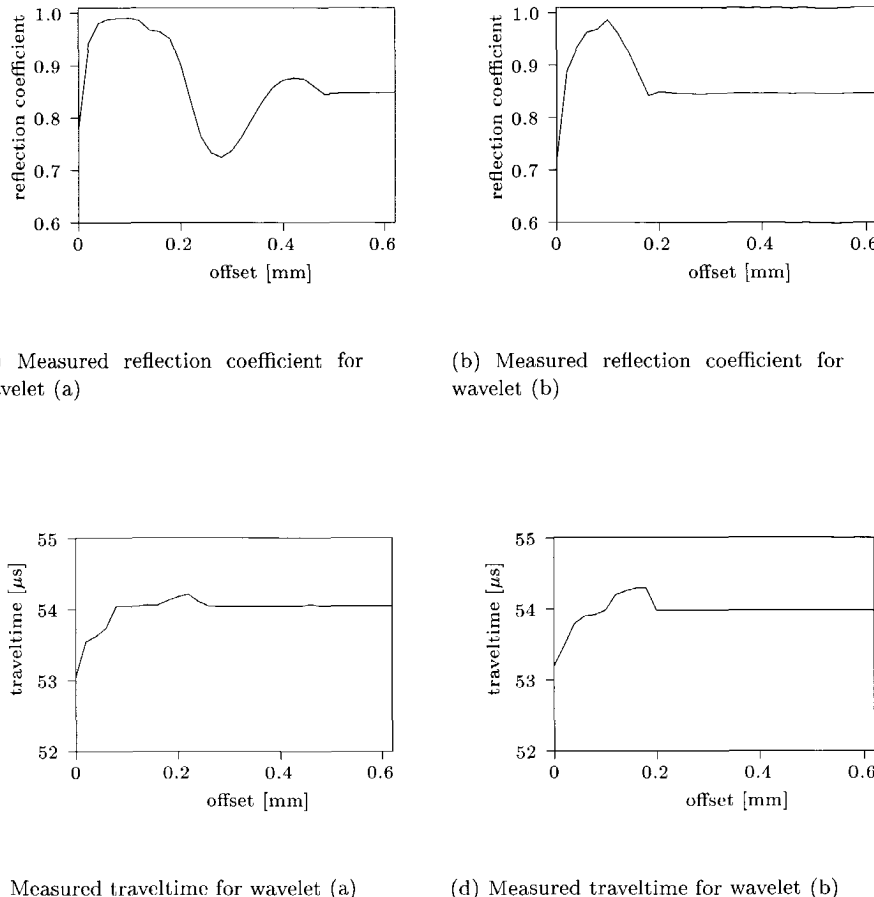


Fig. 4.10 Extracted reflection coefficients and traveltimes from simulated responses on aluminium disks with variable thickness (see Figure 4.9).

It is clear that using wavelet (b), better results will be obtained for thin layers. The difference between the two wavelets is that the energy in wavelet (a) is concentrated at the end of the wavelet, while wavelet (b) has its energy in the beginning. Although the position of the maximum is not only dependent on the energy distribution in the wavelet, it is clear that the more the energy is concentrated in the beginning of the wavelet, the more likely the maximum value will occur in the beginning too.

minimum phase wavelets

According to Yilmaz (1987), a wavelet with a given amplitude spectrum is called a minimum phase wavelet if its energy is maximally concentrated at its onset. The concept of minimum phase wavelets is studied in the Laplace-domain by Claerbout (1976) and by Berkhouit (1973) in the Fourier-domain. There are different ways to transform a wavelet into a minimum phase wavelet. One method is the Whittle's Exp-Log method (Claerbout, 1976), which can be easily transformed into an algorithm. The filter $T(\omega)$ ⁸ that is used for transforming a wavelet into its minimum phase equivalent has to be applied to the reflection measurement where the considered wavelet serves as a source signal. The transformation from the wavelet $S(\omega)$ into the minimum phase wavelet $S^{\min}(\omega)$ is given by

$$S^{\min}(\omega) = T(\omega)S(\omega). \quad (4.16)$$

The measured pressure in a reflection measurement, according to Equation (2.162) and given a minimum phase wavelet $S^{\min}(\omega)$, is given by

$$P^{\min}(\omega) = X(\omega)S^{\min}(\omega) \quad (4.17)$$

and thus

$$P^{\min}(\omega) = T(\omega)P(\omega). \quad (4.18)$$

The preprocessing procedures mentioned in the beginning of this chapter can thus be applied to the transformed signal $P^{\min}(\omega)$, when use is made of the minimum phase wavelet $S^{\min}(\omega)$.

4.4 Inversion algorithm

An algorithm for the detection of the traveltimes t_i of the different layers and the reflection coefficients R_i of the different interfaces based on recursive inversion can now be given by

*determine the minimum phase equivalent of the source signal
 call the sampled reflection signal p_0^0
 apply minimum phase deconvolution of signal p_0^0
 for i from 0 to n
 begin
 use a peak-detection method to estimate R_i and t_i from the signal in p_i^0
 calculate frequency domain counterpart $P_i^0(\omega)$ from $p_i^0(t)$
 for j from 0 to m*

⁸A discussion of $T(\omega)$ is beyond the scope of this thesis.

```

begin
  calculate  $W_i(\omega_j)$  based on  $t_i$ 
  use Equation (4.8) to calculate  $P_{i+1}(\omega_j)$  which means:
    - subtract the primary reflection
    - correct for transmission effects
    - correct for propagation effects
  use Equation (4.9) to calculate  $P_{i+1}^0(\omega_j)$  which means:
    - remove the multiples related to interface  $i$ 
end
  calculate time counterpart  $p_{i+1}^0(t)$  from  $P_{i+1}^0(\omega)$ 
end

```

In this algorithm, n is the number of layers in the configurations and m is the number of frequencies in one measurement.

Based on this algorithm, a flow chart is constructed and given in Figure 4.11.

4.5 Inversion on simulated data

In this section, the Recursive Direct Inversion (RDI) algorithm developed in Section 4.4 will be tested on simulated measurements. The simulations are obtained using the forward algorithm developed in Section 2.5.

Since the Recursive Direct Inversion algorithm is a mathematical and unique inversion of the forward algorithm, the parameters obtained by the inversion algorithm should match the parameters used in the forward model, provided that all calculations are performed without introducing errors.

Obviously, this is not the case. First of all, there are computational errors due to rounding errors. Also, the result of a simulation is not a continuous signal, but a *discretization* of a signal. As a consequence, there will be discretization errors in the result. By using techniques as cubic interpolation or sinc interpolation for the detection of the peak, the effect of discretization is diminished, but it can not be completely eliminated.

Further, the recursive nature of the inversion process — where the effects of one layer at the same time — is disturbed when primary arrivals interfere with later arrivals. The minimum-phase transformation of the source signal is used to reduce this effect.

Errors will propagate through the algorithm. As a consequence, the material parameters of the bottom layer will be obtained with less accuracy than the parameters of the top layer. This is an important issue one has to consider in order to choose a suited inversion method.

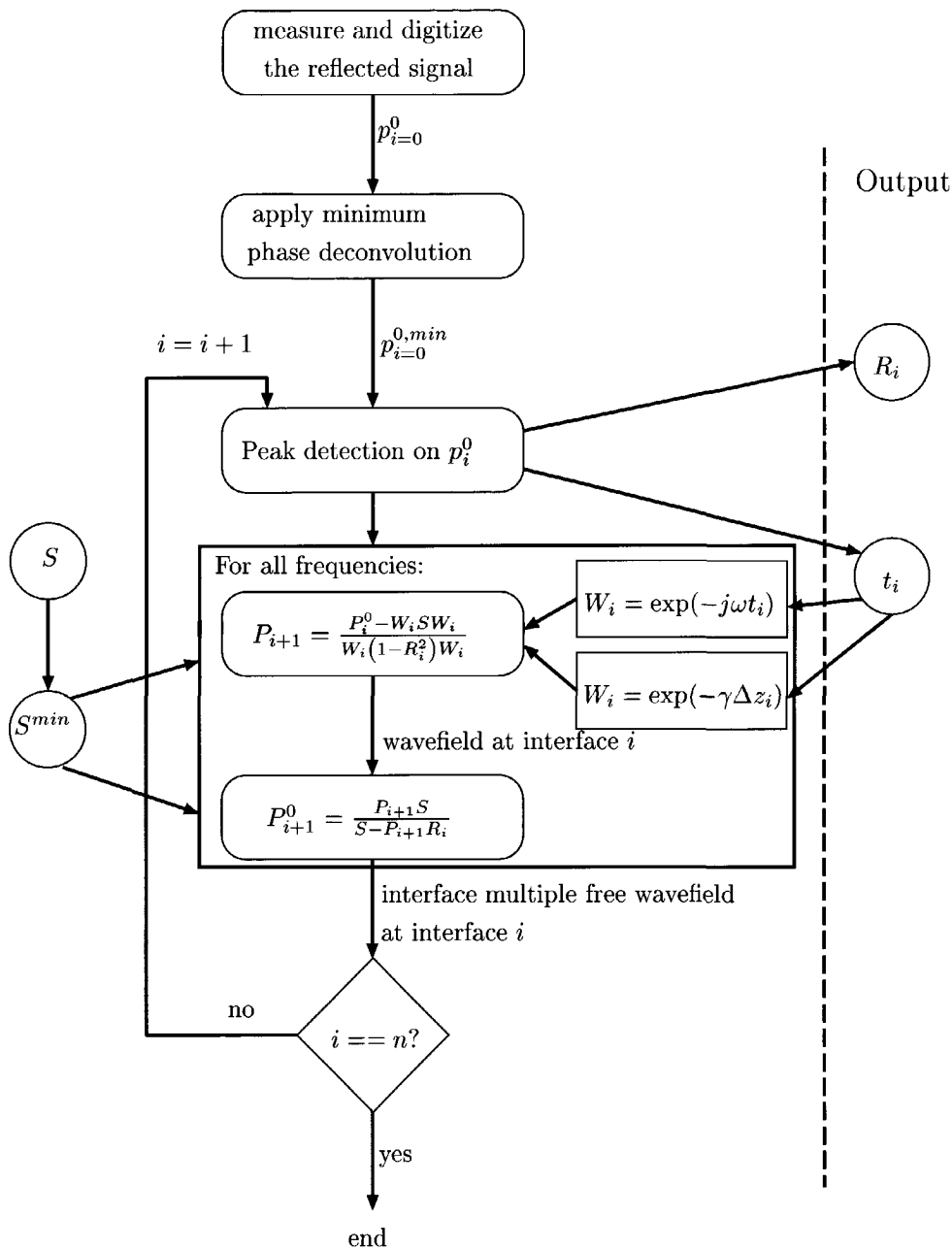


Fig. 4.11 Flow chart for the proposed inversion algorithm based on recursively obtaining the information about one layer.

The Recursive Direct Inversion algorithm is first tested against simulations, in order to check the theoretical possibilities of the algorithm. Computational and discretization errors are also present in real measurements — among other types of errors — and this section therefore gives an example of the *upper limit* of the accuracy of the Recursive Direct Inversion algorithm.

4.5.1 Aluminium layer

In chapter 2, a simulated example of a reflection measurement on a homogeneous aluminium layer was shown. A similar configuration is repeated in Table 4.3.⁹

Aluminium layer in water						
Layer	material	Δz (mm)	ρ (kg/m ³)	c (m/s)	R	t (s)
0	water	0.1	1000	1480	0.842	6.756×10^{-8}
1	aluminium	0.5	2740	6300	-0.842	7.936×10^{-8}
2	water	∞	1000	1480	-	-

Table 4.3 Material properties for an aluminium disk embedded in water.

The source signal that is used for this simulation — emitted by a 15MHz focussed transducer — is discussed in chapter 3. The source signal and the simulated acoustic response of the configuration are shown respectively in Figure 4.12(a) and Figure 4.12(b).

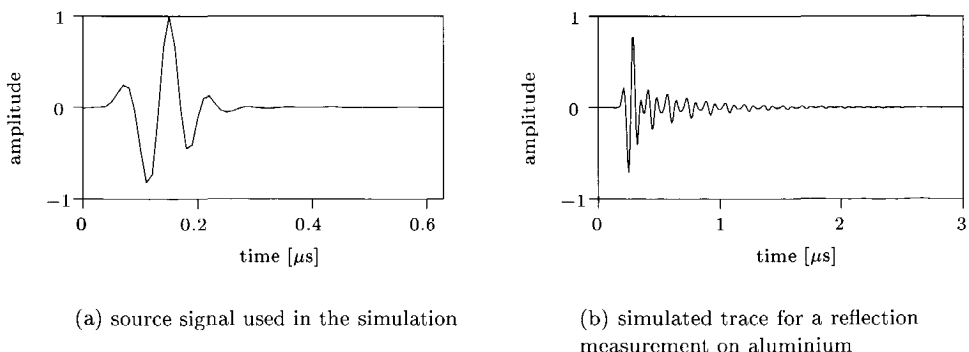


Fig. 4.12 Simulation of the acoustic reflection response of an aluminium disk embedded in water.

Before applying the Recursive Direct Inversion Algorithm, the source signal is trans-

⁹In practice, the water layer will be much thicker, since the target material has to be located in the focus zone of the transducer.

formed into its minimum-phase equivalent. The filter that is responsible for this transformation is then applied to the aluminium layer response, and the results are given in Figure 4.13.

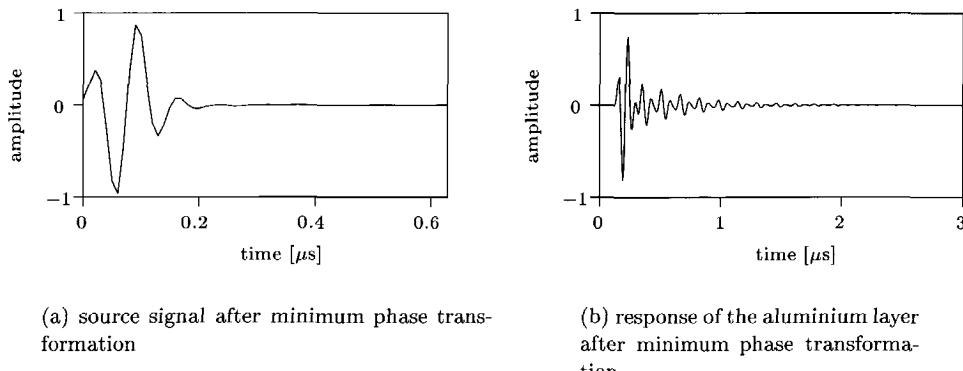


Fig. 4.13 Source signal and reflection response of the aluminium layer after minimum-phase transformation.

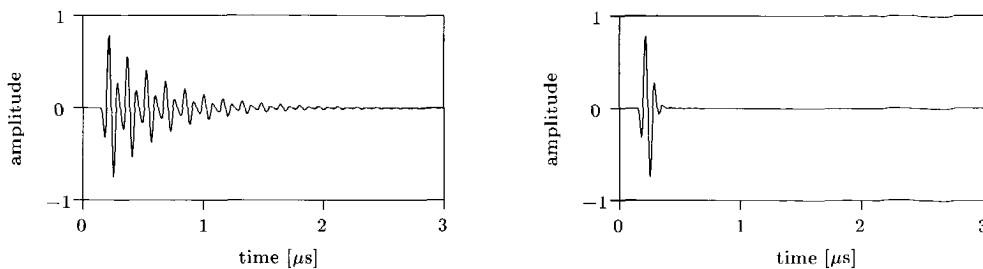
The first step of the Recursive Direct Inversion algorithm is to estimate the traveltime t_0 in *layer 0* — the water layer — and the reflection coefficient between *layer 0* and *layer 1* — the interface between water and aluminium. The obtained values, together with the "true" values, are given in Table 4.4.

Based on the estimated value of t_0 , the propagation factor W_0 can be obtained. Since water is assumed to be an instantaneously reacting medium, Equation (2.79) can be used for this.

After the calculation of the propagation factor, the acoustic pressure $P_1(\omega)$ and its time counterpart $p_1(t)$ can be calculated. The physical meaning of $p_1(t)$ represents the upgoing pressure that would be obtained if the top water layer was removed, and the transducer is positioned at the top of the aluminium layer. The calculation of p_1 based on p_0^0 therefore eliminates the effect of *layer 0*. The result of this elimination step is given in Figure 4.14(a).

The next step is to remove the multiple reflections related to the surface of the aluminium layer. This results in $p_1^0(t)$, which should be equivalent to the pressure that is measured when a transducer at the top of the aluminium layer only measures the upgoing wavefield, assuming no energy is reflected from the top of the layer back into the material. The resulting signal is given in Figure 4.14(b).

From this result, it is possible to determine the traveltime in the aluminium layer, and the reflection coefficient at the bottom interface of this layer. The results can be found in Table 4.4.



(a) Result after subtraction of the first layer reflection and correction for transmission effects for the water-aluminium interface

(b) Result after the elimination of the internal multiples in the aluminium layer

Fig. 4.14 RDI algorithm applied to a simulated reflection measurement of an aluminium layer.

Material parameters in aluminium layer configuration				
Layer	exact R	calculated R	exact $t[\text{s}]$	calculated $t[\text{s}]$
0	0.842	0.844	6.76×10^{-8}	6.76×10^{-8}
1	-0.842	-0.851	7.94×10^{-8}	7.94×10^{-8}

Table 4.4 Comparison between the material parameters used in the simulation and the parameters obtained by the Recursive Direct Inversion algorithm.

It appears that the traveltimes are obtained with a high accuracy. The reflection coefficients are also obtained with a good accuracy, but it can already be noticed that the reflection coefficients of lower interfaces — in this case R_1 — are less accurate than the reflection coefficients of the upper interfaces. The latter is a consequence of the error propagation.

4.5.2 Glare

As stated in the introduction of this section, it is expected that the quality of the result of the inversion decreases with increasing number of layers in the configuration. This will be tested in this subsection, by comparing the results of two different Glare-configurations, with respectively 3 and 5 layers.

The structural difference between Glare and aluminium is not only the number of layers, but also the presence of a medium with relaxation — prepreg — in Glare. In the following simulations, it is assumed that prepreg has an attenuation coefficient $\gamma_r = 1000 \text{ m}^{-1}$, and the coefficients of frictional force K and bulk inviscidness Γ have equal contributions to this attenuation coefficient — see Equation (2.123). In

the inversion, it will be assumed that γ_r is known.

Glare 2/1

The first configuration consists of three layers, and the material parameters are described in Table 4.5. The Glare 2/1 geometrical configuration is illustrated in

Glare 2/1 material embedded in water					
Layer	material	Δz (mm)	ρ ($\frac{\text{kg}}{\text{m}^3}$)	c ($\frac{\text{m}}{\text{s}}$)	γ_r ($\frac{1}{\text{m}}$)
0	water	0.1	1000	1480	0
1	aluminium	0.4	2740	6300	0
2	prepreg	0.250	1600	3100	1000
3	aluminium	0.4	2740	6300	0
4	water	∞	1000	1480	0

Table 4.5 Material parameters of a Glare 2/1 sample.

Figure 4.15(a). First, the source signal used to perform the simulation is emitted by a 15MHz focussed transducer. The result of this simulation is shown in Figure 4.15(b)

First, the source signal is transformed into its minimum phase wavelet, and the same transformation is applied to the reflection measurement. The result is given in Figure 4.16.

Since the configuration consists of three solid layers, three recursion steps are needed in order to obtain the acoustic parameters of the whole configuration. One elimination step removes the effect of the top-most layer. After the elimination of the first layer, the resulting signal has to be the same as the result of a simulation on a configuration of two layers. In Figures 4.17, 4.18 and 4.19 the elimination of the primary arrival and the multiples and the simulated trace are shown.

The true values are compared with the parameters obtained by the Recursive Direct Inversion algorithm, and given in Table 4.6.

The result of the Recursive Direct Inversion algorithm is a number of traveltime-reflection coefficients pairs. However, one is often interested in the acoustic impedance as a function of depth.

The traveltime-reflection pairs can be converted into a series of depth-impedance pairs, using Equations (4.1) and (4.2)¹⁰. In Figure 4.20(a), the acoustic impedance of the material is plotted as a function of the depth into the material, based on

¹⁰It is also possible to convert the traveltime-reflection pairs into depth-density pairs, provided that the velocities in the different layers are known. This is a fair assumption when well known materials are used.

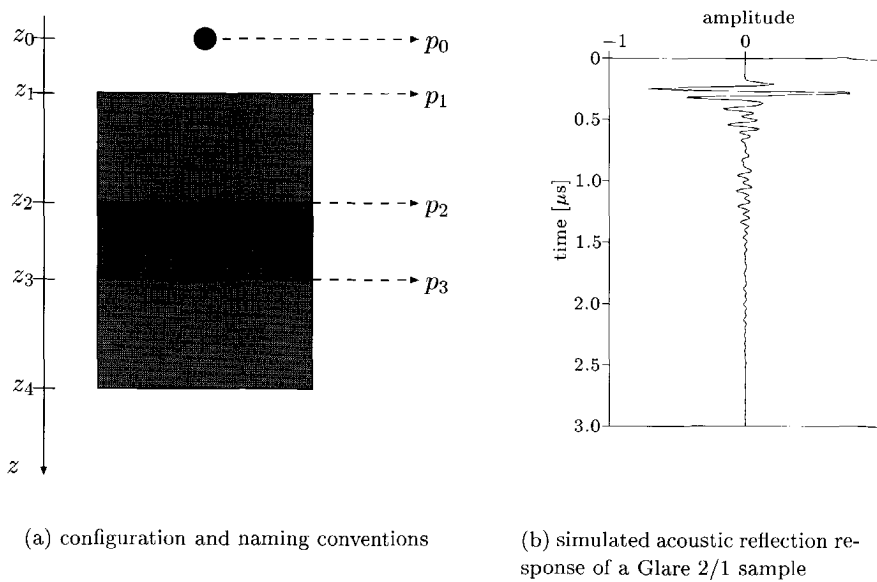


Fig. 4.15 Simulation of a reflection measurement on a Glare 2/1 material embedded in water.

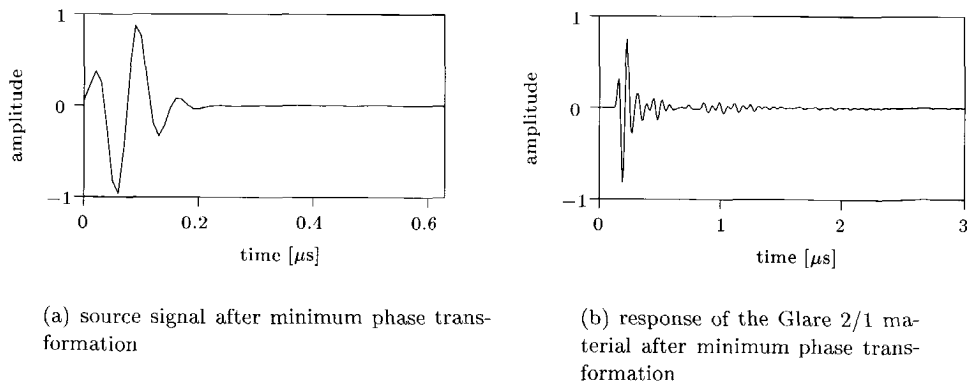


Fig. 4.16 Source and reflection response of the Glare 2/1 sample after performing a minimum-phase transformation.

the results given by the Recursive Direct Inversion algorithm. The parameters that are used for obtaining the simulated response are shown in a similar plot in Fig-

Material parameters in glare 2/1 configuration				
Layer	exact R	calculated R	exact $t[s]$	calculated $t[s]$
0	0.842	0.844	6.76×10^{-8}	6.77×10^{-8}
1	-0.554	-0.564	6.35×10^{-8}	6.36×10^{-8}
2	0.554	0.565	8.06×10^{-8}	8.07×10^{-8}
3	-0.842	-0.869	6.35×10^{-8}	6.37×10^{-8}

Table 4.6 Comparison between the material parameters used in the simulation and the parameters obtained by the Recursive Direct Inversion algorithm.

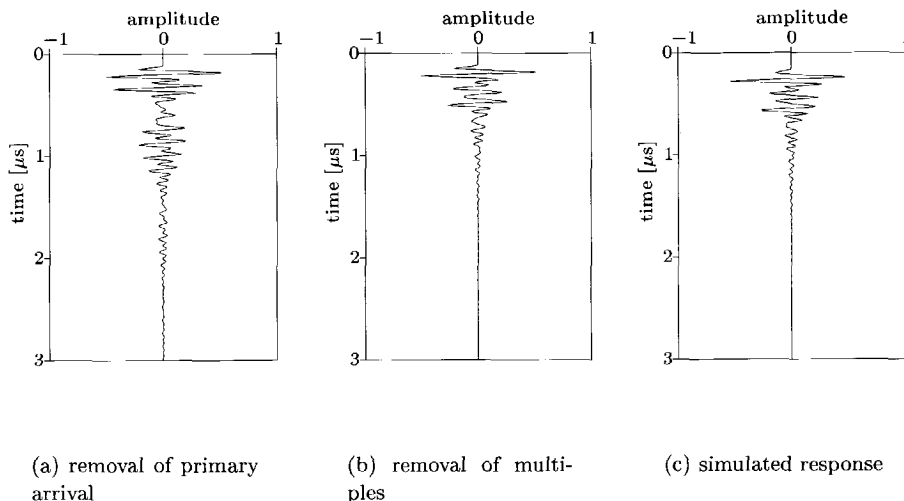


Fig. 4.17 Removal of the primary reflection, multiples and simulated response after elimination of layer 1.

ure 4.20(b). For these figures, grey level plots are used since they can easily be extended to the case where more simulations or measurements are performed on different positions, as will be shown later in this subsection. For clarity, the obtained depth-impedance values are compared in a normal plot in Figure 4.20(c).

The obtained acoustic impedance are compared with the true values in Table 4.7, and the relative error is indicated.

The RDI-algorithm can also be used to obtain the thickness of the layers — by means of Equation (4.2), provided that the acoustic velocity is known.

Assuming that this is the case, Table 4.8 gives the thicknesses of the different layers, as obtained by the RDI algorithm.

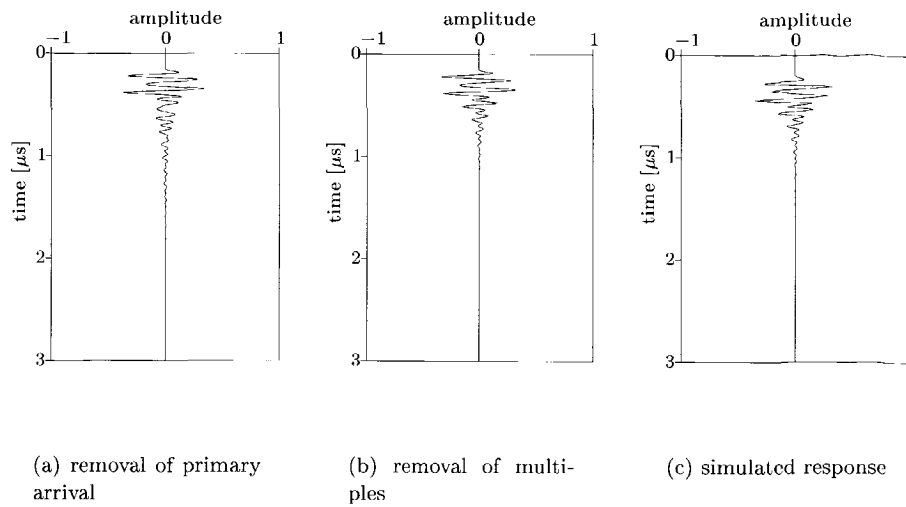


Fig. 4.18 Removal of the primary reflection, multiples and simulated response after elimination of layer 2.

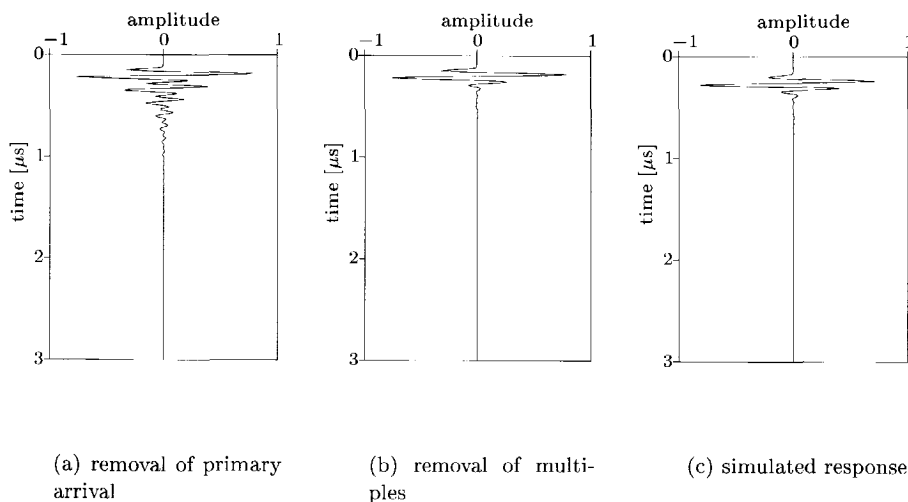


Fig. 4.19 Removal of the primary reflection, multiples and simulated response after elimination of layer 3.

From these tables, it can already be seen that the layer thickness is obtained with a higher accuracy than the impedance of the different layers. Also, by comparing the two aluminium layers, it follows that the obtained acoustic impedance of the bottom aluminium layer is less accurate than the acoustic impedance of the top aluminium

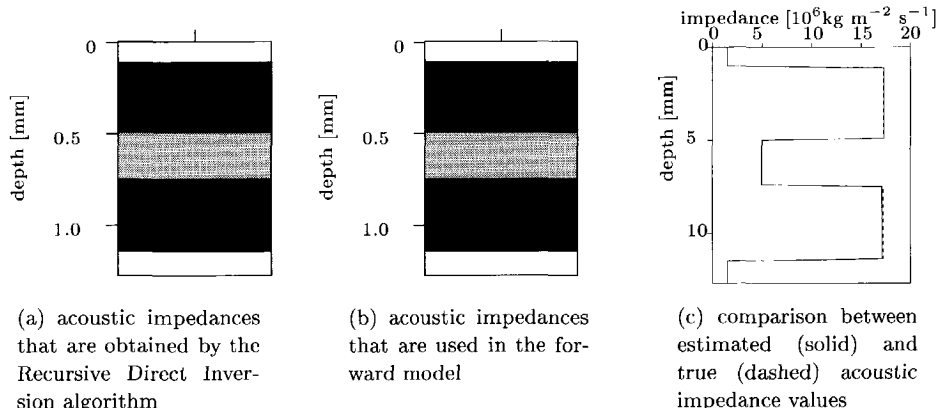


Fig. 4.20 Plot of the acoustic impedance as a function of depth for a simulated reflection measurement on a Glare 2/1 material. Dark colours mean a high impedance value.

Obtained layer impedance in a glare 2/1 configuration			
Layer	exact $Z_i[10^6 \text{kgm}^{-2}\text{s}^{-1}]$	calculated $Z_i[10^6 \text{kgm}^{-2}\text{s}^{-1}]$	$\delta(Z_i)$
0 (water)	1.48	1.48	0.00 %
1 (aluminium)	17.26	17.30	0.22 %
2 (prepreg)	4.96	4.95	0.06 %
3 (aluminium)	17.26	17.12	0.84 %

Table 4.7 Comparison between the acoustic impedance of the different layers used in the simulation and the acoustic impedance obtained by the Recursive Direct Inversion algorithm.

Obtained layer thickness in a glare 2/1 configuration			
Layer	exact $\Delta z_i[\text{mm}]$	calculated $\Delta z_i[\text{mm}]$	$\delta(\Delta z_i)$
0 (water)	0.1000	0.1000	0.00 %
1 (aluminium)	0.4000	0.3998	0.05 %
2 (prepreg)	0.2500	0.2499	0.04 %
3 (aluminium)	0.4000	0.3998	0.05 %

Table 4.8 Comparison between the layer thickness used in the simulation and the thickness obtained by the Recursive Direct Inversion algorithm.

layer. However, there is an excellent match between the true and the estimated values, even for the specific acoustic impedance of the bottom-most layer.

Glare 3/2

A more complex Glare configuration is the Glare 3/2 target, whose parameters are shown in Table 4.9. It is assumed that the attenuation coefficient γ_r of the prepreg layers is known ($\gamma_r = 1000 \text{ m}^{-1}$).

Glare 3/2 sample embedded in water					
Layer	material	$\Delta z(\text{mm})$	$\rho(\frac{\text{kg}}{\text{m}^3})$	$c(\frac{\text{m}}{\text{s}})$	$\gamma_r(\frac{1}{\text{m}})$
0	water	0.1	1000	1480	0
1	aluminium	0.4	2740	6300	0
2	prepreg	0.250	1600	3100	1000
3	aluminium	0.4	2740	6300	0
2	prepreg	0.250	1600	3100	1000
3	aluminium	0.4	2740	6300	0
4	water	∞	1000	1480	0

Table 4.9 Material parameters of a Glare 3/2 sample.

The simulated reflection response for this configuration — using the source signal emitted by the 15 MHz focussed transducer discussed in Chapter 3 — is shown in Figure 4.21(a).

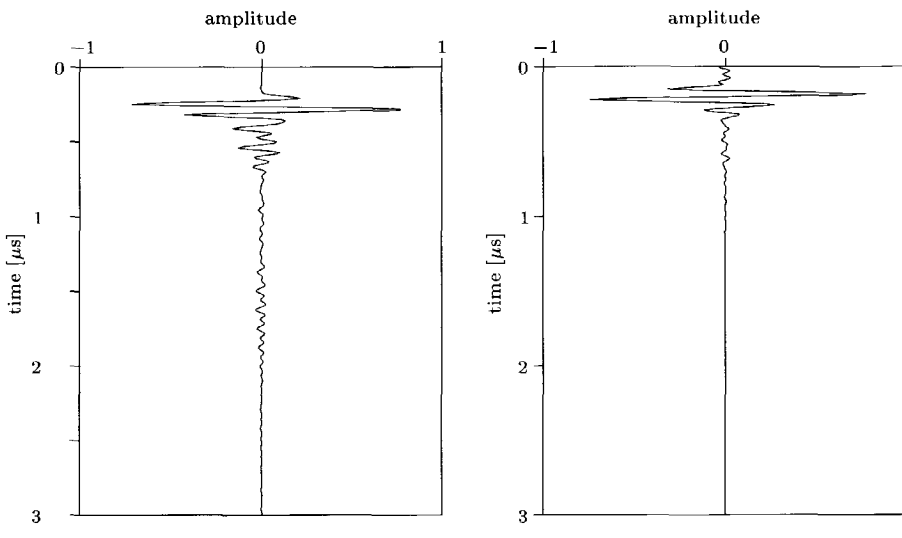
The Recursive Direct Inversion algorithm is used step by step to eliminate the effects of the different interfaces. After elimination of all but the bottom most interface, the signal in Figure 4.21(b) is obtained.

Applying the Recursive Direct Inversion algorithm on this simulated reflection measurement results in a number of traveltimes - reflection coefficient pairs.

The true values are compared with the parameters obtained by the Recursive Direct Inversion algorithm, and given in Table 4.10.

Material parameters in glare 3/2 configuration				
Layer	exact R	calculated R	exact $t[\text{s}]$	calculated $t[\text{s}]$
0	0.842	0.842	6.76×10^{-8}	6.76×10^{-8}
1	-0.554	-0.554	6.35×10^{-8}	6.35×10^{-8}
2	0.554	0.551	8.06×10^{-8}	8.07×10^{-8}
3	-0.554	-0.552	6.35×10^{-8}	6.33×10^{-8}
4	0.554	0.547	8.06×10^{-8}	8.08×10^{-8}
5	-0.842	-0.829	6.35×10^{-8}	6.32×10^{-8}

Table 4.10 Comparison between the material parameters used in the simulation and the parameters obtained by the Recursive Direct Inversion algorithm.



(a) Reflection response of a Glare 3/2 sample embedded in water

(b) Interface-free reflection response of the bottom-most layer, obtained after 5 recursion steps of the RDI algorithm

Fig. 4.21 Reflection response of a Glare 3/2 material and application of the RDI algorithm.

After the conversion from the traveltime-reflection coefficient pairs towards depth-impedance pairs, Figure 4.22(a) is obtained. The image containing the true parameters is given in Figure 4.22(b), and the results are compared in a line plot in Figure 4.22(c). The obtained values for the acoustic impedance of the different layers are also given in Table 4.11.

If the acoustic velocity in the layers is known and the RDI algorithm is used to obtain the thickness of the different layers, the values in Table 4.12 are found. From the results in these tables, it is clear that the deeper the layer, the less accurate the parameters are obtained. The results are still very good, though, even for the deeper layers.

Glare 3/2 with delamination

One of the goals of ultrasonic inspection of laminated materials is to check the quality of the bonds between the layers. The Recursive Direct Inversion Algorithm is able to detect a void inclusion between two layers, due to the extreme low impedance of

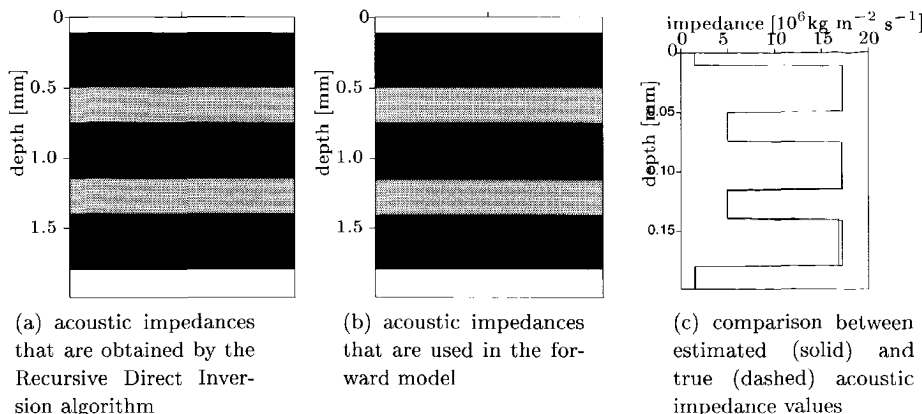


Fig. 4.22 Plot of the acoustic impedance as a function of depth for a simulated reflection measurement on a Glare 3/2 material. Dark colours mean a high impedance value.

Obtained layer impedance in a glare 3/2 configuration			
Layer	exact $Z_i[\text{kgm}^{-2}\text{s}^{-1}]$	calculated $Z_i[\text{kgm}^{-2}\text{s}^{-1}]$	$\delta(Z_i)$
0 (water)	1.48	1.48	0.00 %
1 (aluminium)	17.62	17.30	0.22 %
2 (prepreg)	4.96	4.96	0.06 %
3 (aluminium)	17.62	17.14	0.69 %
4 (prepreg)	4.96	4.94	0.44 %
5 (aluminium)	17.62	15.80	2.37 %

Table 4.11 Comparison between the acoustic impedance of the different layers used in the simulation and the acoustic impedance obtained by the Recursive Direct Inversion algorithm.

air and vacuum.

In Figure 4.23, a Glare 3/2 material with a delamination between layer 2 and layer 3 is shown. It is assumed that several measurements are performed on the material, the transducer is translated over a fixed step-size, 0.1 mm in the x -direction between two measurements. The delamination shows up between measurement points 128 and 192, and thus starts at a horizontal offset of 12.8 mm. Two simulated reflection measurement of this material are compared with each other in Figure 4.24: the first measurement is done outside the delamination area, while the second measurement is done inside this area.

Obtained layer thickness in a glare 3/2 configuration			
Layer	exact Δz_i [mm]	calculated Δz_i [mm]	$\delta(\Delta z_i)$
0 (water)	0.1000	0.1000	0.00 %
1 (aluminium)	0.4000	0.3997	0.07 %
2 (prepreg)	0.2500	0.2501	0.04 %
3 (aluminium)	0.4000	0.3987	0.32 %
4 (prepreg)	0.2500	0.2504	0.16 %
5 (aluminium)	0.4000	0.3983	0.42 %

Table 4.12 Comparison between the layer thickness used in the simulation and the thickness obtained by the Recursive Direct Inversion algorithm.

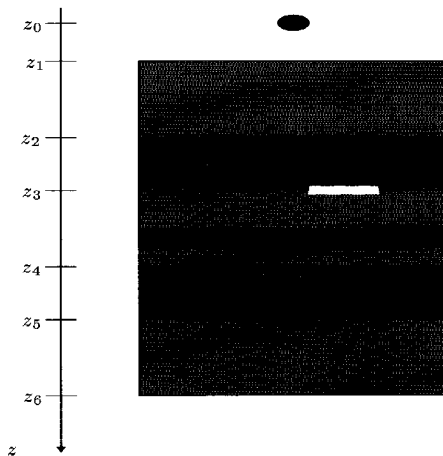
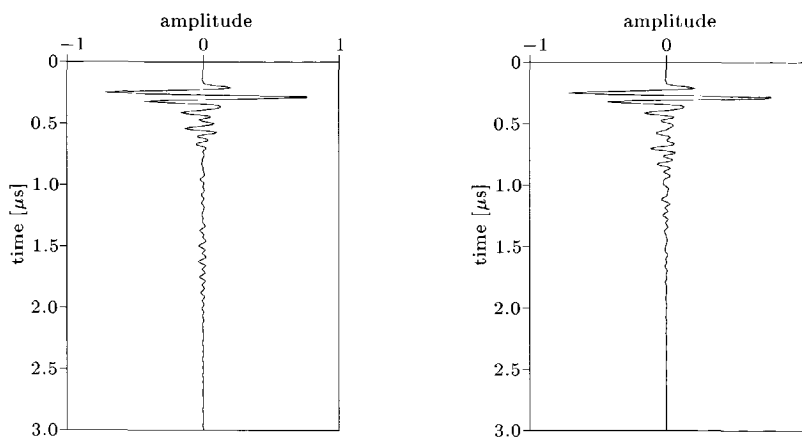


Fig. 4.23 Glare 3/2 material with a delamination between layer 2 and layer 3.

Combining the 256 one-dimensional simulations results in a line-scan. On each simulated reflection response, the Recursive Direct Inversion algorithm is applied. This leads to a number of traveltime-reflection coefficient pairs for each simulation. All these pairs are converted towards depth-impedance pairs. The result is shown in a grey level plot in Figure 4.25.

It can be clearly observed that the algorithm detects a layer with a very low impedance under layer 2 in the delamination area. Due to the high contrast in impedance, almost all the energy at the interface between layer 2 and layer 3 will be reflected. As a consequence, no information about deeper layers is obtained.



(a) simulated acoustic response obtained in the intact region

(b) simulated acoustic response obtained in the delaminated region

Fig. 4.24 Simulation of a reflection measurement on a Glare 3/2 material with a delamination between layer 2 and layer 3.

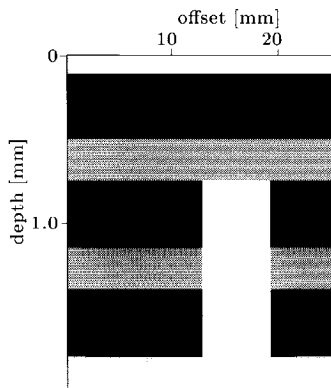


Fig. 4.25 Results of depth-impedance inversion on a Glare 3/2 material with a delamination.

4.6 Inversion on measured data

The simulations in the previous section give an indication about the stability of the direct inversion process. It was shown that the acoustic parameters of the different layers can be detected rather accurate, and the quality of the inversion decreases with the number of layers in the material.

In this section, the Recursive Direct Inversion algorithm is applied to real measurements. In Chapter 3, several reasons are given why there are differences between real data and data obtained by simulations. In order to minimise these differences, two things can be done:

- all physical phenomena that occur when a wave travels through a material have to be incorporated in the developed model — and as a consequence also in the inverse model;
- the data have to be obtained with a high accuracy.

4.6.1 Aluminium layer

In Figure 4.26, the source signal and the reflection measurement on an aluminium disk of approximately 0.8 mm are shown. The signals are obtained after performing a minimum-phase transformation on the source signal, and applying the same transformation on the reflection measurement, as described in Subsection 3.5.1.

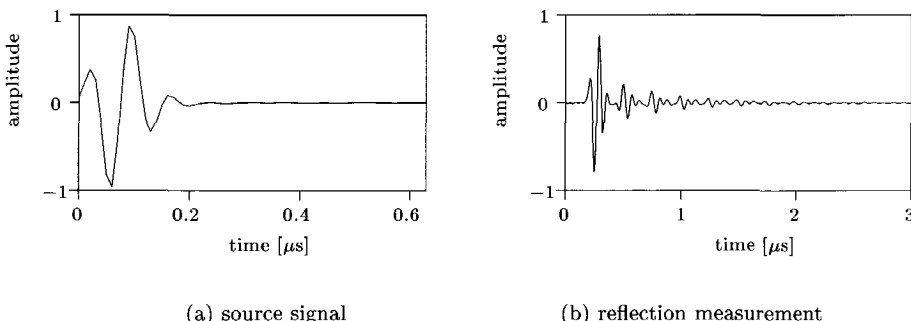


Fig. 4.26 Source and reflection measurement on an aluminium disk embedded in water, after a minimum-phase transformation has been applied

In Figure 4.27, the application of the Recursive Direct Inversion is shown. In the first step — Figure 4.27(b) — the primary arrival due to a reflection at the boundary between the water layer and the aluminium layer is removed. Based on the amplitude of this first arrival, the reflection coefficient between the water layer and the

aluminium layer is estimated. In Figure 4.27(c), the internal multiples in the aluminium layer are removed. The only event that is still present, is the reflection due to an acoustic contrast between the aluminium layer and the water layer beneath it. Based on the elapsed time before this event shows up in the signal, the traveltimes in the aluminium layer can be calculated. Also, the strength of this arrival can be used to calculate the reflection coefficient between the aluminium layer and the water layer beneath it.

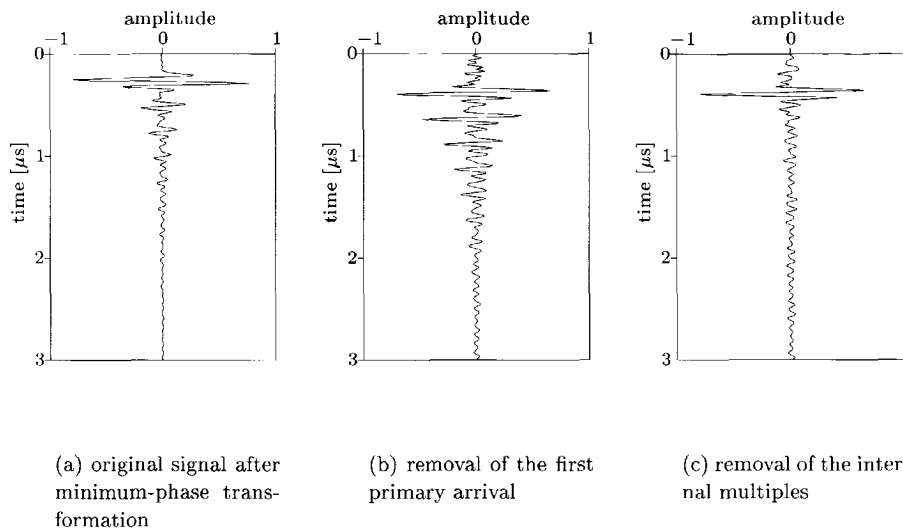


Fig. 4.27 Removal of the first primary reflection and the internal multiples in a measurement on an aluminium disk.

The obtained traveltimes and reflection coefficients are given in Table 4.13

Material parameters in aluminium layer configuration		
Layer	calculated R	calculated $t[\text{s}]$
0	0.851	6.76×10^{-8}
1	-0.782	1.22×10^{-7}

Table 4.13 Material parameters of an aluminium configuration embedded in water, as obtained by the Recursive Direct Inversion algorithm.

It appears that the traveltimes are obtained with a high accuracy. The obtained reflection coefficient is less accurate, but still gives an excellent indication of the specific acoustic impedance of the material under the aluminium layer, which is in this case water.

4.6.2 Glare 2/1

The ultimate goal is the inspection of laminated materials. Therefore, the Recursive Direct Inversion algorithm is applied on reflection measurements on the Glare 2/1 sample that was also discussed in the previous section. The material parameters as supplied by the manufacturer are given in Table 4.5. Applying the RDI algorithm results in the list of traveltime- reflection coefficients pairs given in Table 4.14.

Material parameters of a Glare 2/1 configuration		
Layer	calculated R	calculated t [s]
0	0.825	6.76×10^{-8}
1	-0.454	5.85×10^{-8}
2	0.421	8.30×10^{-7}
3	-0.606	5.92×10^{-8}

Table 4.14 Material parameters of a Glare 2/1 configuration embedded in water, as obtained by the Recursive Direct Inversion algorithm.

After the conversion from the reflection coefficients towards the acoustic impedances, a list of depth-impedance pairs is obtained. The depth-impedance plot obtained by the algorithm is compared with the expected depth-impedance parameters in Figure 4.28. The obtained acoustic impedances are compared with the expected

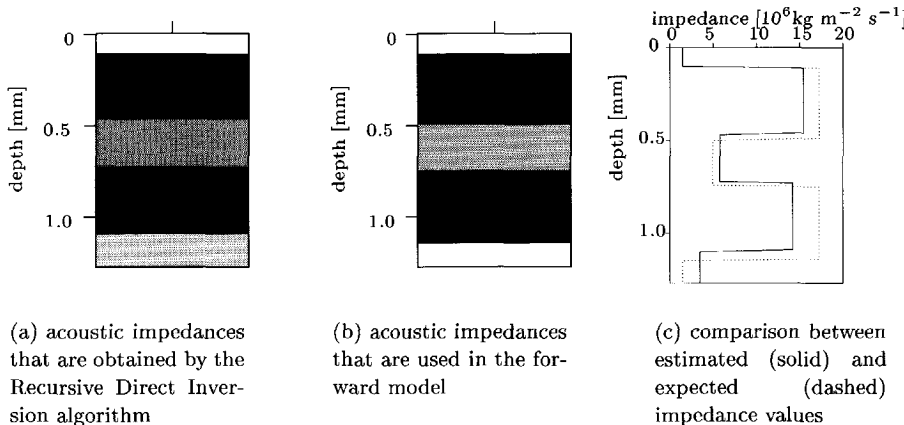


Fig. 4.28 Depth-impedance plot for a reflection measurement on a Glare 2/1 material. Dark colours mean a high acoustic impedance.

values in Table 4.15 and the relative difference is indicated. As can be seen from the table and the figures, the RDI algorithm is capable of determining the different layers

Obtained specific acoustic impedances for a glare 2/1 configuration			
Layer	expected $Z_i[\text{kgm}^{-2}\text{s}^{-1}]$	calculated $Z_i[\text{kgm}^{-2}\text{s}^{-1}]$	$\delta(Z_i)$
0 (water)	1.48	1000	0.00 %
1 (aluminium)	17.26	15.46	10 %
2 (prepreg)	4.96	5.80	17 %
3 (aluminium)	17.26	14.24	17 %

Table 4.15 Comparison between the expected acoustic impedance and the acoustic impedance obtained by the Recursive Direct Inversion algorithm applied on real measurements on Glare 2/1.

in the material, and there is a good match between the obtained and the expected specific acoustic impedances. Differences between the obtained and expected values may be due to both shortcomings in the theory and the algorithm as well as to erroneous values given by the manufacturer of the Glare sample.

If it is assumed that the acoustic velocity in the different layers is known, the RDI algorithm can be used to estimate the layer thickness. The result is given in Table 4.16.

Obtained layer thickness in a glare 2/1 configuration			
Layer	expected $\Delta z_i[\text{mm}]$	calculated $\Delta z_i[\text{mm}]$	$\delta(\Delta z_i)$
0 (water)	0.1000	0.1000	0.00 %
1 (aluminium)	0.4000	0.369	7.75 %
2 (prepreg)	0.2500	0.257	2.8 %
3 (aluminium)	0.4000	0.373	6.75 %

Table 4.16 Comparison between the expected layer thickness and the thickness obtained by the Recursive Direct Inversion algorithm applied on real measurements on Glare 2/1.

It appears that the thickness is obtained with a higher accuracy than the acoustic impedance. Although the difference between the expected acoustic impedance and the obtained acoustic impedance is rather large for the bottom aluminium layer, the algorithm should be able to detect possible delaminations. The impedance contrast between aluminium and void or air is indeed several orders of magnitude larger than the difference between the expected impedance of the bottom layer and the measured impedance.

Chapter 5

Iterative Parametric Optimisation

In this chapter, an alternative method for the Recursive Direct Inversion method developed in Chapter 4 is presented. The method described here is based on parametric optimisation. Unlike the specific method described in Chapter 4, parametric optimisation is a very general procedure applied in many disciplines. The knowledge of the specific problem is used in order to develop a method which is optimally suited for the particular problem of this research.

5.1 Theory of parametric optimisation

In Chapter 4, the acoustic parameters of the layers that constitute the target material are obtained by a direct inverse procedure. This is done by recursively applying operations that are the inverse of the operations used in the forward algorithm. The errors introduced in each step propagate through the next steps. As a consequence, the acoustic parameters of the bottom layers — the last layers to be handled — will be obtained with less accuracy than those of the top layers.

In this chapter, another method for retrieving the acoustic parameters is presented. In this method, the set of parameters plays the central role. Starting from an initial (estimated) set of acoustic parameters, the forward algorithm — see Chapter 2 — is used to predict the resulting wavefield. A comparison between this predicted wavefield and the measured wavefield can then be used in order to correct the initial set of parameters and to obtain a better one. This procedure is repeated until the predicted wavefield "matches" the measured wavefield.

5.1.1 Description of the optimisation problem

A measured quantity — or a series of quantities — \mathbf{y} can be considered as the result of an operator \mathcal{L} acting on a set of parameters \mathbf{u}^* :

$$\mathbf{y} = \mathcal{L}\{\mathbf{u}^*\}. \quad (5.1)$$

In the present research, the measured quantities are the elements of a time-series of pressure-related values, measured at a well-defined point in a medium. Actually, the pressure at a specified point is a continuous function of time, $y(t)$, and \mathbf{y} is a time-sampled version of $y(t)$:

$$\mathbf{y} = \begin{bmatrix} y_0 \\ y_1 \\ \dots \\ y_{n-1} \end{bmatrix}, \quad (5.2)$$

with n the number of sample points.

The operator \mathcal{L} describes the total action of a wave travelling from the transducer – located at the considered point – towards a material, interacting with the material, and travelling back towards the transducer. This action can be described using the wave theory as described in Chapter 2.

The set of parameters \mathbf{u}^* this operator acts on is determined by the geometrical and material properties of the constituting layers. In the inverse problem, these parameters are the unknown constants that cause the operator to yield the measured series of quantities. A different set of parameters will give a different set of measured quantities.

The goal of this chapter is to find the set of parameters that, when the operator acts upon it, gives the series of quantities that optimally matches the measured series of quantities. After the operator \mathcal{L} is applied to a set of parameters \mathbf{u} , a series \mathbf{p} is obtained:

$$\mathbf{p} = \mathcal{L}\{\mathbf{u}\}, \quad (5.3)$$

with

$$\mathbf{p} = \begin{bmatrix} p_0 \\ p_1 \\ \dots \\ p_{n-1} \end{bmatrix} \quad (5.4)$$

Different criteria can be used in order to determine when two series match each other. In order to be able to distinguish between the quality of two approaches, the

matching needs to be associated with a numerical value. In general, the quality of matching is described by an error function $\epsilon(\mathbf{u})$. The lower the value of this function, the better the matching.

Finding a minimum for the function $\epsilon(\mathbf{u})$ is done by an optimisation procedure. Since the value for $\epsilon(\mathbf{u})$ is dependent on a set of parameters, the problem is denoted as a parametric optimisation problem.

A function that is often used to associate a value with a set of parameters, is the (weighted) quadratic error function.

The weighted quadratic error function is defined as

$$\epsilon(\mathbf{u}) = \frac{1}{2} \sum_{i=0}^{n-1} w_i (p_i - y_i)^2. \quad (5.5)$$

When all weight quantities w_i are equal to 1, Equation (5.5) is simply called the quadratic error function.

If the residue function $r(t; \mathbf{u})$ is defined as

$$r(t; \mathbf{u}) = y(t) - \mathcal{L}\{\mathbf{u}\}, \quad (5.6)$$

the weighted quadratic error function is in matrix notation written as

$$\epsilon(\mathbf{u}) = \frac{1}{2} \mathbf{r}^T(\mathbf{u}) \mathbf{W} \mathbf{r}(\mathbf{u}), \quad (5.7)$$

where $\mathbf{r}(\mathbf{u})$ is the time-sampled counterpart of the residue function $r(t, \mathbf{u})$ and \mathbf{W} is a diagonal matrix whose elements are the weight quantities: $\mathbf{W} = \text{diag}(w_0, w_1, \dots, w_{n-1})$. When the weight quantities are all equal to 1, the quadratic error function becomes

$$\epsilon(\mathbf{u}) = \frac{1}{2} \|\mathbf{r}(\mathbf{u})\|^2. \quad (5.8)$$

The vector $\bar{\mathbf{u}}$ minimising $\epsilon(\mathbf{u})$ provides the set of parameters that best matches the set of real parameters \mathbf{u}^* , using the above-mentioned error criterion.

Different methods exists for finding the minimum of a multivariate smooth function. These methods are extensively described in the literature — e.g. Gill et al. (1981), Tarantola (1987). It is advantageous to choose and adapt a method that suits the needs for a particular problem. In this section, two general methods will be described.

The first method is a very general optimisation method based on the steepest-descent method. The second approach makes use of the properties of the least squares target function.

5.1.2 Steepest descent method

A general iterative method for finding a set of parameters \mathbf{u} that minimises the target function $\epsilon(\mathbf{u})$ is described by the following iterative algorithm:

*let \mathbf{u}^k be a vector containing the current estimated parameters
 compute a non-zero vector \mathbf{q}^k and a scalar α^k for which it holds that $\epsilon(\mathbf{u}^k - \alpha^k \mathbf{q}^k) < \epsilon(\mathbf{u}^k)$
 the new estimated parameter set \mathbf{u}^{k+1} is given by $\mathbf{u}^{k+1} = \mathbf{u}^k - \alpha^k \mathbf{q}^k$
 repeat these steps until the stop criterion — see subsection 5.1.4 — is satisfied.*

The algorithm is initiated by defining \mathbf{u}^0 to be the set of initial parameters. This initial set can be based on a-priori information. In general, the better the initial vector approaches the exact minimum of $\epsilon(\mathbf{u})$, the fewer steps will be required before the stop criterion is satisfied.

The procedure can be iteratively repeated and the resulting series $\mathbf{u}^0, \mathbf{u}^1, \dots$ will converge towards \mathbf{u}^* provided that the start point \mathbf{u}^0 is located close to the global minimum and not close to a local minimum.

This algorithm requires two important decisions in each step:

- choose a vector \mathbf{q}^k ;
- choose a scalar α^k .

The choice of \mathbf{q}^k

In order to allow convergence of the series $\mathbf{u}^k, \mathbf{u}^{k+1}, \dots$ the vector \mathbf{q}^k has to be chosen in a way that at least for some α^k it holds that

$$\epsilon(\mathbf{u}^k - \alpha^k \mathbf{q}^k) < \epsilon(\mathbf{u}^k). \quad (5.9)$$

The new parameter vector \mathbf{u}^{k+1} is then defined as

$$\mathbf{u}^{k+1} = \mathbf{u}^k - \alpha^k \mathbf{q}^k. \quad (5.10)$$

It is common to take the gradient of $\epsilon(\mathbf{u})$ evaluated at the point \mathbf{u}^k — denoted by $\nabla \epsilon(\mathbf{u}^k)$ — to be the search direction \mathbf{q}^k . A discussion of this can be found in the literature — e.g. Gill et al. (1981), Tarantola (1987) and Golub and Van Loan (1989). Intuitively this can be understood by considering that $-\nabla \epsilon(\mathbf{u}^k)$ points in the direction where the error decreases the fastest.

The gradient $\nabla\epsilon(\mathbf{u})$ is calculated as

$$\nabla\epsilon(\mathbf{u}) = \begin{bmatrix} \frac{\partial\epsilon}{\partial u_1} \\ \frac{\partial\epsilon}{\partial u_2} \\ \vdots \\ \frac{\partial\epsilon}{\partial u_m} \end{bmatrix}. \quad (5.11)$$

In the case no analytical expression for $\nabla\epsilon(\mathbf{u})$ is known, a numerical approximation for this gradient has to be used. The forward difference approximation is given by

$$\frac{\partial\epsilon(u_1, u_2, \dots, u_i, \dots, u_m)}{\partial u_i} \simeq \frac{\epsilon(u_1, u_2, \dots, u_i + \Delta, \dots, u_m) - \epsilon(u_1, u_2, \dots, u_i, \dots, u_m)}{\Delta}. \quad (5.12)$$

In this calculation, Δ has to be chosen sufficiently small since by definition, the gradient is obtained by letting Δ approach zero. On the other hand, when Δ is too small, computational errors might be introduced.

A better approximation for the partial derivatives is obtained by using central differences:

$$\frac{\partial\epsilon(u_1, u_2, \dots, u_i, \dots, u_m)}{\partial u_i} \simeq \frac{\epsilon(u_1, u_2, \dots, u_i + \frac{\Delta}{2}, \dots, u_m) - \epsilon(u_1, u_2, \dots, u_i - \frac{\Delta}{2}, \dots, u_m)}{\Delta}. \quad (5.13)$$

The drawback in using central differences is that for the calculation of the whole gradient, $2m$ evaluations of $\epsilon(\mathbf{u})$ are required, while by using forward differences the gradient is obtained after $m + 1$ evaluations.

The choice of α^k

Once the direction of search has been chosen, it is assumed that at least for one value of α^k Equation (5.9) is satisfied. Finding the value of α^k that minimises $\epsilon(\mathbf{u}^k - \alpha^k \mathbf{q}^k)$ then basically is an univariate minimisation problem. Methods for detecting the minimum of an univariate function can be found in the literature — e.g. Gill et al. (1981). In this case, however, it is not necessary to find *the best* value of α^k . In general, the more α^k minimises the left-hand side of Equation (5.9), the fewer iteration steps are needed before the stop criterion will be reached. However, the computations necessary to calculate this best value might not outweigh the gain obtained by the fewer iteration steps.

The error function can be calculated for different values of α^k , and the value that results in the lowest value for the error function can be taken to be α^k . This means that a lot of function evaluations are necessary, however.

It is also possible to calculate the error function for a few values of α^k , and then using a polynomial interpolation in order to obtain the minimum value. If n denotes the number of evaluations, taken at distinct values, there exists exactly one $n - 1$ -th degree polynomial that gives the exact values in the considered evaluation points. The coefficients of this polynomial can easily be calculated, by solving the Vandermonde System

$$\mathbf{V}^T \mathbf{a} = \mathbf{f}, \quad (5.14)$$

where \mathbf{a} is the vector containing the polynomial coefficients and \mathbf{f} is the vector containing the function evaluations. Further, \mathbf{V} is the Vandermonde matrix $V(x_0, \dots, x_n)$ — see Golub and Van Loan (1989). Assuming that the error function is smooth in the vicinity of the minimum — which is, as will be shown later, a fairly reasonable assumption in the specific problem of this research — this minimum can be approximated by using a second-order polynomial. A second-order polynomial has one minimum, and is uniquely defined when three of its (index, value) pairs are known. The value of the error function in the considered point is known. Two other values are needed in order to describe the polynomial.

Normalisation of the parameter space

Since \mathbf{u}^{k+1} , the update of the parameter-vector \mathbf{u}^k will be located on a line starting from the current vector \mathbf{u}^k and with direction $\nabla \epsilon(\mathbf{u}^k)$, it is advantageous that the solution \mathbf{u}^* is located on this line. Since the gradient of a function is perpendicular to the tangential plane in the considered point, this means that the shape of the contour of constant ϵ needs to be an m -th dimensional hyper-sphere. This means that if a vector \mathbf{u}^c is located a fixed distance Δ away from \mathbf{u}^* , the error function $\epsilon(\mathbf{u})$ is not dependent on the direction in which the vector has been moved. This is probably not the case for the chosen set of parameters in \mathbf{u} . Therefore, a transformation will be performed from the physical parameters in \mathbf{u} towards a new set of parameters \mathbf{v} that have contour-lines in the shape of a hyper-sphere in the vicinity of \mathbf{v}^* :

$$\mathbf{v} = \mathcal{F}\mathbf{u}, \quad (5.15)$$

where \mathcal{F} is a linear transformation. The physical set of parameters in \mathbf{u} is obtained from \mathbf{v} using the inverse transformation:

$$\mathbf{u} = \mathcal{F}^{-1}\mathbf{v}. \quad (5.16)$$

As a consequence of the transformation, the row $\mathbf{v}^0, \mathbf{v}^1, \dots$ will converge faster to \mathbf{v}^* than the row $\mathbf{u}^0, \mathbf{u}^1, \dots$ converges to \mathbf{u}^* . The row is obtained using the iterative relation

$$\mathbf{v}^{k+1} = \mathbf{v}^k - \alpha^k \nabla \epsilon(\mathbf{v}^k). \quad (5.17)$$

From Equations (5.3) and (5.5), it follows that the error function is written as

$$\epsilon(\mathbf{u}) = \frac{1}{2} \|\mathbf{y} - \mathcal{L}\{\mathbf{u}\}\|^2. \quad (5.18)$$

Using Equation (5.16) this becomes

$$\epsilon(\mathbf{v}) = \frac{1}{2} \|\mathbf{y} - \mathcal{L}\{\mathcal{F}^{-1}\{\mathbf{v}\}\}\|. \quad (5.19)$$

In the case where each transformed parameter is only dependent on one original parameter, the transformation operator \mathcal{F} can be written as follows:

$$\mathbf{v} = \mathbf{D}\mathbf{u} + \mathbf{g}, \quad (5.20)$$

where \mathbf{D} is a diagonal matrix $\mathbf{D} = \text{diag}(d_1, d_2, \dots, d_m)$ and \mathbf{t} is a translation vector. Further, since

$$\frac{\partial \epsilon}{\partial v_i} = \frac{\partial \epsilon}{\partial u_i} \frac{\partial u_i}{\partial v_i}, \quad (5.21)$$

it holds that

$$\nabla \epsilon(\mathbf{v}) = \mathbf{D}^{-1} \nabla \epsilon(\mathbf{u}). \quad (5.22)$$

As a consequence, it follows from Equations (5.17), (5.20) and (5.22) that an improved estimate of the set of parameters is given by

$$\mathbf{u}^{k+1} = \mathbf{u}^k - \alpha^k \mathbf{D}^{-2} \nabla \epsilon(\mathbf{u}^k). \quad (5.23)$$

5.1.3 Gauss-Newton Method

The method of the steepest descent as described in the previous subsection is very general and does not use the knowledge that the target function is the result of a least-squares problem. The second order Taylor expansion of the target function around \mathbf{u}^k is given by

$$\epsilon(\mathbf{u}^k + \mathbf{q}^k) = \epsilon(\mathbf{u}^k) + \nabla^T \epsilon(\mathbf{u}^k) \mathbf{q}^k + \frac{1}{2} (\mathbf{q}^k)^T \nabla^2 \epsilon(\mathbf{u}^k) \mathbf{q}^k, \quad (5.24)$$

with an error of order $\|\mathbf{q}^k\|^3$.

The vector \mathbf{q}^k that minimises expression (5.24) is obtained as the solution of the linear system

$$\nabla^2 \epsilon(\mathbf{u}^k) \mathbf{q}^k = -\nabla \epsilon(\mathbf{u}^k). \quad (5.25)$$

Using Equation (5.8), it follows that

$$\nabla \epsilon(\mathbf{u}^k) = \mathbf{J}^T(\mathbf{u}^k) \mathbf{r}(\mathbf{u}^k) \quad (5.26)$$

and

$$\nabla^2 \epsilon(\mathbf{u}^k) = \mathbf{J}^T(\mathbf{u}^k) \mathbf{J}(\mathbf{u}^k) + \sum_{i=0}^{m-1} r_i(\mathbf{u}) \mathbf{H}_i(\mathbf{u}), \quad (5.27)$$

where $\mathbf{J}(\mathbf{u})$ is the Jacobian matrix of $\mathbf{r}(\mathbf{u})$ and is defined as

$$\mathbf{J}(\mathbf{u}) = \begin{bmatrix} \frac{\partial r_0}{\partial u_1} & \frac{\partial r_0}{\partial u_2} & \cdots & \frac{\partial r_0}{\partial u_m} \\ \frac{\partial r_1}{\partial u_1} & \frac{\partial r_1}{\partial u_2} & \cdots & \frac{\partial r_1}{\partial u_m} \\ \cdots & \cdots & \cdots & \cdots \\ \frac{\partial r_{n-1}}{\partial u_1} & \frac{\partial r_{n-1}}{\partial u_2} & \cdots & \frac{\partial r_{n-1}}{\partial u_m} \end{bmatrix} \quad (5.28)$$

and \mathbf{H}_i is the Hessian matrix of $r_i(\mathbf{u})$ and is defined as

$$\mathbf{H}_i = \begin{bmatrix} \frac{\partial^2 r_i}{\partial u_1^2} & \frac{\partial^2 r_i}{\partial u_1 \partial u_2} & \cdots & \frac{\partial^2 r_i}{\partial u_1 \partial u_m} \\ \frac{\partial^2 r_i}{\partial u_2 \partial u_1} & \frac{\partial^2 r_i}{\partial u_2^2} & \cdots & \frac{\partial^2 r_i}{\partial u_2 \partial u_m} \\ \cdots & \cdots & \cdots & \cdots \\ \frac{\partial^2 r_i}{\partial u_m \partial u_1} & \frac{\partial^2 r_i}{\partial u_m \partial u_2} & \cdots & \frac{\partial^2 r_i}{\partial u_m^2} \end{bmatrix}. \quad (5.29)$$

If \mathbf{u}^k is located close to the minimum \mathbf{u}^* , the residues r_i will be small. As a consequence, the second term in Equation (5.27) will be small too, for reasonable values in the Jacobian and Hessian matrices.

Using Equations (5.26) and (5.27) together with this approximation in Equation (5.25), it follows that

$$\mathbf{J}^T(\mathbf{u}^k) \mathbf{J}(\mathbf{u}^k) \mathbf{q}^k = -\mathbf{J}^T(\mathbf{u}^k) \mathbf{r}^k. \quad (5.30)$$

The vector \mathbf{q}^k that solves this equation, is the solution of the linear least-squares problem

$$\frac{1}{2} \|\mathbf{J}^k(\mathbf{u}^k) \mathbf{q}^k + \mathbf{r}^k\|_2^2. \quad (5.31)$$

Different methods exist for solving linear least-square problems. One method exists in the \mathbf{QR} factorisation. If the orthogonal matrix $\mathbf{Q}^{m \times m}$ and the non-singular upper-triangular matrix $\mathbf{R}^{n \times n}$ compose the QR factorisation of $\mathbf{J}(\mathbf{u}^k)$

$$\mathbf{Q} \mathbf{J}^k = \begin{bmatrix} \mathbf{R} \\ \mathbf{0} \end{bmatrix}, \quad (5.32)$$

then \mathbf{q}^k is obtained as the solution of the linear system

$$\mathbf{R} \mathbf{q}^k = -\mathbf{Q}_1 \mathbf{r}^k, \quad (5.33)$$

where it holds that

$$\mathbf{Q} = \begin{bmatrix} \mathbf{Q}_1^{n \times m} \\ \mathbf{Q}_2^{(m-n) \times m} \end{bmatrix}. \quad (5.34)$$

5.1.4 Stop criterion

The goal of the iterative improvement is to obtain a series of vectors \mathbf{u} where the corresponding series of errors $\epsilon(\mathbf{u})$ converges towards 0. Since it is in general impossible to reach this limit — i.e., due to computational errors — a stop criterion has to be defined. It is common to stop the iteration once the error $\epsilon(\mathbf{u})$ is lower than a predefined value:

$$\epsilon(\mathbf{u}) < \epsilon^{\text{lim}}. \quad (5.35)$$

This criterion itself only gives a boundary for the global error, and not for the errors on the different parameters. Therefore, it makes sense to relate the choice of ϵ^{lim} to the errors on the physical parameters.

A vector $\Delta^{\text{lim}}\mathbf{u}$ is defined with each of the components representing the maximum allowed absolute error for the corresponding parameter in \mathbf{u} . A series of m error values is constructed by calculating the error resulting from a series of parameters $\mathbf{u}^{\text{lim},i}$. Each $\mathbf{u}^{\text{lim},i}$ is equal to the exact set \mathbf{u}^* , except for its i th component, which is given by

$$u_i^{\text{lim},i} = u_i^* + \Delta^{\text{lim}} u_i. \quad (5.36)$$

This corresponding error value is denoted by $\epsilon^{\text{lim},i}$. Taking

$$\epsilon^{\text{lim}} = \min_i \{\epsilon^{\text{lim},i}\}, \quad (5.37)$$

it is ensured that the error on the different components will never exceed the maximum allowed error, provided that the parameters are independent from each other. Generally, this is not the case, however, and the above-derived criterion has to be used with care.

Another reason for stopping the iterations, is the stagnation of the error value. Due to noisy data, computational errors, an imperfect forward model etc. it is unlikely that the error function can become as small as desired.

5.1.5 The choice of parameters

The iterative procedures described in the following sections result in the improvement of a set of parameters that are responsible for the result obtained by measurements. Physically, the traveltimes in each layer and the reflection coefficients at the boundaries between two layers determine the response of the material. Therefore, it makes sense to choose the traveltimes in each layer and the reflection coefficient at each boundary to be the parameters. In a configuration with $m/2$ layers, this

results in a set of m parameters. The vector \mathbf{u} is composed as

$$\mathbf{u} = \begin{bmatrix} t_0 \\ R_0 \\ t_1 \\ R_1 \\ \dots \\ t_{m-1} \\ R_{m-1} \end{bmatrix}, \quad (5.38)$$

with t_i the traveltime in layer i and R_i the reflection coefficient at the boundary between layer i and layer $i + 1$.

The result of the iterative procedure is a set of values for the traveltime and the reflection coefficients of the different layers. From these parameters, other values — material parameters — can be calculated, using Equations (4.1), (4.2), (4.3) and (4.4).

5.2 Optimisation on simulated data

Some of the benefits of applying an inversion algorithm on simulations are already mentioned in Section 4.5. Besides, in the case of a parametric optimisation, simulations can provide information about the quality of different optimisation algorithms.

5.2.1 Aluminium layer

In a first case, the simulated acoustic reflection response of a homogeneous aluminium layer embedded in water is studied. The water under the aluminium is considered to be a half-space, so the energy that transmits from the aluminium down into the water, will never be reflected back. The material parameters of the configuration are specified in Table 5.1.

Aluminium layer in water						
Layer	material	Δz (mm)	ρ (kg/m ³)	c (m/s)	R	t (s)
0	water	0.1	1000	1480	0.842	6.75610^{-8}
1	aluminium	0.5	2740	6300	-0.842	7.93610^{-8}
2	water	∞	1000	1480	-	-

Table 5.1 Material properties for an aluminium disk embedded in water.

The source signal used in the simulations in this section is a real measured signal, obtained with a 15-MHz transducer with a focus point at 76.2 mm. The time-signal of this source signal is shown in Figure 5.1(a).

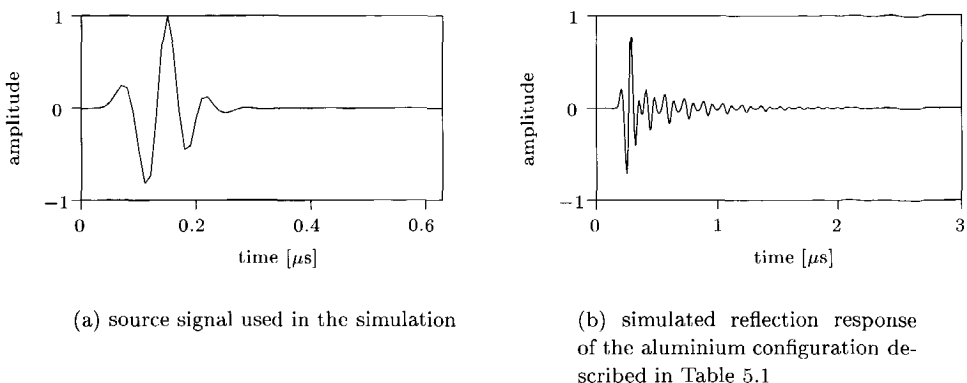


Fig. 5.1 Source signal and simulation of the acoustic reflection response of an aluminium disk embedded in water.

Using the forward model as explained in Chapter 2, the scattered reflected wavefield at the transducer can be calculated. The result is shown in Figure 5.1(b).

Changing the acoustic parameters of the aluminium layer will give a different result. In Table 5.2, a slightly different configuration than the one in Table 5.1 is given, in which the aluminium disk is 0.02 mm thicker.

Aluminium layer in water						
Layer	material	Δz (mm)	ρ ($\frac{\text{kg}}{\text{m}^3}$)	c ($\frac{\text{m}}{\text{s}}$)	R	t (s)
0	water	0.1	1000	1480	0.815	6.75610^{-8}
1	aluminium	0.52	2300	6300	-0.815	8.25410^{-8}
2	water	∞	1000	1480	-	-

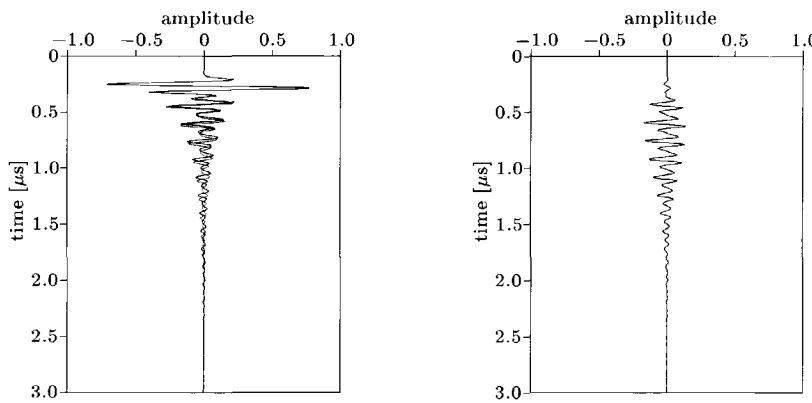
Table 5.2 Perturbed material properties for an aluminium disk embedded in water.

The corresponding acoustic responses of these configurations are compared with each other in Figure 5.2.

In the following, it is assumed that the material parameters in Table 5.1 provide the "true" set of parameters. The parameters in Table 5.2 on the other hand are the "estimated" set, and they will be used as the initial set for the optimisation routines¹. Note that in this case, Figure 5.2(b) is the residue function $r(t)$, according to Equation (5.6).

Equation (5.8) can be used to calculate the error for each configuration. Using the

¹It has to be mentioned that the algorithm will only optimise R_i and t_i . The other parameters follow from the obtained R_i and t_i , using some a-priori information.



(a) acoustic reflection responses of the configurations described in Table 5.1 (solid line) and Table 5.2 (dotted line).

(b) difference between the two simulations

Fig. 5.2 Simulated reflection measurement on an aluminium layer embedded in water for two sets of material parameters.

configuration of Table 5.2, an error of 0.225 is obtained.

By varying the traveltimes in the water layer and the aluminium layer and the reflection coefficients at the interfaces of the aluminium layer, contour plots of the error function are obtained.

Without scaling the parameters, the error as a function of the traveltimes in the aluminium layer and the reflection coefficient between the aluminium layer and the water beneath it, is given in the contour plot of Figure 5.3(a). It is clear that the error function is much more sensitive to changes in the traveltimes than to changes of the same magnitude in the reflection coefficient.

Normalisation of the parameters can lead to more circular contour plots. According to Gill et al. (1981), *the first basic rule of scaling is that the variables of the scaled problem should be of similar magnitude and of order unity in the region of interest*. Therefore, each of the parameters is transformed using Equation (5.20), where

$$d_i = u_i^{-1}, \quad (5.39)$$

$$g_i = 0, \quad (5.40)$$

where u_i is the initial value of parameter i . This leads to the scaled window in Figure 5.3(b). Still, the influence of one parameter — the traveltimes — outweighs the influence of the other parameter — the reflection coefficient.

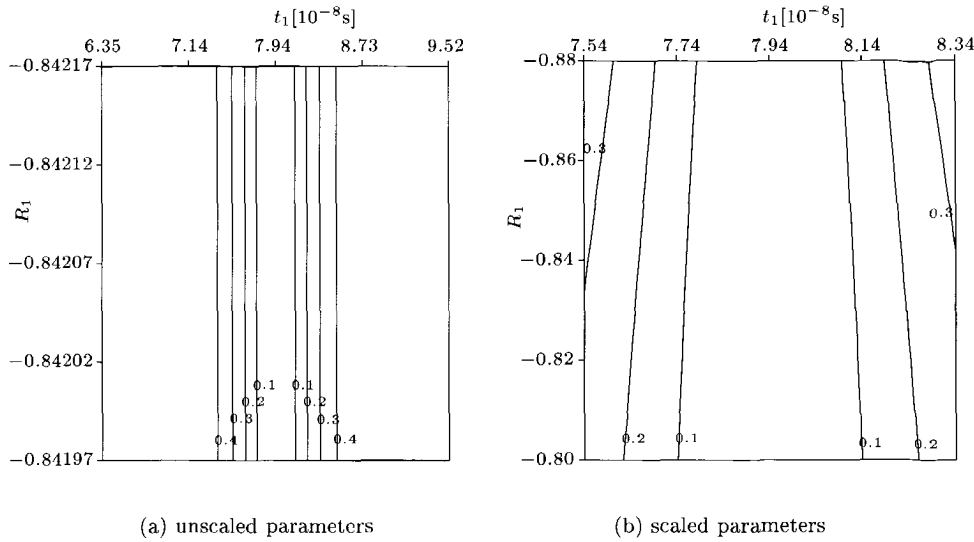


Fig. 5.3 Contour plot of the error function for different values of the traveltime in the aluminium layer t_1 and the reflection coefficient between aluminium and water R_1 .

In Figure 5.4(a), the range for the parameters is manually varied until the contour lines are rather circular. Each parameter is then situated at $u_i^{\min} \leq u_i \leq u_i^{\max}$. A transformation from the old set of parameters \mathbf{u} towards a new set \mathbf{v} where it holds that $-1 \leq v_i \leq 1$ for each v_i is obtained as follows:

$$\mathbf{v} = \mathbf{D}\mathbf{u} + \mathbf{g} \quad (5.41)$$

where \mathbf{D} is the diagonal matrix given by

$$\mathbf{D} = \text{diag} \left(\frac{2}{u_0^{\max} - u_0^{\min}}, \frac{2}{u_1^{\max} - u_1^{\min}}, \dots, \frac{2}{u_{n-1}^{\max} - u_{n-1}^{\min}} \right) \quad (5.42)$$

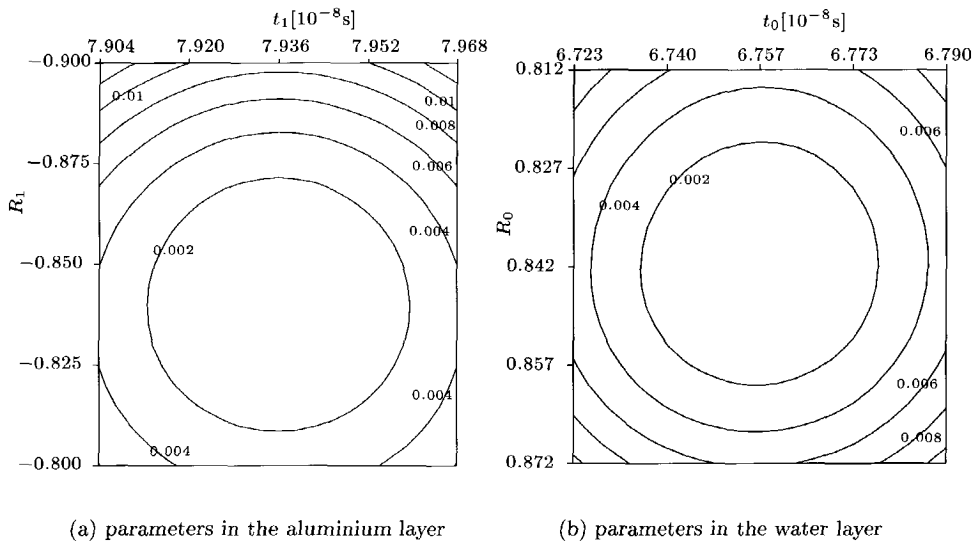
and \mathbf{g} is a translation vector given by

$$g_i = -\frac{u_i^{\max} + u_i^{\min}}{u_i^{\max} - u_i^{\min}}. \quad (5.43)$$

Unfortunately, the boundaries given by u_i^{\min} and u_i^{\max} are generally not known.

The dependence of the error function on the manually scaled parameters of the water layer is given in the contour plot of Figure 5.4(b).

From Figures 5.4(a) and 5.4(b), it follows that the traveltime in a layer and the reflection coefficient between the considered layer and the subsequent layer can be calculated almost independently from each other.



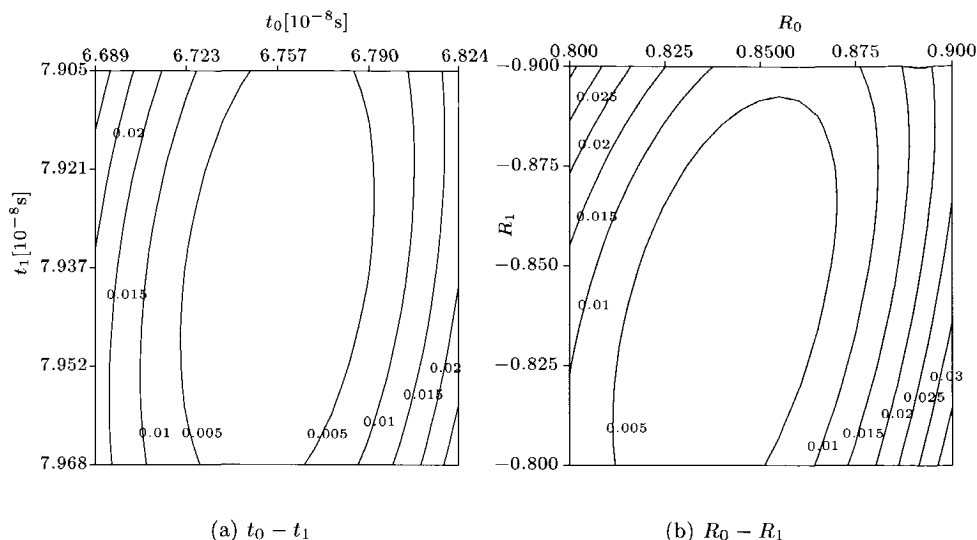


Fig. 5.5 Contour plot of the error function for different values of the traveltimes in the water layer and the aluminium layer and the reflection coefficients between water, aluminium and water.

ters until the result matches with the result of the true configuration. The gradient $\nabla\epsilon(\mathbf{u}^0)$ is calculated using Equations (5.11), and the search direction \mathbf{q}^0 is obtained using Equation (5.23):

$$\mathbf{q}^0 = \mathbf{D}^{-2} \nabla\epsilon(\mathbf{u}^0) = \begin{bmatrix} 2.273 \cdot 10^{-7} \\ -0.500 \\ 6.348 \cdot 10^{-7} \\ -0.561 \end{bmatrix}, \quad (5.45)$$

where the elements of \mathbf{D} are composed using Equation (5.43). A scalar α is now needed, before Equation (5.23) can be applied. The upper limit on α is determined by the constraints for the parameters. These constraints have to be chosen by the user², based on a priori knowledge of the material:

$$\mathbf{u}^{\min} = \begin{bmatrix} 6.081 \cdot 10^{-8} \\ 0.8 \\ 7.873 \cdot 10^{-8} \\ -0.9 \end{bmatrix}, \mathbf{u}^{\max} = \begin{bmatrix} 7.302 \cdot 10^{-8} \\ 0.9 \\ 8.571 \cdot 10^{-8} \\ -0.8 \end{bmatrix}. \quad (5.46)$$

²Note that these boundaries in general are not the same boundaries that define the transformation matrix and vector of Equations 5.42 and 5.43.

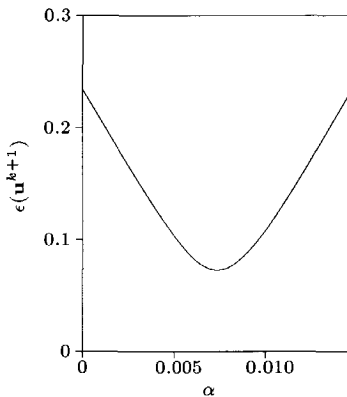


Fig. 5.6 Behaviour of the error-function as a function of the scaling coefficient α

In order for \mathbf{u}^{k+1} to be located inside the area bounded by the constraints, it follows that the maximum value for α is $1.50 \cdot 10^{-2}$.

In Figure 5.6, the error function is shown as a function of α .

From this plot, it turns out that the assumption that the error function is smooth in the neighbourhood of the minimum is reasonable.

For the choice of α^k , as needed in Equation (5.23), a second order polynomial interpolation is performed, after the search interval has been reduced by using the Golden section search — see Gill et al. (1981).

For each iteration step, the obtained acoustic parameters are shown in Figure 5.7. It can be seen that after a few steps, the traveltimes are obtained with a high accuracy. It takes a lot more iteration steps, however, in order to obtain the same accuracy for the reflection coefficients.

Second order approach

The second order method that will be used here, is based on the Gauss-Newton method. Optimisation methods given in the literature are rather general, though, and do not take into account the specific behaviour of the problem.

Since it follows from the contour plots that the reflection coefficients and traveltimes are rather independent from each other, and since the error function is much more influenced by changes in a traveltimes than equal (absolute or relative) changes in a reflection coefficient, a modified method is used.

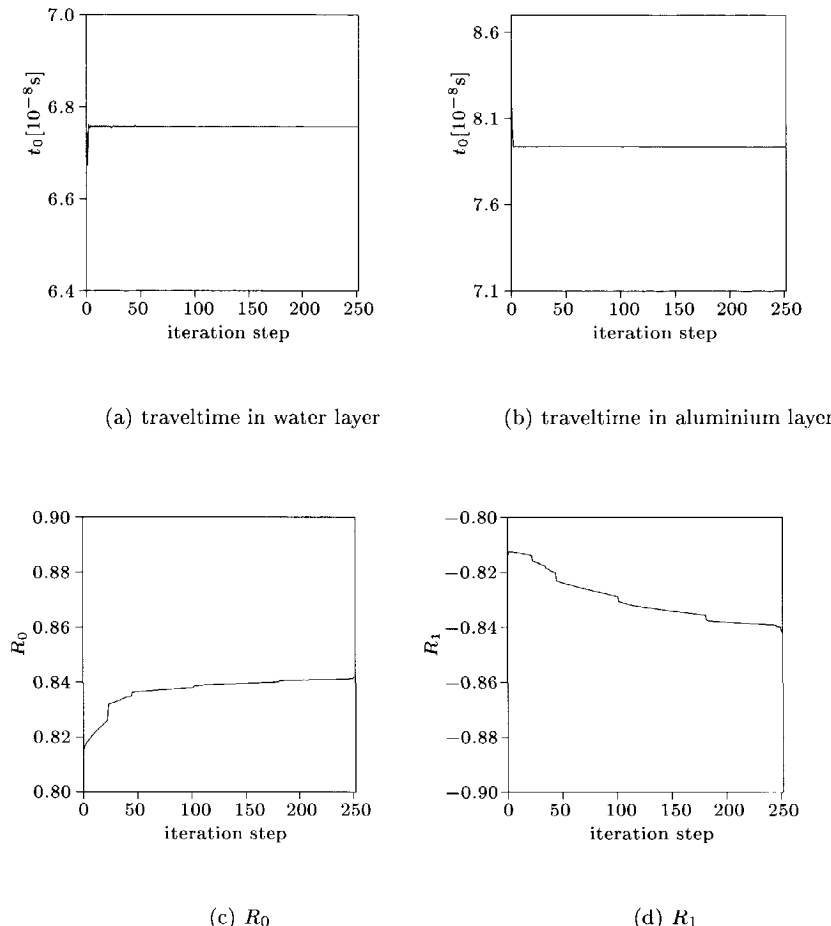


Fig. 5.7 Improvements on the material parameters of a water-aluminium configuration obtained after successive steps of the linear optimisation algorithm

Each iteration step consists of two parts. In the first part, only the traveltimes are updated, and the reflection coefficients are kept constant. This will have a major influence on the value of the error function. Furthermore, the influence of the different traveltimes is about the same order of magnitude, so no complicated parameter scaling is required. In the second part, the newly obtained traveltimes are kept constant, and the reflection coefficients are updated. This results in a minor improvement on the error, but it can lead to rather large updates for the reflection coefficients.

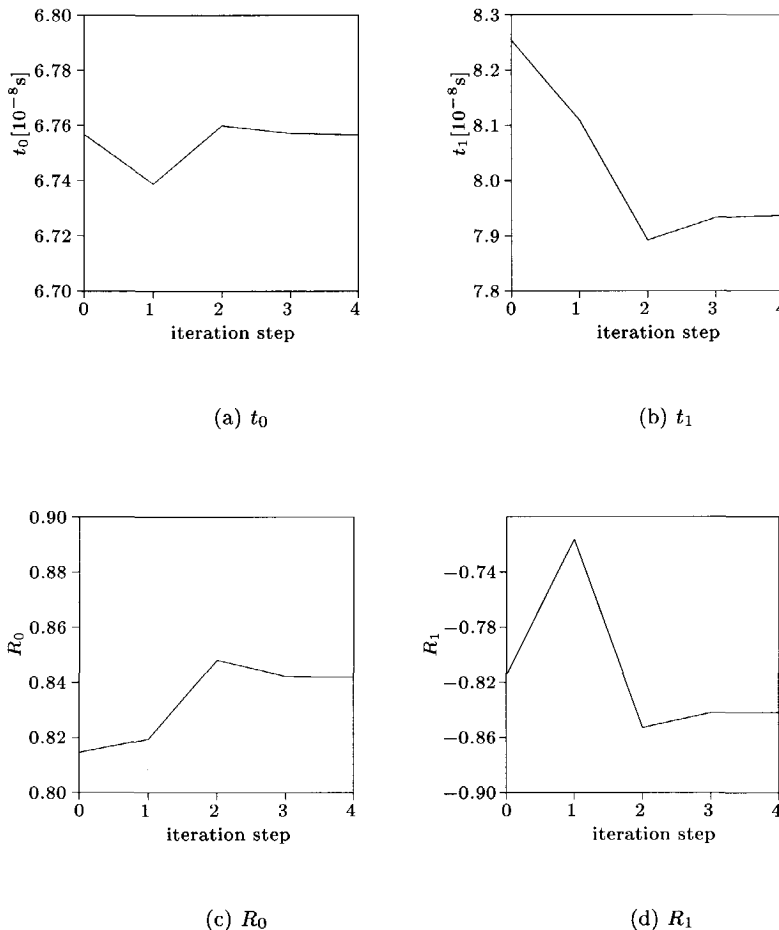


Fig. 5.8 Improvements on the material parameters of an aluminium layer embedded in water, obtained after successive steps of the modified Gauss-Newton algorithm.

The results of this modified Gauss-Newton algorithm are for the successive steps given in Figure 5.8. It is remarkable that only 4 iteration steps are needed in order to obtain the same accuracy as is obtained with 253 iteration steps using the linear method with automatic scaling of the parameters. Therefore, in the remainder of this chapter, only the modified Gauss-Newton method will be used.

5.2.2 Glare

In this subsection, the modified Gauss-Newton algorithm is used to obtain the "true" material parameters of a glare 2/1 material, starting from an initial set of parameters that is different from the true one. The true set is given in Table 5.3 and the perturbed parameters are given in Table 5.4.

Glare 2/1 in water						
Layer	material	Δz (mm)	ρ ($\frac{\text{kg}}{\text{m}^3}$)	c ($\frac{\text{m}}{\text{s}}$)	R	t (s)
0	water	0.1	1000	1480	0.842	$6.756 \cdot 10^{-8}$
1	aluminium	0.4	2740	6300	-0.554	$6.349 \cdot 10^{-8}$
2	prepreg	0.25	1600	3100	0.554	$8.065 \cdot 10^{-8}$
3	aluminium	0.4	2740	6300	-0.842	$6.349 \cdot 10^{-8}$
4	water	∞	1000	1480	-	-

Table 5.3 "True" material properties for a Glare 2/1 material embedded in water.

Glare 2/1 in water						
Layer	material	Δz (mm)	ρ ($\frac{\text{kg}}{\text{m}^3}$)	c ($\frac{\text{m}}{\text{s}}$)	R	t (s)
0	water	0.1	1000	1480	0.825	$6.756 \cdot 10^{-8}$
1	aluminium	0.395	2740	6100	-0.480	$6.475 \cdot 10^{-8}$
2	prepreg	0.25	1600	3400	0.477	$7.353 \cdot 10^{-8}$
3	aluminium	0.405	2740	6300	-0.824	$6.429 \cdot 10^{-8}$
4	water	∞	1000	1480	-	-

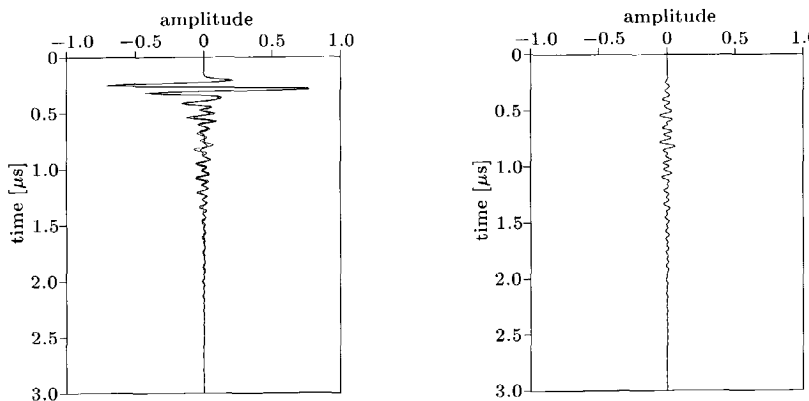
Table 5.4 Initial material properties for a Glare 2/1 material embedded in water.

The corresponding acoustic responses of these configuration are compared with each other in Figure 5.9. Note again that in Figure 5.9(b), the residue function $r(t)$ is shown — see Equation (5.6).

The influence of perturbations on the traveltimes in one layer and the reflection coefficient at the bottom interface of the considered layer are shown in the contour plots of Figure 5.10.

Again, it can be seen that the reflection coefficients can be calculated relatively independent from the traveltimes. The mutual dependence of the traveltimes in the different layers is shown in Figure 5.11, and the dependence on the reflection coefficients is shown in Figure 5.12.

Starting with the initial set of 8 parameters of Table 5.4, the modified Gauss-Newton method is applied. The improvements for the parameters after each iteration step



(a) acoustic reflection responses of the configurations described in Table 5.3 (solid line) and Table 5.4 (dotted line).

(b) difference between the two simulations

Fig. 5.9 Simulated reflection measurement on a Glare 2/1 material embedded in water for two sets of parameters.

are given in Figure 5.13. Again, it can be seen that the modified Gauss-Newton method gives the "true" values after very few iterations.

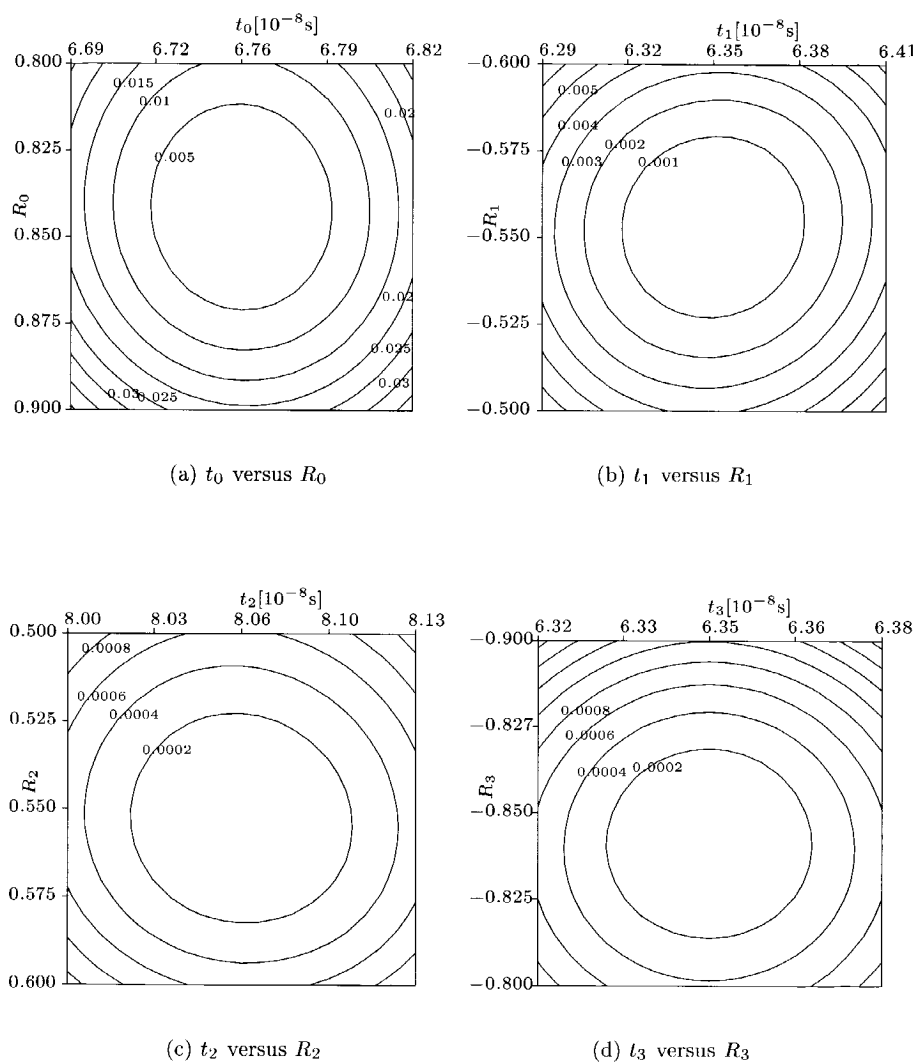


Fig. 5.10 Contour plots obtained by altering the traveltime and reflection coefficient in one layer of the Glare 2/1 configuration.

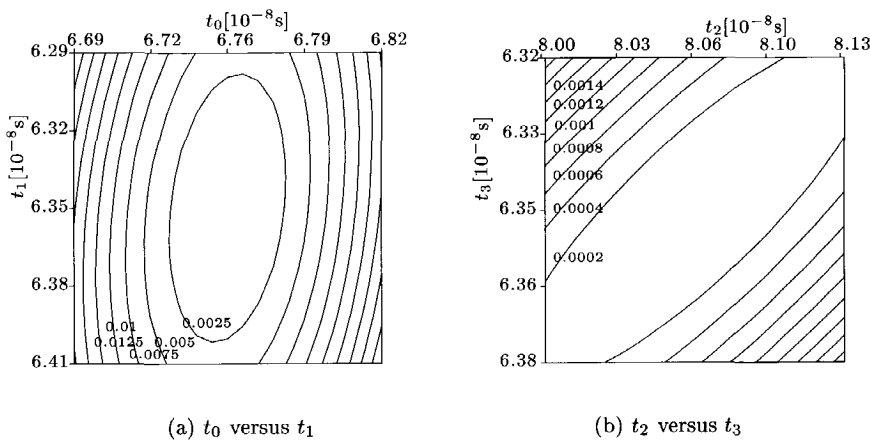


Fig. 5.11 Contour plots obtained by altering the traveltimes in two different layers of the Glare 2/1 configuration.

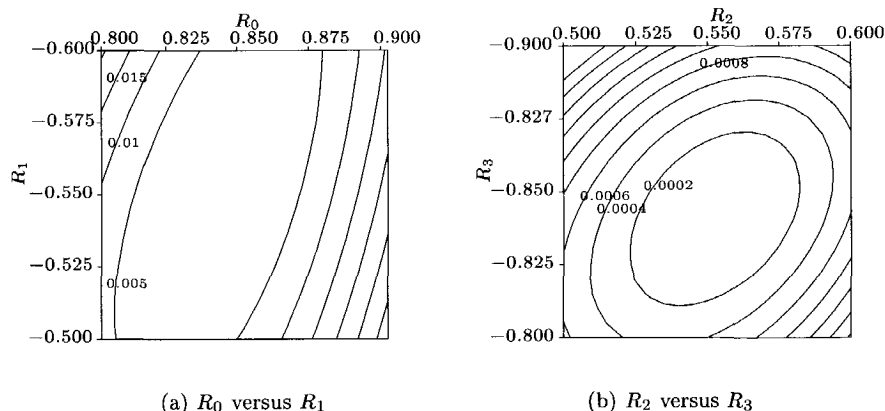


Fig. 5.12 Contour plots obtained by altering the reflection coefficients in two different layers of the Glare 2/1 configuration.

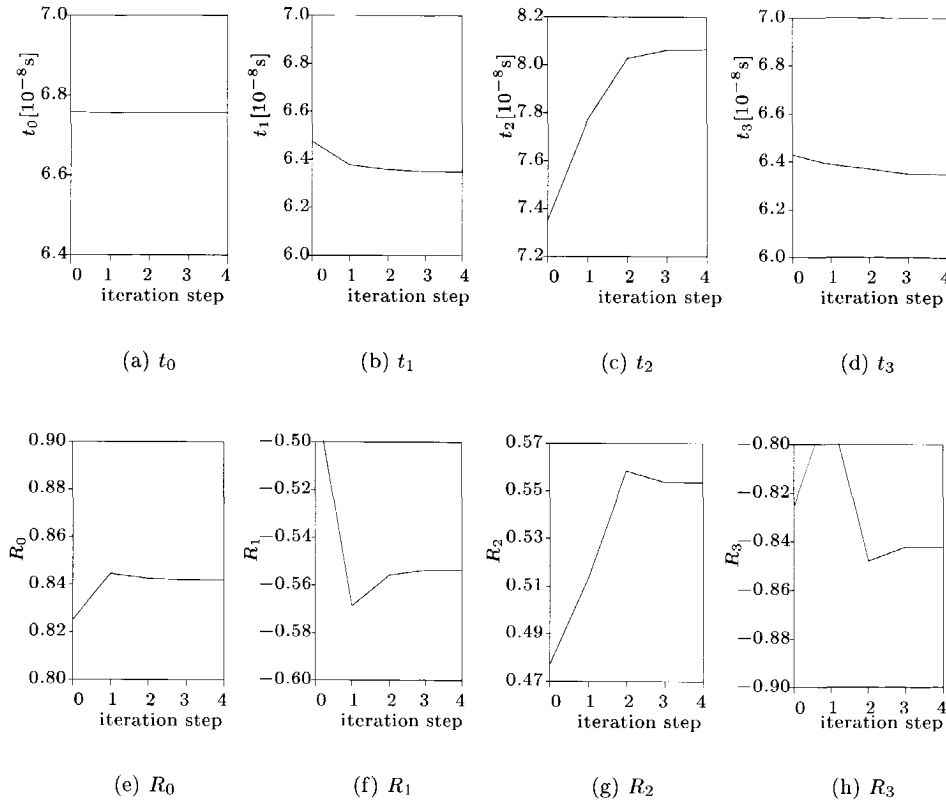


Fig. 5.13 Improvements on the material parameters obtained after successive steps of the modified Gauss-Newton algorithm.

5.3 Optimisation on measured data

In the previous section, it is shown that the optimisation algorithms can be used to obtain the "true" set of parameters of a configuration, starting from an initial "estimated" set.

The modified Gauss-Newton algorithm will now be used in order to obtain the set of parameters where the corresponding simulated reflection response matches with the real measurement, for a number of configurations.

5.3.1 Aluminium layer

In this subsection, the configuration exists of an aluminium disk embedded in water. The same configuration is discussed in section 4.6. The material parameters of this configuration, obtained by the Recursive Direct Inversion are given in Table 4.13. Based on these parameters and on the expected material parameters of aluminium, an initial set is given in Table 5.5.

Material parameters in aluminium layer configuration		
Layer	initial R	initial t [s]
0	0.842	$6.76 \cdot 10^{-8}$
1	-0.842	$1.22 \cdot 10^{-7}$

Table 5.5 Initial material parameters of an aluminium configuration embedded in water.

The improvements of 10 successive optimisation steps are given in Figure 5.14. The results are compared with the obtained parameters using the Recursive Direct Inversion method in Table 5.6. The obtained values for the reflection coefficients and the

Material parameters in aluminium layer configuration				
Layer	R (RDI)	R (IPO)	$t(RDI)$ [s]	$t(IPO)$ [s]
0	0.851	0.845	$7.50 \cdot 10^{-8}$	$7.50 \cdot 10^{-8}$
1	-0.782	-0.755	$1.22 \cdot 10^{-7}$	$1.22 \cdot 10^{-7}$

Table 5.6 Comparison between material parameters of an aluminium configuration embedded in water obtained with the Recursive Direct Inversion (RDI) method and the method of Iterative Parametric Optimisation (IPO).

traveltimes are comparable for both methods. The traveltimes are obtained with a very high accuracy, and the reflection coefficients give a strong indication about the specific acoustic impedance of the material beneath the aluminium layer — which is water, in the used configuration.

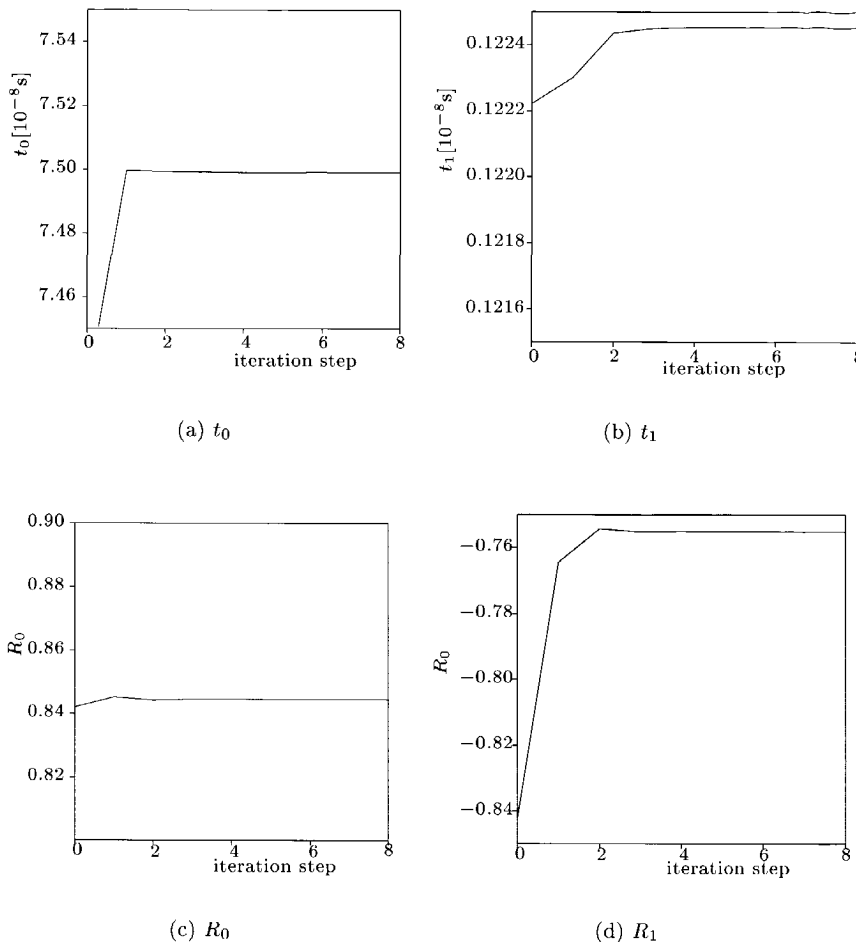


Fig. 5.14 Improvements of the material parameters of the aluminium configuration obtained after successive steps of the modified Gauss-Newton algorithm

5.3.2 Glare 2/1

At this point, the modified Gauss-Newton algorithm is used to obtain the material parameters of a Glare 2/1 material. The reflected pressure wavefield is measured, and in Section 4.6.2, the Recursive Direct Inversion algorithm is used in order to obtain the material parameters. The results of this inversion are given in Table 4.16 and Table 4.15.

An initial set of parameters for the parametric optimisation is given in Table 5.7.

Material parameters in a Glarc 2/1 configuration			
Layer	material	initial R	initial t [s]
0	water	0.842	$6.76 \cdot 10^{-8}$
1	aluminium	-0.553	$6.35 \cdot 10^{-8}$
2	prepreg	0.551	$8.06 \cdot 10^{-8}$
3	aluminium	-0.842	$6.35 \cdot 10^{-8}$
4	water	-	

Table 5.7 Initial material parameters of a Glare 2/1 configuration embedded in water.

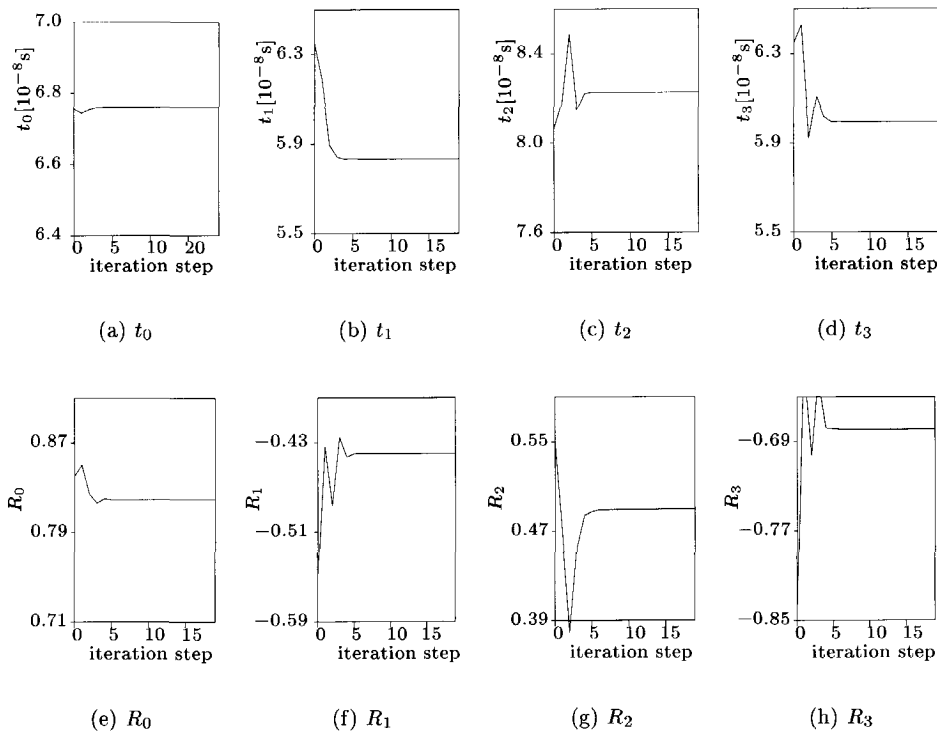


Fig. 5.15 Improvements on the material parameters of a measured Glare 2/1 material obtained after successive steps of the modified Gauss-Newton optimisation algorithm.

The results of 20 successive optimisation steps is shown in Figure 5.15. The resulting reflection coefficients and traveltimes are given in Table 5.8. An interesting check for the result given by the optimisation algorithm is the comparison between the

Material parameters of a Glare 2/1 configuration		
Layer	calculated R	calculated $t[\text{s}]$
0	0.819	$6.76 \cdot 10^{-8}$
1	-0.439	$5.83 \cdot 10^{-8}$
2	0.489	$8.23 \cdot 10^{-7}$
3	-0.679	$5.99 \cdot 10^{-8}$

Table 5.8 Material parameters of a Glare 2/1 configuration embedded in water, as obtained after 20 steps of the Iterative Parametric Optimisation algorithm.

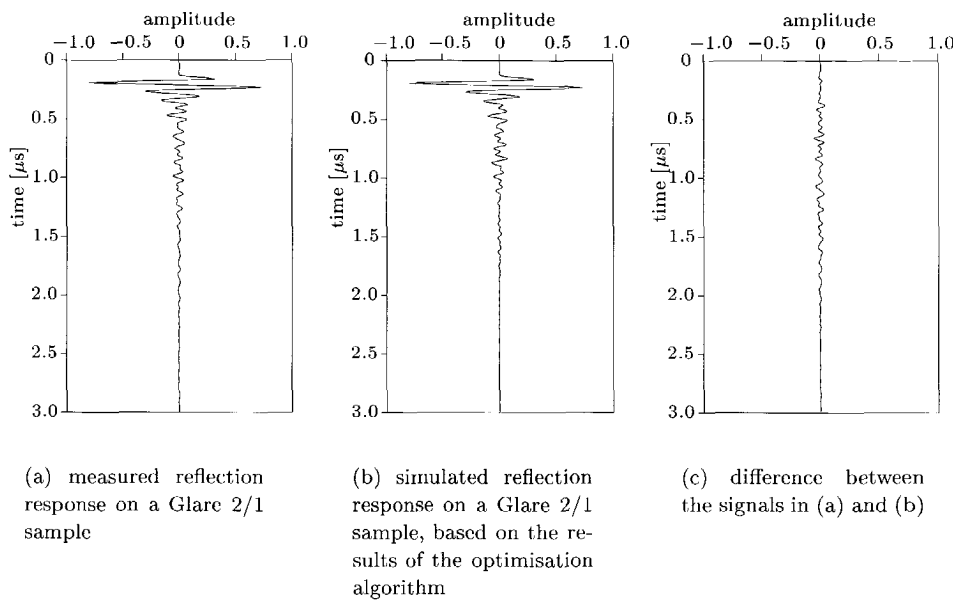


Fig. 5.16 Comparison between measured reflected signal and signal obtained based on the results of the optimisation algorithm.

measured signal and a simulation that is obtained using the acoustic parameters returned by the optimisation. In Figure (5.16), these two signals are compared with each other. It can be seen that the differences between the signals are very small.

Assuming that the acoustic velocity inside the layers is well-known, a series of depth-impedance values can be calculated. Together with the expected values, the obtained plot is given in Figure 5.17. The obtained values for the specific acoustic impedances are compared with the expected values and the values obtained by the RDI-method in Table 5.9. If it is assumed that the acoustic velocity in the different layers is known,

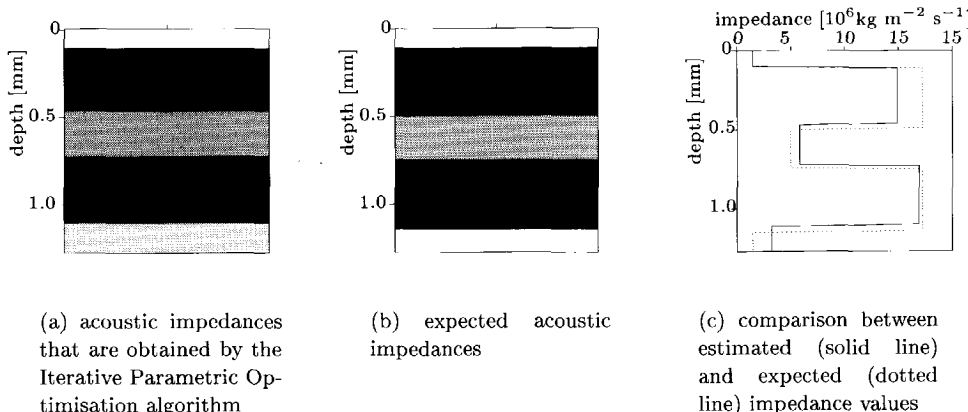


Fig. 5.17 Depth-impedance plot of the acoustic impedance as a function of depth for a simulated reflection measurement on a Glare 2/1 material. Dark colours denote a high impedance value.

Obtained specific acoustic impedances for a glare 2/1 configuration			
Layer	expected $Z_i[\text{kgm}^{-2}\text{s}^{-1}]$	$Z_i[\text{kgm}^{-2}\text{s}^{-1}]$ (IPO)	$Z_i[\text{kgm}^{-2}\text{s}^{-1}]$ (RDI)
0	1.48	1.48	1.48
1	17.26	14.90	15.46
2	4.96	5.79	5.80
3	17.26	16.91	14.24

Table 5.9 Comparison between the expected acoustic impedance, the acoustic impedance obtained by the Iterative Parametric Optimisation algorithm and the acoustic impedance obtained by the Recursive Direct Inversion algorithm applied on real measurements on a Glare 2/1 configuration.

the results from the IPO-algorithm can be used to estimate the layer thickness. The results are given in Table 5.10. Again, the results obtained by the two methods agree with each other. It can be noticed that for the deeper layers, the method of the iterative parametric optimisation give better results. It was shown in the previous chapter that errors propagate throughout the recursion of the RDI-method. The drawback of the method of the iterative parametric optimisation is that it is slower, especially when a high accuracy is desired — and many iteration steps have to be performed.

It thus turns out that both methods have their advantages and disadvantages. The RDI method is fast and gives good results for materials with only a few layers. It

Obtained layer thickness in a glare 2/1 configuration			
Layer	expected Δz_i [mm]	Δz_i [mm] (IPO)	Δz_i [mm] (RDI)
0 (water)	0.1000	0.1000	0.1000
1 (aluminium)	0.4000	0.368	0.369
2 (prepreg)	0.2500	0.255	0.257
3 (aluminium)	0.4000	0.378	0.373

Table 5.10 Comparison between the expected layer thickness, the thickness obtained by the Iterative Parametric Optimisation algorithm and the thickness obtained by the Recursive Direct Inversion algorithm applied on real measurements on Glare 2/1.

is also useful for materials with many layers, when one is more interested in the properties of the top-most layers than in the properties of the bottom-most layers. The quality of the results obtained by the IPO method is less dependent on the depth of the layers. On the other hand, the quality is dependent on the number of iterations that are performed, and thus on the execution time.

Chapter 6

Conclusions and recommendations

In this last chapter, some concluding remarks are made concerning the developed theory and its practical applications. Based on both theoretical results and practical experience, some recommendations for further investigations are given.

6.1 Conclusions

The objective of this thesis is to develop algorithms for characterising acoustic reflection responses from thin, laminated materials. This ultrasonic inspection technique has been developed to overcome the limitations that are encountered in the aerospace industry with the currently used acoustic transmission techniques.

In order to get more information from the measured acoustic reflection response of a material, it is necessary to understand the physical processes that take place when an acoustic wave interacts with a material.

In this thesis, a model has been developed that describes the microscopic and macroscopic phenomena inside the material. In general, the formulation of the acoustic reflection response may be very complicated. Using some assumptions, though, a simple model is obtained. This model is based on the principles of wave propagation — by means of a propagation factor W — and reflection at interfaces — by means of the reflection coefficient R . A similar model based on propagation and reflection is extensively used in data processing for seismic exploration¹.

Typical for the present research, is that the materials that are to be examined consist of thin layers. This is taken into account in the model.

Although the formulation of this model is very general, the definitions for the propagation factor and the reflection coefficient may be adapted to a particular problem.

¹The models used in seismics are often two or three dimensional, whereas the model developed in this research is one dimensional.

In this research, formulations are given for propagation and reflection in instantaneously reacting media and in media with relaxation effects.

Simulations using the model for instantaneously reacting media show a very good correspondence with actually recorded measurements performed on a thin aluminium disk.

This model is not adequate, though, for the simulation of reflection measurements on so-called prepreg layers ². It appears that when performing measurements on this material, some acoustic energy is dissipated. An extended formulation for the propagation factor and the reflection coefficients takes frictional forces and bulk inviscidness into account and therefore allows the dissipation of acoustic energy. By including this, a better match between simulations and measurements is obtained.

The quality of the measurements is important for the comparison between simulations and measurements and for the retrieval of the material parameters. The ultimate goal is to obtain data that are not disturbed by any kind of noise. Since in practice there is always some noise present, it is advantageous to pre-process the data in order to decrease the noise.

The quality of the data is also influenced by the quality of the source signal, being the acoustic excitation for the system. This source signal has to be well-known and repeatable.

Using the forward model, a transfer function can be derived that calculates the expected acoustic response based on the used source signal and the geometrical and material properties of the target.

The actual goal of this research is to obtain the material properties, based on the used source signal and the measured acoustic response.

In this thesis, two methods are described for obtaining the material parameters of a laminate.

The first one is based on the inverse formulations of the forward model. It is a recursive method, since the parameters of the different layers are obtained one at a time. Theoretically, this method should give correct results, but due to noise in the data and due to the fact that not all of the assumptions used in the formulation of the forward model are completely satisfied, the results will not be exact. Moreover, due to the recursive nature of the method, errors will propagate through the different recursion steps.

In the second method, a simulated reflection response is calculated based on an initially estimated set of parameters. The simulated response is compared with the actual measurement, and the parameters are updated. This procedure is repeated until the matching between the measured signal and the simulated response is good enough, or until no further improvement occurs. Generally, this parametric opti-

²A prepreg layer consists of a fibre-reinforced resin — see Appendix A.

misation method will give better results when more iteration steps are performed. Compared with the first method, however, this method is rather slow.

The inversion methods give information about the acoustic traveltimes in the different layers and the reflection coefficients at the interfaces. For inspection purposes, one is more interested in the acoustic impedance of the material as a function of depth. This conversion can be done easily assuming the wave propagation velocity is known. One of the advantages of depth-impedance plots is that void inclusions and delaminations are clearly observed, due to their low acoustic impedance. The latter is extremely important in the inspection of laminated materials, where a low-impedance region may indicate a delamination.

The inversion methods are applied on both simulated and measured data. The application of the inversion methods to the simulated reflection response of a Glare 3/2 material with a delamination, shows that the lateral position and the depth of the delamination can be obtained with a high accuracy.

Practical measurements are done on an aluminium disk and a Glare 2/1 laminate. Both inversion methods are able to detect the different layers, and give a "fair" estimation of the acoustic impedance of the constituting layers. As a consequence, it should be possible to automatically detect very low impedances, due to delaminations. For a fast detection of the material parameters of a target with only a few layers, the method of Recursive Direct Inversion is advised. For a more accurate result, or in the case the target material consists of many layers, it is advised to use the method based on Iterative Parametric Optimisation.

6.2 Recommendations

In this thesis, it has been shown that it is possible to obtain the material parameters of the different layers in a laminate, based on advanced processing of reflection measurements. Some of the recommendations given below can be applied using the model described in this thesis, while others suggest an expansion of the developed model.

6.2.1 Using the existing model

- The quality of the obtained signal can be improved. The current C-scan system used in this research project has been developed for large-scale inspection by means of transmission measurements. The built-in pulser and trigger system are not very accurate, and do not match the requirements of the sensitive Panametrics transducers. It is necessary however to obtain a discretized signal with a high sampling rate and with a good resolution. All aspects of the data acquisition system have to be adjusted to each other. Starting from the

specifications of the transducer — i.e. a frequency range and a power spectrum — a pulser (for delivering the signal) and an A/D converter (for obtaining the signal) have to be selected. Cables have to be chosen very carefully in order to minimise noise.

- Where there is a very good match between simulations and measured acoustic responses of an instantaneously reacting material, the theory describing the propagation and reflection effects in media with relaxation can be improved. It should be investigated whether or not the coefficients of frictional forces and the coefficient of bulk inviscidness are frequency- and amplitude-dependent. The prepreg samples provide a good test-case for this research.
- Depending on the needs of a particular user group, the information from the inversion process does not have to be presented in a depth-impedance plot. It is possible to make a three-dimensional image of the target where the value of the acoustic impedance is indicated with colours.

6.2.2 Enhanced model

- The performed acquisitions are all zero-offset measurements, which means that the signal is measured at the same lateral position where it was generated. As a consequence, one position of the transducer will give information only about one vertical line in the material, and vice versa.

Multi-offset measurements, where the distance between the source and the receiver is non-zero and varies, are very common in seismic exploration. By varying the distance between the source and the receiver, by using more receivers or by a combination of both techniques, there will be more measurements that contain information about one vertical line in the material. A requirement is that the source signal has to be emitted into a specific direction, or into a broad range of angles. This principle is clarified in Figure 6.1.

The reflection coefficient is dependent on the angle of incidence of the wave-field. Using non-normal angles of incidence therefore can reveal more information about the interface where reflection occurs. This technique is extensively used in seismics — e.g. Ostrander (1984), van Wijngaarden (1998).

It is possible to develop processing techniques that extrapolate the measured signal backwards to a point in the material where it was reflected. All measurements that contain information about the considered point can be combined and this way more information about that point is obtained. In seismic exploration, this technique already exists and is called Common Focus Point (CFP) technology — e.g. Thorbecke (1997).

- When an incident wave arrives at the boundary of a material under a non-

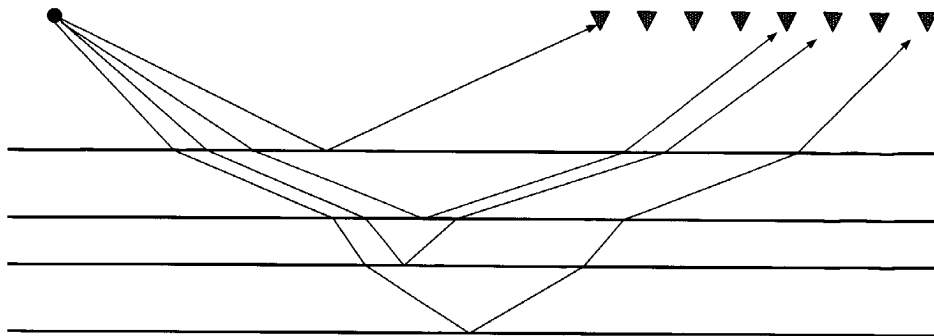


Fig. 6.1 The principle of multi-offset measurements.

perpendicular angle, mode conversion occurs at the interface. The incident compressional wave will be converted into a compressional reflected wave and into compressional and shear waves entering the material.

When the shear waves arrive at the boundary between the material and the water (after being reflected at least once inside the material), the wave is partly converted into a compressional transmitted wave in water. This principle is illustrated in Figure 6.2.

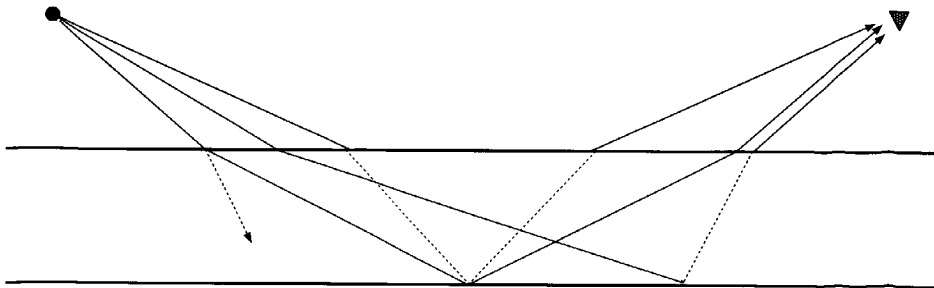


Fig. 6.2 The principle of mode conversions. Compressional waves are represented by solid lines, shear waves are shown with dotted lines. Note that for simplicity not all conversions are shown.

The above mentioned process can be compared with the mode conversions occurring at the bottom of the ocean in marine seismic measurements — e.g. Schalkwijk et al. (1999).

Shear waves have other properties than the acoustic pressure waves, and they can reveal more information about the material and the interfaces. If both the compressional wave velocity and the shear wave velocity are obtained, more material parameters can be calculated than in the case only the compressional velocity is known. This can for example give information about the porosity of the considered material. In seismics, relationships between the compressional and the shear wave velocity are used as lithology indicators — e.g. van Wijngaarden (1998).

Appendix A

Glare

The theory developed in the first part of Chapter 2 is very general. The basic principles can be applied to different media with their own geometrical and material properties. The developed model, however, is specifically tuned for laminated materials, since this is the goal of the present research.

A.1 Structure and naming

Glare is a material developed at Delft University of Technology — see Roebroeks (1991) and Vlot et al. (1998) — and it belongs to the family of the fibre-reinforced metal laminates. These materials typically consist of alternating layers of metal sheets and fibre-reinforced resin layers.

In Glare, the metal sheets are made of aluminium, and the fibre-reinforced resin layers are composed of glass fibres in an epoxy resin¹. The layered structure of Glare is shown in Figure A.1.

Both the aluminium and the prepreg layers can have different properties. For Glare1, the aluminium alloy is 7475-T76² and one layer has a thickness between 0.3 mm and 0.4 mm. The aluminium alloys in the other Glare variants are 2024-T3.

The prepreg layers are composed of two or more sub-layers, each having a thickness of 0.125 mm. In each sub-layer, the filers are oriented in one particular direction. If the alternating sub-layers in a prepreg layer have the same fibre-direction, the resulting prepreg layer has a uni-directional orientation. On the other hand, if the fibre direction in a sub-layer is perpendicular to the fibre direction in the enclosing sub-layers, the layer has a cross-ply orientation. An overview of the possible combinations and their corresponding names is given by Coenen (1998).

¹Arall, a predecessor of Glare consists of alternating aluminium and aramid fibre layers.

²Information about the properties of different alloys can be found on the World Wide Web, <http://www.matweb.com>, or in the literature e.g. Boyer and Gall (1985).



Fig. A.1 Layered structure of a Glare 3/2 material. Aluminium layers are coloured dark grey, and prepreg layers are coloured light grey, which is in agreement with the acoustic impedance of these materials.

Apart from the internal properties of both the aluminium alloy and the prepreg layer, the number of layers is an important property. Therefore, Glare laminates are typically called *Glare x/y*, where x is the number of aluminium layers in the material, and y is the number of prepreg layers. Since each layer is covered by two layers of the other kind — except for the most outward aluminium layers —, it has to hold that $x = y + 1$.

A.2 Properties

The properties of fibre metal laminates — compared with the properties of traditional aluminium structures — are studied by a.o. Slagter (1994). One of the most important benefits of Glare over traditional aluminium materials, is the crack-bridging mechanism which is illustrated in Figure A.2.

When a crack occurs in one of the aluminium layers, the load can — partially — be carried by the glass fibres in prepreg layers next to the aluminium layer with the crack. As a consequence, the crack can not proceed — at least, not as fast as it would proceed without a prepreg-layer.

The slow crack growth in Glare has an important effect on the safety and on the total cost of the material — and consequently the airplane it is composed of. In Figure A.3, the crack length as a function of time is shown. The figure gives only relative information about crack length and evolutions. The minimum crack size that can be detected by a particular scan system is denoted by l_d . The critical crack size, which is considered to be damaging, is given by l_c . It follows from Figure A.3

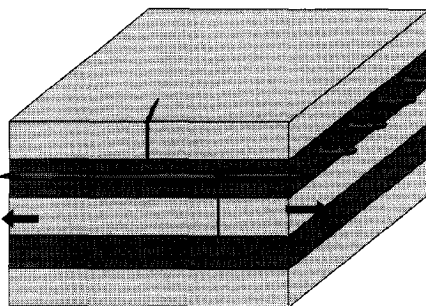


Fig. A.2 Crack-bridging system in Glare.

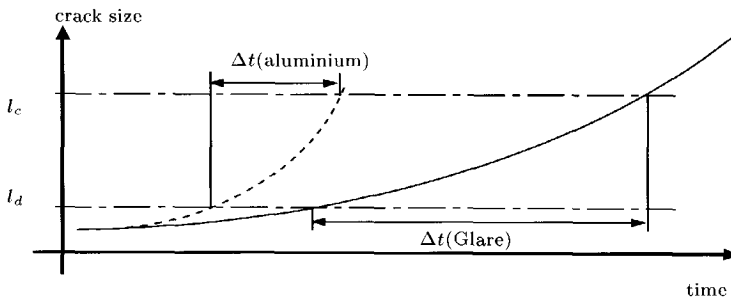


Fig. A.3 Crack growing in aluminium (dotted line) and Glare (solid line). As can be seen, the time window Δt in which defects can be detected before they are critical, is much larger for Glare than for aluminium.

that the time between the minimum detected crack size and the critical crack size is much larger for Glare than for aluminium. As a consequence, there is a larger time window in which investigators can determine possible damage in a Glare structure. Besides, Glare materials have to be inspected on a less regular basis than aluminium materials.

Bibliography

Achenbach, J. D. (1973). *Wave propagation in elastic solids*. Elsevier science publishers B.V.

Aki, K. and Richards, P. (1980). *Quantitative Seismology*. W.H. Freeman and Co.

Berkhout, A. J. (1973). On the minimum-length property of one-sided signals. *Geophysics*, **38**(4), 657–672.

Berkhout, A. J. (1987). *Applied seismic wave theory*. Elsevier.

Boyer, H. E. and Gall, T. L. (1985). *Metals handbook*. American society for metals.

Bray, D. E. and Stanley, R. K. (1997). *Nondestructive evaluation, A tool in design, manufacturing, and service*. CRC Press.

Brekhovskikh, L. M. (1980). *Waves in layered media*. Academic press.

Chua, L., Desoer, C., and Kuh, E. (1987). *Linear and Nonlinear Circuits*. McGraw-Hill.

Claerbout, J. F. (1976). *Fundamentals to Geophysical Data processing*. McGraw-Hill.

Cocnen, R. A. M. (1998). *Design of a quality assurance system for structural laminates*. Delft University Press.

De Hoop, A. T. (1995). *Radiation and scattering of waves*. Academic Press.

De Meester, P. (1988). *Kwaliteitscontrole en mechanische eigenschappen van materialen*. Acco.

Dessing, F. J. (1997). *A wavelet transform approach to seismic processing*. Ph.D. thesis, Delft University of Technology.

Gill, P. E., Murray, W., and Wright, M. H. (1981). *Practical optimization*. Academic Press.

Golub, G. H. and Van Loan, C. F. (1989). *Matrix computations*. The Johns Hopkins University Press.

Herrmann, F. J. (1997). *A scaling medium representation: a dicussion on well-logs, fractals and waves*. Ph.D. thesis, Delft University of Technology.

Johnson, N. L. and Leone, F. (1977). *Statistics and experimental design in engineering and the physical sciences*. John Wiley & Sons Inc.

Kennett, B. L. N. (1974). Reflections, rays and reverberations. *Bull. Seis. Soc. Am.*, **64**, 1685–1696.

Kennett, B. L. N. (1983). *Seismic wave propagation in stratified media*. Cambridge university press.

Koek, E. A. (1991). *Theoretical and experimental study of the field radiated by ultrasonic transducers*. Master's thesis, Delft University of Technology.

Körner, T. (1993). *Excercises for Fourier Analysis*. Cambridge University Press.

Kreyszig, E. (1972). *Advanced engineering mathematics, third edition*. John Wiley & Sons Inc.

Legouis, T. and Nicolas, J. (1987). Phase gradient method of measuring the acoustic impedance of materials. *The journal of the acoustical society of America*, **81**(1), 44–50.

Mood, A. M. (1987). *Introduction to the theory of statistics*. McGraw-Hill.

O'Neil, H. T. (1949). Theory of focussing radiators. *The journal of the acoustical society of America*, **21**(5), 516–526.

Ostrander, W. J. (1984). Plane-wave reflection coefficients for gas sands at nonnormal angles of incidence. *Geophysics*, **49**(10), 1637–1648.

Paul, D. I. (1957). Acoustical radiation from a point source in the presence of two media. *The journal of the acoustical society of America*, **29**(10), 1102–1109.

Pierce, A. D. (1989). *Acoustics, An introduction to its physical principles and applications*. Acoustical Society of America.

Roebroeks, G. (1991). *Towards Glare — the development of a fatigue insensitive and damage tolerant aircraft material*. Ph.D. thesis, Delft University of Technology.

Schalkwijk, K., Wapenaar, C., and Verschuur, D. (1999). Application of two-step decomposition to multicomponent ocean-bottom data: theory and case study. *Journal of seismic exploration*, **8**(8), 261–278.

Schwartz, L. (1957). *Theorie des distributions, vol. I*. Hermann and Cie, Paris.

Slagter, W. (1994). *Static strength of fiber metal laminates*. Ph.D. thesis, Delft University of Technology.

Sydenham, P. H. (1982). *Handbook of mathematical Science*. John Wiley & Sons Inc.

Tarantola, A. (1987). *Inverse problem theory, methods for data fitting and model parameter estimation*. Elsevier.

Thorbecke, J. (1997). *Common focus point technology*. Ph.D. thesis, Delft University of Technology.

Toksoz, M. N. and Johnston, D. H. (1981). *Seismic wave attenuation*. Society of Exploration Geophysicists.

Tolstoy, I. (1992). *Acoustics, elasticity and thermodynamics of porous media: twenty-one papers by Maurice A. Biot*. Acoustical Society of America.

van Wijngaarden, A. J. (1998). *Imaging and characterization of angle-dependent seismic reflection data*. Ph.D. thesis, Delft University of Technology.

Verschuur, D. V. (1991). *Surface-related multiple elimination, an inversion approach*. Ph.D. thesis, Delft University of Technology.

Vlot, A., Vogelesang, L. B., and de Vries, T. J. (1998). *Fibre metal laminates for high capacity aircraft*. 30th Int. SAMPE Technical Conference, San Antonio, Texas.

Wapenaar, C. P. A. and Berkhouit, A. J. B. (1989). *Elastic wave field extrapolation*. Elsevier.

Yilmaz, O. (1987). *Seismic Data Processing*. Society of Exploration Geophysicists.

Zemanian, A. H. (1965). *Distribution theory and transform analysis*. Dover Publications, inc.

Characterisation of laminated construction materials based on ultrasonic reflection measurements

The goal of ultrasonic inspection is to obtain information about the examined material. Current ultrasonic inspection techniques based on C-scan measurements do not reveal information about the structure of the material. Apart from that, the target material needs to be accessible from both sides.

The method described in this thesis reveals more information about the internal structure of the material. Besides, it is based on reflection measurements and as a consequence, the material needs to be accessed from only one side.

A good understanding of the interaction of an ultrasonic wave with a material is required. The study of these interactions is very general, and can also be applied on different fields — e.g. medical or seismic applications. Based on the knowledge of these interactions, a model is developed for the specific case of the ultrasonic inspection of laminated materials. The developed model is valid for layers composed of instantaneously reacting media as well as for layers composed of media with relaxation effects.

The model allows one to perform simulations of reflection or transmission measurements on targets. The obtained simulations can be compared with real obtained measurements. It is shown in this thesis that the simulations based on the developed model resemble real measurements after some filtering and statistical operations are performed on these measurements.

Based on the developed model, inversion algorithms can be developed. The goal of inversion is to obtain the material parameters of the examined target, based on the measured response.

Two different inversion algorithms are described, the first one based on a direct inversion of the equations of the forward model, the second one based on an iterative

optimisation of the material parameters.

Both algorithms are first tested on simulations of reflection measurements. It is shown that there is a very good match between the true material parameters and the parameters obtained by the inversion algorithms. The inversion algorithms can be used to obtain the specific acoustic impedance of the different layers of the material, or they can be used to estimate the thickness of the layers. Especially the layer thickness is obtained with a very high accuracy.

The inversion methods are also tested on reflection measurements on an aluminium layer and a Glare 2/1 laminate. It turns out that both the layer thickness and the specific acoustic impedance of the different layers can be obtained with a good accuracy. Both methods have their advantages and disadvantages. The method based on direct inversion is appropriate for materials with only a few layers, or when processing time is critical. The method based on iterative parametric optimisation, on the other hand, is appropriate when a high accuracy is required, or when the material consists of a lot of layers.

Karakterisatie van gelaagde constructiematerialen, gebaseerd op ultrasone reflectie-metingen¹

Het doel van ultrasone inspectie is het verkrijgen van informatie over het onderzochte materiaal. De huidige ultrasone inspectie technieken gebaseerd op C-scan metingen geven geen informatie over de structuur van het materiaal. Bovendien is het noodzakelijk dat het beschouwde materiaal van twee kanten benaderd kan worden.

De methode die in dit proefschrift beschreven wordt, geeft meer informatie over de interne structuur van het materiaal. Daarenboven is ze gebaseerd op reflectiemetingen. Dit laatste heeft tot gevolg dat het materiaal slechts langs één kant benaderd moet worden.

Het is noodzakelijk een duidelijk inzicht te hebben in de interacties tussen een ultrasone golf en een materiaal. De studie van deze interacties is zeer algemeen, en kan ook toegepast worden in andere onderzoeksgebieden — bijvoorbeeld voor medische en seismische toepassingen. Gebaseerd op de kennis van deze interacties is een model ontworpen voor het specifieke geval van de ultrasone inspectie van gelaagde materialen. Het model is zowel geldig voor lagen die bestaan uit instantaan reagerende media als voor lagen die bestaan uit media waar relaxatie effecten optreden.

Uitgaande van dit model is het mogelijk om simulaties van reflectie metingen op materialen uit te voeren. De bekomen simulaties kunnen vergeleken worden met echte metingen. In dit proefschrift is aangetoond dat de simulaties gebaseerd op het ontwikkelde model een sterke overeenkomst vertonen met echte metingen, nadat een aantal filter en statistische bewerkingen zijn uitgevoerd op de gemeten data.

Gebaseerd op het ontwikkelde model, kunnen inversie-algoritmes ontworpen wor-

¹Flemish summary of *Characterisation of laminated construction materials based on ultrasonic reflection measurements*.

den. Het doel van inversie is het bekomen van de materiaal parameters van het beschouwde materiaal, uitgaande van de gemeten reflectie-responsie.

In dit proefschrift worden twee verschillende inversie-algoritmes beschreven. De eerste is gebaseerd op een rechtstreekse inversie van de vergelijkingen van het voorwaartse model, terwijl de tweede gebaseerd is op een iterative optimalisatie van de materiaal parameters.

Beide algoritmes worden eerst getest op gesimuleerde reflectie-metingen. Er wordt aangetoond dat er een sterke overeenkomst is tussen de echte materiaal parameters en de parameters die door de inversie algoritmes bekomen worden. De inversie-algoritmes kunnen gebruikt worden om de specifieke akoestische impedantie van de verschillende lagen van het materiaal te bekomen, of ze kunnen gebruikt worden om de dikte van de verschillende lagen te schatten. Vooral de dikte van de lagen wordt verkregen met een erg grote nauwkeurigheid. De inversie-algoritmes worden ook getest op echte reflectie-metingen op een aluminium plaat en een Glare 2/1 laminaat. Het blijkt dat zowel de laagdikte als de specifieke akoestische impedantie van de verschillende lagen verkregen worden met een goede nauwkeurigheid.

Beide methodes hebben hun voor- en nadelen. De methode gebaseerd op de directe inversie is geschikt voor materialen met slechts enkele lagen, of in het geval er een strikte limiet is gesteld voor de verwerkingstijd. Aan de andere kant is de methode gebaseerd op de iteratieve parametrische optimalisatie vooral geschikt wanneer een grotere nauwkeurigheid vereist is, of wanneer het materiaal bestaat uit een groot aantal lagen.

Curriculum vitae

Naam	Johan Vos
Geboortedatum	6 september 1973
Geboorteplaats	Mechelen, België
Opleiding	
1979 - 1984	basisonderwijs te Puurs
1984 - 1990	secundair onderwijs te Puurs
1990 - 1992	kandidaat Burgerlijk Ingenieur aan de Katholieke Universiteit Leuven
1992 - 1995	Burgerlijk Mijnbouwkundig Ingenieur aan de Katholieke Universiteit Leuven
Werkervaring	
1995	Projectmedewerker aan de faculteit Toegepaste Aardwetenschappen van de Technische Universiteit Delft
1996 - 2000	Onderzoeker in Opleiding aan de Technische Universiteit Delft, Laboratorium voor akoestische beeldvorming en geluidsbeheersing, STW project DLR.3433
1999 -	Java- en IT-consultant
2000 -	Software ingenieur, SmartMove NV

Dankwoord

Het boekje is bijna vol, maar er is nog plaats om de mensen te bedanken zonder wie dit boekje er helemaal niet zou zijn geweest.

De beide promotoren, professor Berkhout en professor Wapenaar, verdienen een grote pluim vanwege hun overtuiging dat technieken die in de onderzoeksgroep ontwikkeld werden voor seismische toepassingen ook hun nut kunnen hebben op het gebied van ultrasone inspectie. Ik hoop dat ik met dit proefschrift de ultrasone inspectie-wereld van hun gelijk heb kunnen overtuigen.

De kritische geest van Kees Wapenaar stimuleerde me om mijn intuitief gelijk wetenschappelijk te onderbouwen — hetgeen vaak leidde tot het bijschaven van dit intuitief gelijk. Ik bedank Eric Verschuur voor zijn diplomatiek talent. Wanneer metingen of resultaten niet voldeden aan de verwachtingen, was Eric er met zijn "tips en trukendoos" om me weer op het rechte pad te brengen — of om een eventueel schuin pad wat rechter te maken.

Mijn waardering gaat ook uit naar de mensen van de faculteit Lucht- en Ruimtevaart voor hun excellent werk op het gebied van laminated, en voor hun open visie om de faculteit Natuurkunde te betrekken bij het ultrasoon onderzoek. Professor Vogelesang verdient bijzondere appreciatie als projectleider van het STW-project waar dit onderzoek deel van uitmaakt. Verder bedank ik ook Remco Coenen, Dylan Krul, Gérard Brouwers en Tjerk de Vries.

Alleen werken is maar saai, maar gelukkig waren er de collega's. Promovendi komen en gaan, en de lijst (ex-)collega's is dan ook behoorlijk lang. Ik bedank in het bijzonder Karin "Amazone" Schalkwijk voor haar deskundige opmerkingen op het gebied van de Engelse taal en de omgang met paarden; Ewoud "Coop" van Dedem voor de Twin Peaks-marathons met de (vergeef me de uitdrukking) "damn fine coffee"; Barbara "CGO" Cox voor haar grafisch inzicht en haar eufemistische kritiek op mijn grafisch prutswerk; John "TN" Bolte voor het incasseren van Hollander-moppen. De promotiedatum van mijn kamergenoten Frederic Verhelst, Paul Zwartjes en Kees Hindriks is door mijn aanwezigheid mogelijk wat uitgesteld, maar ze

zitten nu hopelijk wel op het juiste Linux-pad.

Ik mag niet vergeten Alexander Koek, Gerrit van Dijk en Maurits van der Heiden te bedanken voor hun deskundig advies en hun toewijding om ook op vrijdagavond beschikbaar te zijn voor verdere discussies.

Ik ben veel dank verschuldigd aan mijn vrienden in België, die me voor een naturalisatie hebben kunnen behoeden. Een speciale vermelding gaat naar Koen Bruynseels voor het ontwerp van de kaft van dit proefschrift.

Tot slot bedank ik mijn broers en vooral mijn ouders, die me de mogelijkheid, het vertrouwen en de vrijheid hebben gegeven om dit werk te verrichten.



